Università degli Studi di Padova

DIPARTIMENTO DI ASTRONOMIA

Dottorato di Ricerca in Astronomia
XXIII ciclo

Observed Stellar Spectra As Templates For Gaia

Coordinatore: Prof. Giampaolo Piotto

Supervisori: Prof. Antonella Vallenari

Prof. Ulisse Munari

Dottoranda: Tenay Saguner

31 Gennaio 2011

To My Family &
To Prof. I. Ethem Derman

Contents

List of Figures

List of Tables

Chapter 1

Introduction

The ESA's Gaia mission (Lindegren & Perryman, 1995) is an all-sky astrometric and spectro-photometric survey of all point-like sources (i.e. stars, asteroids, quasars, extragalactic-supernova, etc.) between V $\sim 6^{th}$ - 20^{th} magnitude. During it's 5 years mission (with an additional one year) lifetime it will produce a stereoscopic and kinematic view of $\sim 10^9$ stars. The main scientific goal of Gaia is to study the composition, origin and evolution of our Galaxy. Gaia main contribution to this topic is to establish accurate stellar distances with 3-dimensional space motions that will enable us to study the 3-dimensional structure and kinematics of different types of stars in the Galaxy. The complementary use of low-resolution spectrophotometry and medium-resolution spectroscopy will provide information about intrinsic astrophysical properties of stars, in particular effective temperatures, surface gravities, abundances, masses and ages. Gaia will allow to address key questions of modern astrophysics regarding the formation and evolution of the Milky Way.

Considering the amount of objects that will be observed by Gaia, the challenge is to design classification systems and develop appropriate algorithms that can analyze automatically the Gaia data and extract reliable estimations of object classes with their reliable astrophysical parameters (Bailer-Jones, 2005). The classification, parametrisation will rely on templates which are builded from grids of synthetic spectra. Thus, tests and calibrations of these algorithms require set of stars for which the atmospheric parameters and radial velocities are well known. Moreover, parametrisation is based on stellar atmosphere models which are still not perfect. Thus, observed spectra of stars with well determined parameters are important also to test and improve synthetic spectra.

From Gaia observations, the possibility to combine astrophysical properties of stars with their radial velocity measurements will be limited to $11^{th} \leq$ V $\leq 13^{th}$ mag (depending on the resolution). Thus, stars with magnitudes between this threshold limit will provide us complete information including the radial velocities. On the other hand, F,G and K spectral type stars will be the most numerous among the objects observed by Gaia.

In this context, Red Clump stars will be inevitable sources which we can attain a complete set of information from Gaia since those stars are intrinsically bright and their spectral

types ranges mostly between G8III to K2III. Apart from being abundant in the Galaxy and being luminous, in this evolutionary stage those stars also occupy a compact region on the Hertzprung-Russel diagram with having same luminosities, reliable spectro-photometric distance estimates can be obtained for them. On these grounds Red Clump stars are of great interest in analyzing the 3-dimensional kinematics of Galaxy and its sub-systems.

Thus, in this study we aimed to carry out a medium resolution spectroscopic survey for a sample ($\sim$ 500) of well chosen Red Clump stars and constitute a catalog. This catalog contains accurate radial velocities, atmospheric parameters (T_{eff}, $\log g$ and $[M/H]$) and space velocities (U,V,W) combined with additional photometric and spectroscopic information compiled from previous catalogs in literature (Hipparcos (Perryman et al., 1997), Tycho-2 (Høg, 1998), 2Mass (Cutri et al., 2003), Denis (Cioni et al., 1999)).

We observed 305 of Red Clump stars with Asiago 1.22m + B&C spectrograph at multi-epochs. Radial velocities are derived via cross-correlation against observed templates and atmospheric parameters derived via χ^2 fitting against a grid of synthetic stellar spectra. The accuracy for radial velocities, is $\sigma(RV) = 1.3$ kms^{-1} and for atmospheric parameters, $\sigma(T_{eff}) = 88$ K, $\sigma(\log g) = 0.38$ dex and $\sigma([M/H]) = 0.17$ dex respectively.

Our final catalog can be used as reference to test, train and calibrate classification algorithms during the preparation of the Gaia mission. At the same time, our catalog can allow to study kinematical and structural properties of the Solar neighbourhood.

Chapter 2 presents the Gaia Mission, the scientific goals and the instruments. Chapter 3 summarizes the properties of Red Clump stars. The sample selection is described in Chapter 4. Chapter 5 presents the observations and data reduction. Chapters 6 and 7 deal with the methods and tests to derive accurate radial velocities and athmospheric parameters, respectively. Chapter 8 discusses the quality control from repeated observations. Chapter 9 presents the final catalog. Finally Chapter 10 discusses the properties of the stars, their ages, kinematics as tracers of the Galactic disks.

Chapter 2

The Gaia Mission

The formation and evolution of galaxies is one of the most debated problems in Astrophysics and detailed studies on our Galaxy are the first step to understand these complex processes. The Gaia mission will provide positional and radial velocity measurements with the accuracy needed to produce a stereoscopic and cinematic census of about one billion stars throughout our Galaxy (and into the Local Group). Gaia astrometric mission is one of the next cornerstones of ESA's science program, with a launch date target of not later than mid-2012. GAIA main scientific goal is to clarify the origin and history of our Galaxy, from a quantitative census of the stellar populations.

It will advance questions such as when the stars in our Galaxy formed, when and how the Galaxy was assembled, and what is the distribution of dark matter. The survey aims for completeness to V = 20 mag, with accuracies on distances of about 10 μas as at 10^{th} mag. This will be combined with astrophysical information for each star, provided by on-board BP/RP photometry and (limited) spectroscopy by means of the radial velocity spectrograph (RVS). Additional products include detection and orbital classification of extra-Solar planetary systems, and a survey of minor bodies in our Solar System, of galaxies in the nearby Universe, and distant quasars. It will provide a number of stringent new tests of general relativity and cosmology.A summary of the Gaia science case can be found in ESA-SCI(2000)4 to whom we refer for more detail and refeneces.

Gaia mission covers a wild range of scientific objectives, among them we would like to recall :

- **Galaxy Structure And Evolution:** Understanding our Galaxy requires measurement of distances and space motions for large and unbiased samples of stars of different mass, age, metallicity, and evolutionary stage. Being an all-sky, magnitude limited survey, Gaia will be a peerless tool for the reconstruction of the Milky Way. Gaia will bring major inputs to the understanding of the formation and the history of the Galaxy by combining positional, kinematical and chemical informations for 1.5 billion stars ($\sim$ 0.5% of the stellar content of the Galaxy). It will observe $\sim 9 \times 10^8$ stars in the thin disk, $\sim 4 \times 10^8$ stars in the thick disk (Bailer-Jones, 2009) and

$\sim 2 \times 10^7$ in the bulge. All those measurements will allow to test the hierarchical structure formation; to study the kinematics of the disks; to detect internal proper motions of associations, and nearby open clusters; to derive the kinematics of Local Group dwarfs. The study of the bulge will be difficult and limited because of extinction and crowding (Robin et al., 2005). However, using Gaia data we can derive the shape and figure of rotation. The dynamics of the spiral arms and nature of the stellar warp will be reconstructed with high precison. Finally substructures in the halo including tidal accretion debris will be discovered.

- **Stellar Formation And Evolution:** The study of stellar structure and evolution provides fundamental information on the properties of matter as well as on the evolution of galaxies and cosmology. Gaia will provide unprecedented and complete information on stars of all spectral types and all evolutionary stages. This will sample the stellar evolutionary phases, allowing precise isochrone reconstruction and detailed comparison with stellar models. Finally, the star formation of the Galactic populations will be derived. Coupling these informations with individual abundances of key chemical elements, e.g. Ca, Mg and Si, for millions of stars up to V $\sim$ 12 mag, will bring major improvement in our knowledge of the chemical history and the enrichment processes of the Galaxy. Finally, from the $862 - nm$ Diffuse Interstellar Band (DIB), RVS data will allow astronomers to derive a $3 - D$ map of interstellar reddening (Katz, 2009; Munari et al., 2005).

- **Binary And Multiple Stars:** The RVS will provide the radial velocities of about 100−150 million stars up to V=16 mag with a precision from 15 kms^{-1} at the faint end to 1 kms^{-1} (or better) at the bright end. The RVS will collect, on average, ∼40 (transit) spectra per star over the 5 years of the mission. The associated multi-epoch radial velocity information will be ideally suited for identification and characterization of double and multiple systems. In particular, Gaia will provide masses and radii accurate to a few per cent for thousands of eclipsing binaries (Munari et al., 2000, 2004).

- **Extra-Solar Planets:** Gaia will also make a systematic census of giant planets ($M_P \geq 2-3$ $M_{Jupiter}$), providing insights into the frequency of giant planets as a function of the characteristics of their host stars and their locations in the Galaxy (Lattanzi, 2010; Rambaux et al., 2009). This will give unique information about the conditions favouring the formation of planets. Since the presence and location of one or several giant planets may severely affect the formation of smaller planets in a system, Gaia will provide important information on the likelihood of finding Earth-like planets orbiting their stars in the habitable zone.

- **Local Group:** Gaia will make a unique contribution to extragalactic astronomy, for example addressing the structure, dynamics and stellar populations in the Magellanic Clouds, M31 and M33. Evenif the $\sigma_\pi/\pi \leq 0.1$ parallax accuracy will not be available beyond $\sim$ 10 kpc, proper motions of individual giants and super giants in LMC ($D_\odot \sim 50$ kpc) and SMC ($D_\odot \sim 63$ kpc) will be accurate enough to allow

Table 2.1: Expected numbers of specific objects observed by Gaia

Object Type	Number
Extragalactic Supernovae	20×10^3
Resolved Galaxies	$10^6 - 10^7$
Quasars	50×10^4
Solar System Objects	25×10^4
Brown Dwarfs	$\geq 50 \times 10^3$
Extra-Solar Planets	15×10^3
Resolved Binaries	10^7 within 250 pc

to discriminate between the member and field stars (Kucinskas et al., 2005) and to derive the LMC and SMC space motions.

A summary of the expected number of objects observerved by Gaia is presented in Tab. 2.1

Gaia will represent an incomparable follow up of the Hipparcos mission (1989-1993, Perryman et al. (1989) and van Leeuwen (1997)), with huge improvements in terms of: measurement accuracy, limiting magnitude (therefore the number of observed objects) and the combination of astrometric, photometric, spectroscopic observations. A comparison of the characteristics and the performances of Gaia mission and Hipparcos mission can be found in Tab. 2.2.

2.1 Overview Of The Gaia Mission

The Gaia project is the result of a large and complex collaboration between many individuals, teams, and organizations. ESA, with the support of the prime contractor, EADS Astrium, design, build and test the satellite and payload. Scientists from ESA Member States in the Gaia Data Processing and Analysis Consortium (DPAC) will develop the procedures for the acquisition and analysis of data, and will produce the final catalogue. The resulting data from Gaia will be available to the ESA scientific community.

2.1.1 Measurement Principles

The Gaia payload design has arisen from the requirements on astrometric precision and completeness, the provision of accurate spectrophotometry for astrophysical diagnostics,

	Hipparcos	Gaia
Completeness	V $\sim$ 9 *mag*	V $\sim$ 20 *mag*
Limiting Magnitude	V $\sim$ 12.4 *mag*	V $\sim$ 20 *mag*
Number Of Sources	$\sim 1.2x10^5$	$\sim 1.5x10^9$
Quasars	none	$\sim 10^6$
Galaxies	none	$\sim 10^7$
Astrometric Accuracy	$\sim$ 1 *mas*	V$\leq$ 10 $\Rightarrow$ 10 μas
		V= 15 $\Rightarrow$ 20 μas
		V= 20 $\Rightarrow$ 100 μas
Spectro-Photometry	2 Bands	Low-Resolution
		330$-$1050 *nm*
		$R_P \sim 20 - 100$
Spectroscopy	none	V$\leq$ 16 $\Rightarrow$ 1$-$10 km s^{-1}
		848$-$874 nm
		$R_P \sim 11000$
Target Selection	Input Catalog	OnBoard Detection

Table 2.2: A comparison of Gaia mission and Hipparcos mission in terms of characteristics and performances.

the acquisition of radial velocities and the need for on-board object detection (Perryman et al., 2001).

The main goal of Gaia mission is to perform global (wide field) astrometry as opposed to local (narrow field) astrometry. In local astrometry, the stars position are measured with respect to a neighbouring star in the same field. Even with an accurate instrument, the propagation of errors is prohibitive when making a sky survey. The principle of global astrometry is to link stars with large angular distances in a network where each star is connected to a large number of other stars in every direction. Global astrometry requires the simultaneous observation of two fields of view in which the star positions are measured and compared.

Gaia optical configuration is based on two telescopes looking at two different fields of view mapped on the same focal plane (FP, for detailes see Fig. 2.4) and superimposed on the same image. An iterative procedure will provide matches of the objects in successive scans, updates of the attitude of the satellite and its calibrations, solving for the object positions and feeding back them into the system (Global Iterative Solution, for details we recommend Lindegren, 2005). In this way the system is self calibrating by the use of isolated non variable point sources that will form a sufficiently large body of reference

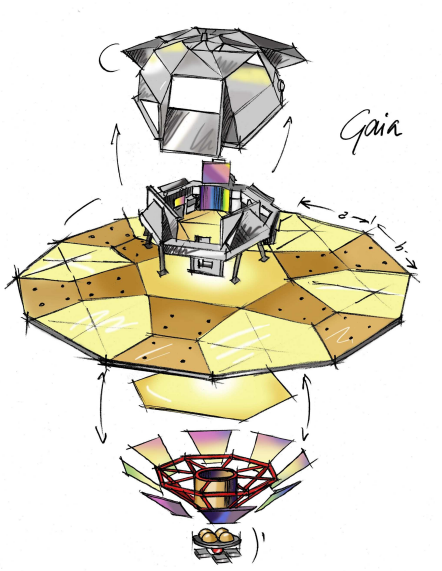

Figure 2.1: An artistic expression of Gaia satellite.

objects for most calibration purposes, including the definition of the Celestial Frame.

2.1.2 Observation Principle

Fig 2.2 shows the precessional motion of the spin axis causing the two fields of view to successively cover the sky.

With this two fields of view, the satellite will perform a continuous scanning of the sky along a great circle completing a rotation in 6 hours (see Fig. 2.2), according to a revolving scanning law at a rate of 60 arcsec s^{-1}. With a precession period of the spin axis of 70 days, at the end of the mission the whole sky will be observed several times, from a few tens to more than 200 times depending on the position, the average value being around 80. (Fig. 2.3 shows the sky coverage after 5 years of Gaia mission.)

2.1.3 Instruments And Performances

The payload consists of a toroidal structure (optical bench) holding the two identical primary mirrors of 1.45×0.5 m in size and 35 m focal length that are superposed and combined on the same focal plane that contains all the instruments devoted to astrometric, spectrophotometric and spectroscopic measurements(Fig. 2.4). Due to the scan mode of Gaia, the instantaneous image moves across the detector, in a direction which is mostly co-linear with the CCD rows and the y axis of the Gaia reference frame (Fig 2.5). In order to achive a useful integrated image, the detector is operating in Time-Delay Integration (TDI) mode, providing the match between the continuous satellite motion (resulting in

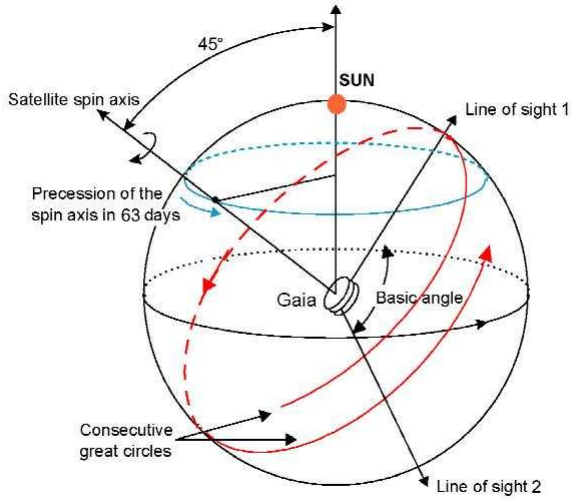

Figure 2.2: The Gaia scanning law. (Figure taken from rssd.esa Gaia web page)

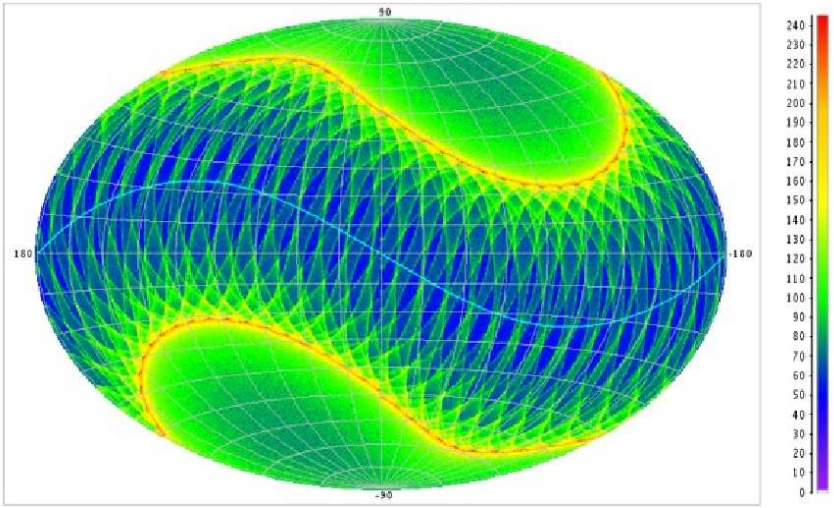

Figure 2.3: The sky coverage of Gaia after 5 year mission time. (Figure taken from rssd.esa Gaia web page)

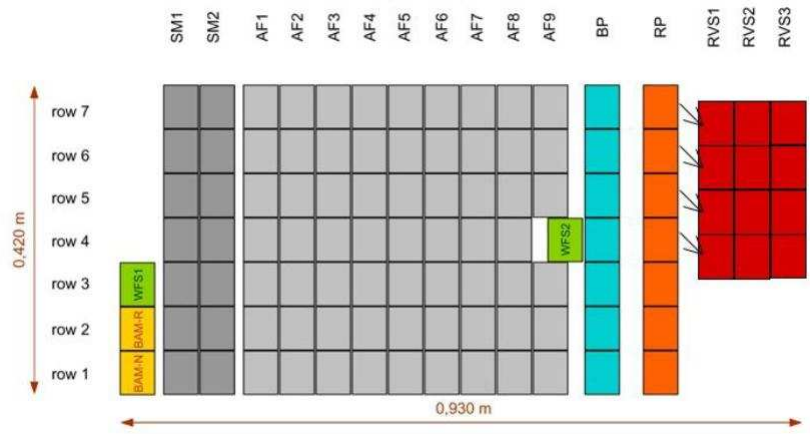

Figure 2.4: The Focal Plane Of Gaia. (Figure taken from rssd.esa Gaia web page)

a continuous apparent motion of the image on the focal plane) and the CCD transfer velocity.

Fig 2.4 shows the focal plane of Gaia. The focal plane holds:

- the wave-front sensor (WFS) and basic angle monitor (BAM) (first strip);
- the two strips of Sky Mapper (SM), an array of 2×7 CCDs that are autonomously detecting objects entering the fields of view and communicating details of the star transits to the subsequent CCDs;
- the main Astrometric Field (AF), an array of 9×7 CCDs devoted to astrometric measurements (parallaxes, proper motions) and an integrated white-light photometry at G band;
- the Blue and Red Photometers (BP and RP), two columns of 7 CCDs that are providing low dispersion ($R_P \sim 20$ for BP and ~ 100 for RP) spectrophotometric measurements for each object over the wavelength ranges 330−680 and 640−1000 nm, respectively;
- the Radial Velocity Spectrograph (RVS), an array of 3×4 CCDs registering spectra of all objects brighter than about V = 16.5 mag in the wavelength range of the CaII triplet (847−874 nm) at a resolution of $R_P \sim 10000$.

The instantaneous image is integrated throughout the whole transit over the CCD, as each pixel is generated at the leading edge and transferred in steps with the corresponding point in object space up to the trailing edge of the device where the readout process takes place.

Readout on the Astrometric Field (Fig. 2.4) is restricted to the regions of interest identified by the Sky Mapper: for each star, a surrounding window is identified and read. Depending

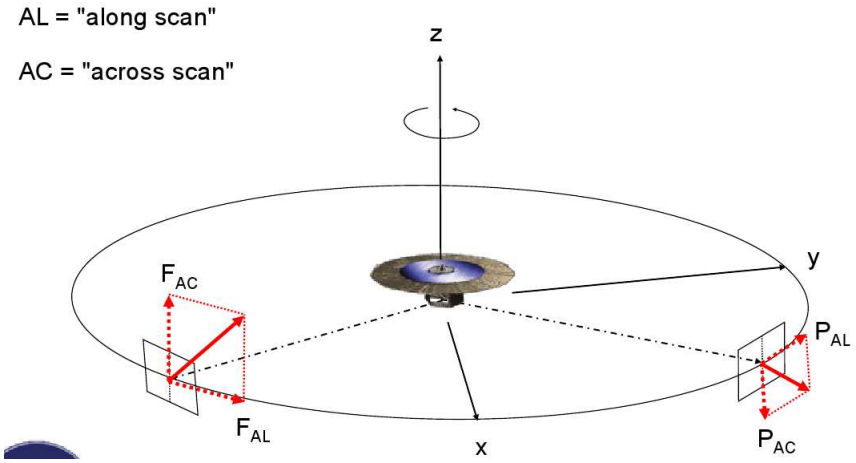

Figure 2.5: Gaia's spin axis and fiels of views. P refers to preceding field-of-view and F refers to following field-of-view. AL and AC refers to along scan and across scan, respectively. (Figure taken from Lindgren, 2010).

on the target brigthness, across column (AC) binning is possible, to improve the signal-to-noise (S/N) ratio and reduce the data volume for stars fainter than V $\sim$ 13 mag.

2.1.4 The Accuracy Of Gaia Measurements

Astrometry

The end-of-mission parallax standard error, averaged over the sky, for unreddened B1V, G2V, and M6V stars shall comply with the following requirements as listed in Tab. 2.3:

Magnitude	Stellar Spectral Type		
	B1 V	G2 V	M6 V
V<10 Mag	$<$ 7 μas	$<$ 7 μas	$<$ 7 μas
V=15 Mag	$<$ 25 μas	$<$ 24 μas	$<$ 12 μas
V=20 Mag	$<$ 300 μas	$<$ 300 μas	$<$ 100 μas

Table 2.3: Standard errors on Gaia parallaxes

Spectro-Photometry : RP/BP

The primary aim of the spectro-photometric instrument is to measure the spectral energy distribution of all observed objects, (i) to correct the centroid positions in the main astro-

metric field for systematic chromatic shifts, and (ii) to derive astrophysical characteristics, such as effective temperature (T_{eff}), mass, age, chemical composition for stars.

Low-Resolution Spectrophotometry	V[Mag]	B1V	G2V	M6V
BP	15	<10 mmag	<25 mmag	<100 mmag
	20	<150 mmag	<1000 mmag	- mmag
RP	15	<10 mmag	<25 mmag	<100 mmag
	20	<150 mmag	<1000 mmag	- mmag

Table 2.4: Standard errors on Gaia spectrophotometry

Spectroscopy : RVS

The RVS wavelength range (8470-8740 $\mathring{A}$) is a rich domain. The choice of the spectrograph wavelength range was motivated by a number of considerations (Munari, 1999), starting from the constrain on its width, to be limited to $\sim$ 300 Å. The stars to be observed with Gaia down to V $\sim$ 20 can be roughly represented by the proportions of spectral types as listed in Tab. 2.1.4.

O-B stars:	$\sim$ 2 10^6	G stars:	$\sim$400 10^6
A stars:	$\sim$ 50 10^6	K stars:	$\sim$300 10^6
F stars:	$\sim$230 10^6	M stars:	$\sim$ 55 10^6

According to the Tab. 2.1.4, the selected wavelength region must be close to the peak of the energy distributions of the RVS' most numerous targets, G-K type stars, and on its red side, to take reddening into account. In addition, the extinction in the red domain is roughly a factor of two smaller than in the V band. This will allow the probing of the Galactic disk over greater distances than would be feasible at 5500 $\mathring{A}$.

In F,G and K type stars the selected wavelength interval is dominated by three strong core-saturated ionized Calcium lines ($\lambda\lambda$ 8498.0, 8542.1, 8662.1 $\mathring{A}$). CaII lines appear at B8 and dominate throughout M8. This allows the measurement of radial velocities even at very low signal-to-noise ratios (i.e. $\sigma_{V_r} \sim 15$ kms^{-1} at S/N $\sim$ 1 per pixel for a K1 V type star) as well as in very metal-poor stars. Although the strength of the triplet lines decrease with increasing gravity, it nevertheless remains very strong in dwarf stars: their equivalent widths are larger than 3 $\mathring{A}$ for stars of spectral type F8 V to M6 V. The triplet is non-resonant and therefore will not be affected by contributions from the interstellar medium.

In late type stars, the RVS spectra also contains numerous unblended weak lines of astrophysical interest and in particular α-elements like SiI or MgI. In the coolest stars CN and TiO molecular transitions are visible, but no strong molecular bandhead is present.

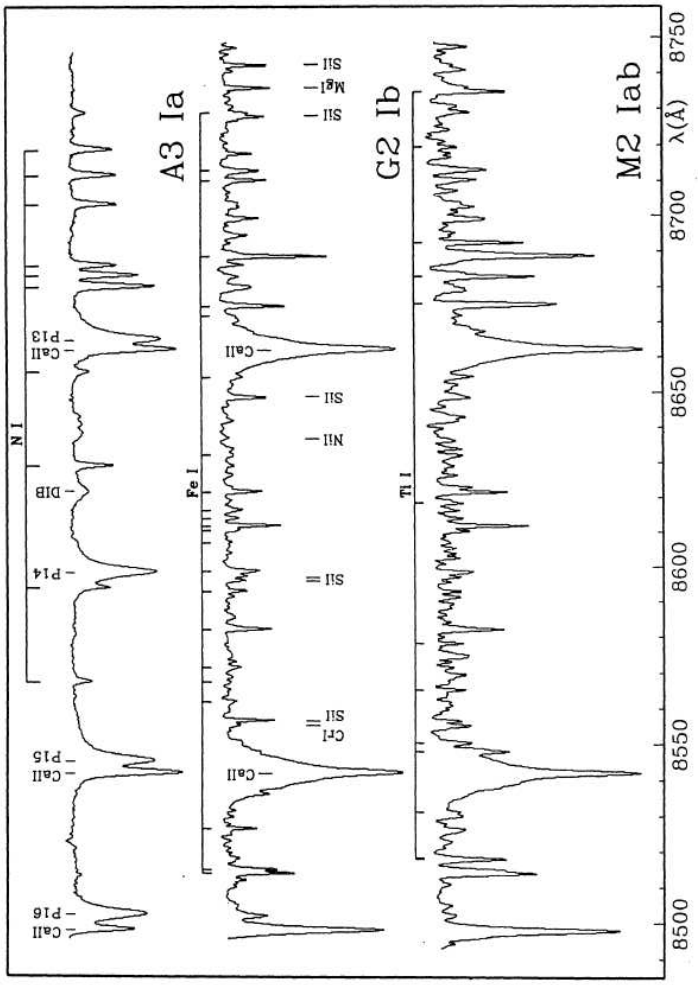

Figure 2.6: Spectra for A, G, M supergiants with identification of some of the strongest lines. Sequences of NI, FeI and TiI absorption characterize the A, G, M spectra, respectively. CaII lines become visible at B8 and dominate throughout the M stars, while the Pashen lines disappear at $\sim$ F8. Spectra are taken from the atlas of Munari & Tomasella (1999) covering the Gaia range at R_P= 20000 (Figure taken from Sordo, R. 2005, PhD. Thesis).

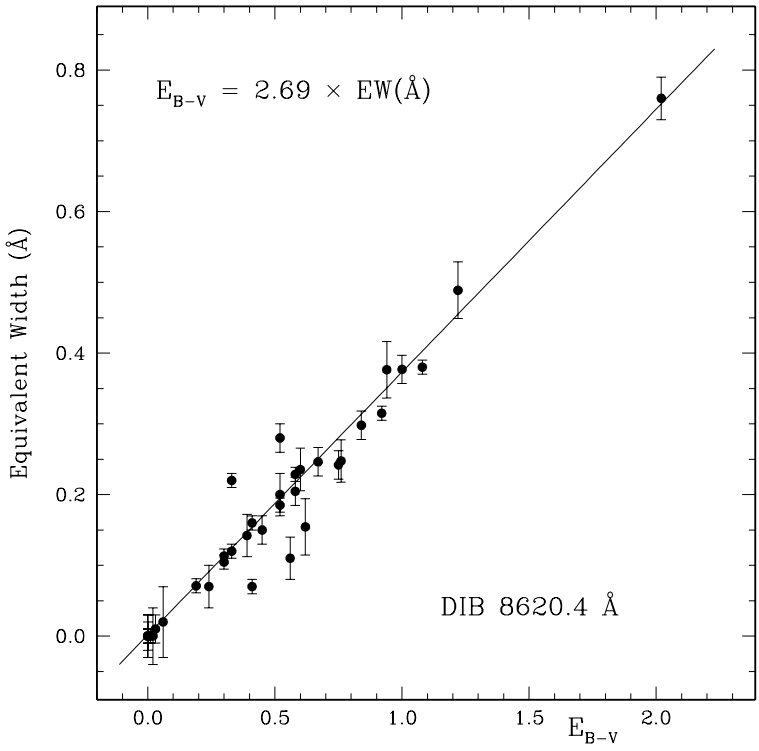

Figure 2.7: Correlation between the equivalent width of the diffuse interstellar band at 8620 $\mathring{A}$ and the reddening for stars widely spread in galactic coordinates and distance from the Sun (adapted from Munari 1999 and Munari et al. 1999) (Figure taken from Sordo, R. 2005, PhD. Thesis).

In early type stars, this spectral region is dominated by lines of the Hydrogen Paschen series, whose equivalent widths are strongly anti-correlated with gravity. The Paschen lines are visible even in very rapidly rotating stars. The spectra of hot stars also exibit some other strong (e.g. Ca II, N I) and weak (e.g. He I, He II) lines.

It addition, the spectral range contains a diffuse interstellar band (DIB), located at λ8620 $\mathring{A}$, which appears to be a reliable tracer of interstellar reddening (Munari 1999). Figure 2.7 shows the relation. This will be used, together with the photometric data, to derive a three-dimensional map of Galactic interstellar extinction.

In Tab. 2.5 the end-of-mission radial velocity (RV) robust formal errors,for unreddened B1V, G2V, and K1 III MP (MP = metal-poor) stars shall comply with the following requirements:

Spectral Type	V [Mag]	RV Error (km s −1)
B1 V	7	< 1
	12	< 15
G2 V	13	< 1
	16	< 15
K1 III MP	13.5	< 1
	16	< 15

Table 2.5: Standard Errors on Gaia Radial Velocities

2.2 The Classification of Gaia objects

In the first passage, Gaia will make use of the GSC2 as input catalog, mainly to identify bright stars. As Gaia performs real time detection, the intrinsic properties of most of the objects that are entering in the Gaia's fields of view will not be known. The first part of the Gaia data processing requires classifying everything observed. If we consider the amount of data that Gaia will collect, we can conclude that the data processing clearly requires automated classification and parameterization methods for the detected sources.

In the Gaia project, the classification algorithms are base on both supervised and unsupervised methods (see Bailer-Jones et al., 2008; Smith et al., 2008), first producing a discrete classification of the objects, i.e. dividing objects having higher probability of being stars, galaxies, and QSOs, then estimating the astrophysical parameters of all the stars and at some extent also of the galaxies, by comparison with a set of templates. Finally, the treatment of the outliers will rely on unsupervised methods.

The Discrete Source Classifier (DSC) is the algorithm producing the first discrete classification. It currently uses epoch-combined BP/RP data, supplemented with astrometry where available.

QSO detection. The primary goal of Gaia classification is related to the QSO detection, which is fundamental to build the astrometric reference frame. Present QSOs catalogs are mainly based on radio positions. Their accuracy is not sufficient to calibrate Gaia's astrometry. Instead, the large number of quasars observed by Gaia over the whole sky will define its own reference frame (Bailer-Jones et al., 2008). Thus, it is fundamental to identify a clean sample of Quasars. Gaia mission will allow a realization of the International Celestial Reference System (ICRS) based on optical detection and more accurate by two or three orders of magnitude than the present system (Ma et al., 1998; Kovalevsky et al., 1997).

Estimation Of The Astrophysical Parameters For single stars, the goal of the Gaia classification is to provide parameters such as T_{eff}, surface gravity ($\log g$), metallicity ([Fe/H]), interstellar extinction (A_V using BP/RP data down to V$\sim$20. Using the spectroscopy from the RVS instrument, other parameters can be derived such as: radial velocity for stars brighter than V$\sim$ 16, α-process element abundances ($[\alpha/Fe]$), CNO abundances, rotational velocity for stars brighter than V$\sim$ 12 mag. Gaia photometry will allow to estimate T_{eff} to an accuracy of 3% at V= 15 mag and 4% at V= 20 mag for unreddened stars. [Fe/H] and $\log g$ can be estimated with accuracies of $0.1 - 0.4$ dex for stars with $V \leq$ 18.5 mag, depending on the spectral type. The extinction is expected to vary over a wide range ($A_V = 0 - 10$ mag), especially on the Galactic plane. $\log g$ and [Fe/H] can still be estimated with an accuracy of 0.3 and 0.5 dex, respectively, at V= 15 mag, but much poorer accuracy will be reached at V= 18.5 mag. The degeneracy in T_{eff} and A_V will seriously hamper the estimates at faint magnitudes for heavily reddened stars. The summarized information of the astrophysical parameter precisions can be found in Tab. 2.6.

	Instrument	V[Mag]	Accuracy
Effective Temperature	BP/Rp	16	1% to 5%
Surface Gravity	BP/RP	16	0.1 to 0.4 dex
Metallicity	BP/RP	16	$\sim$ 0.2 dex
Extinction	RVS	Hot stars	0.05 to 0.1 mag

Table 2.6: Expected precision of astrophysical parameters

Unresolved Galaxy Classifier For point-like unresolved galaxies, Gaia classification provides the taxonomy and some specific astrophysical parameters from the BP/RP spectrum, such as star formation rate, redshift, and extinction (Bellas-Velidis et al.,2010).

2.3 The Final Catalogue

The final catalogue is expected to be published at the end of the mission, around 2021, with intermediate data releases produced during the operational phase. Gaia catalogue will provide as much astrophysical information as possible for each source, derived from the combination of all Gaia measures.

The catalogue will also contain intermediate data which allow a reprocessing of the observations. In particular the astrophysical parameters can be improved by incorporating complementary information obtained from other surveys or follow-up observations. For astrometric data, reprocessing is relevant for multiple sources with uncertain solutions (which can be improved by incorporating follow-up radial velocity observations). Hence the Gaia catalogue will not be a static release but will evolve over the time as more informations are added to it (Brown, 2008).

2.4 The Importance of training data

Supervised methods require the comparison with a set of templates, either observed or synthetic, as training data. Observational stellar templates importance is twofold: first they can be used as reference stars that once observed by Gaia will be used to calibrate the performances of the classification algorithms. Second, they can provide libraries of spectra with well known parameters to improve the synthetic spectra. The algorithm calibration procedures are necessary to be able to achieve the expected accuracy on the atmospheric parameter determination.

Stars of F,G,K spectral types will be the most numerous among the objects observed by Gaia. Therefore their atmospheric parameter calibration will be crucial for achieving the Gaia goal of studying the structure and evolution of the Galaxy. On the other hand the

RVS will provide useful data for both atmospheric parameter determination and radial velocity determination only for stars brighter than about 11^{th} to 13^{th} mangnitude. Thus, stars which fall within both the spectral type and magnitude limits will be optimal sources for testing, training and calibrating the parametrization algorithms before and after the lunch of Gaia.

There has been a great effort inside the Gaia community to provide ground based observations of all types of stars to test the classification and parametrization algorithms using BP/RP (Blue/Red Photometer) and RVS (Radial Velocity Spectrometer). Taking into account the requests and the capability of the instruments, Red Clump stars seems to be useful candidates to use as reference stars and/or training data.

Chapter 3

The Red Clump Stars

Red Clump stars display properties that make them a primary tool to investigate Galactic structure and kinematics :

- their absolute magnitudes shows minimal dispersion at both optical and infrared wavelengths.
- they are intrinsically bright and observable thoroughout most of the Galaxy.
- their spectral types mainly range from G8III to K2III.
- their spectra comprise strong absorption lines.

Those specific properties of Red Clum stars make them ideal sources to measure accurate radial velocities and atmospheric chemical abundances. Thus, they have been the subject of many kinematical and structural studies of Galaxy and it's vicinity in the literature.

3.1 The Structure And The Evolution Of the Red Clump

The Red Clump is mainly composed by low-mass stars (below $\sim 2.3\ M_{\odot}$) in the stage of central helium burning phase, following He ignition in an electron-degenerate core

During the main sequence phase, because of the absence of con- vection, the star burns hydrogen more rapidly in the core than in the outer regions, so there is a chemical gradient with hydrogen decreasing toward the center. After central hydrogen burning, the star has develop a helium core, which, in the absence of energy sources, tends to be isothermal. The central hydrogen burning moves into a shell that moves outwards. The shell become thinner as it moves outside, the core contracts and the envelope expands.

When the star reaches the Hayashi line, the envelope become convective, the luminosity increase while the T_{eff} is constant: in the HR diagram the star is rising the Red Giant

Branch (RGB). At the end of the RGB, low-mass stars ignite helium in a degenerate shell through a relatively strong helium flash and then quiescently burn it in a convective central region.

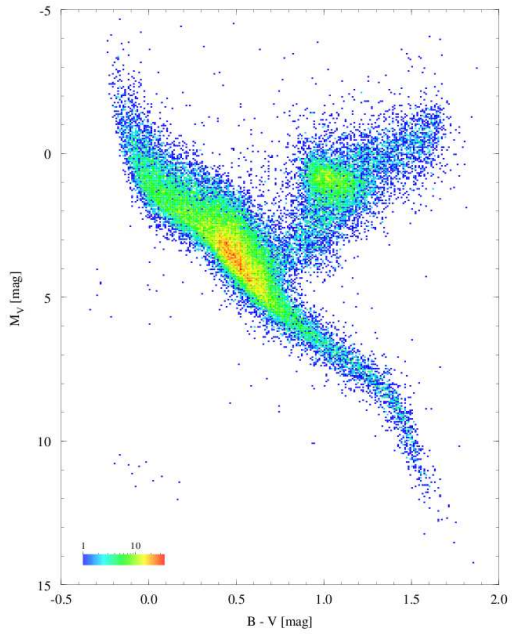

Figure 3.1: Hertzsprung-Russell (M_V, B−V) diagram for the 41704 single stars from the Hipparcos Catalogue with relative distance precision $\sigma_\pi/\pi < 0.2$ and $\sigma_{(B-V)}$ less than or equal to 0.05 mag. Colours indicate number of stars in a cell of 0.01 mag in (B−V) and 0.05 mag in V magnitude (M_V).

The onset of electron degeneracy after the central hydrogen-exhaustion postpones the He-ignition until the core mass grows to about $Mc \sim 0.45\ M_\odot$. Since the He-flash in a degenerate gas starts at $Mc \sim 0.45 \div 0.55\ M_\odot$ for low-mass stars (except for a little dependence on metallicity), thus they tend to have the same superficial luminosity. The small range of luminosities reflects the small range of core mass at the moment of helium ignition. That is confirmed by CMDs of Globular Clusters: all RGB finish at the same luminosity (Girardi, 1999).

After the helium flash, the new source of energy from the core pushes the hydrogen fusing shell outwards and forces it to cool. Now the star is generating new energy by helium burning in it's core, the core shrinks back, thus the star winds up on the horizontal branch (HB). In CMDs, these stars share a very narrow distribution in luminosity, but may have a large extension in temperatures. The temperatures on HB depends on the metallicity and hydrogen rich envelop masses. Red Clump considered the high-metallicity and high envelope mass counterpart of the horizontal branch.

3.2 Red Clump Stars In The Literature

Among countless more, we will refer some of the recent examples of applications of Red Clump stars to Galaxy investigation: the peculiarities of Galactic rotation (Rybka et al. 2008), the stellar bar in the inner Galaxy (Cabrera-Lavers et al. 2007), the Galactic Bulge (Nataf et al. 2010), the vertical distribution of disk stars in terms of kinematic and metallicity (Soubiran et al. 2003), the surface mass density in the Galactic plane (Siebert et al. 2003), the origin of the Thick disk (Ruchti et al. 2010), the surface mass density in the Galactic disk (Bienayme et al. 2006) and age-metallicity relation (AMR), age-velocity relation (AVR) (Soubiran et al. 2008), tidal streams in solar neighborhood (Famaey et al. 2005, Antoja et al. 2008), Galactic substructures (Correnti et al. 2010, Law et al. 2010).

The large proportion of RC stars observed by the ongoing RAVE survey (Steinmetz et al. 2006, Zwitter et al. 2008), and the accurate distances derived for them (Zwitter et al. 2010), support a great potential of the RAVE data base in progressing towards a better understanding of how the Galaxy formed, structured and evolved (Freeman & Bland-Hawthorn 2002, Siebert et al. 2008, Veltz et al. 2008, Kiss et al. 2010).

In literature, spectroscopic surveys of Red Clump stars generally focus on their atmospheric parameters or radial velocities, but not on both at the same time (the exception of the Rave survey and Mischenina et al. (2006)). A very recent spectroscopic survey of Red Clump stars with high resolution spectroscopy has been published by Valentini & Munari (2010). Here we peresent an extension, fainter magnitudes thus distant targets, of the spectroscopic survey of RC stars of Valentini & Munari (2010) that are both aimed to construct a catalog of accurate radial velocities and atmospheric parametes combined with available photometric and spectrophotometric informations in the literature for well selected Red Clump stars in the solar neighbourhood.

Chapter 4

Target Selection and The Input Catalog

The input catalog for our survey consist of meticulously selected Red Clump stars, distributed along the great circle of celestial equator and away from galactic plane. In this chapter, we discussed the selection criteria in detailed in terms of astrometric, photometric and spectroscopic characteristics.

4.1 Target Selection Criteria

The Red Clump stars constitute our input catalog are selected from Hipparcos catalog (1997) to provide a homogeneous sample of genuine, un-reddened stars that are easily observable from northen latitudes of Astrophysical Observatory of Padova, and being fainter by ≥ 1 magnitude (and consequently more distant) than ones in Valentini & Munari (2010) and other similar surveys of Red Clump stars in the literature.

Fig. 4.1 and Fig. 4.2 shows the aitoff projection in both equatorial (Fig. 4.1) and galactic (Fig. 4.2) coordinates of input catalog stars. Fig. 4.3, shows the distribution of the magnitudes and spectral type of our survey stars in comparison with the other surveys of Red Clump stars in literature. It can bee seen that, our surveys stars are fainter by ≥ 3 magnitude from than the surveys of Mishenina et al.(2006), Hekker & Melendez (2007), and Takeda et al. (Takeda et al., 2008).

The first selection criteria that we applied to constitute our input catalog was concerned the spectral type and the positions on the sky of the target stars. Red Clump stars have spectral types between G8III and K2III. Thus we choose stars from Hipparcos [1] catalog have spectral types in this range. Then, we cross-checked the spectral types of the selected stars from the Michigan Project.

[1] All selection criteria involving Hipparcos information refer to the original catalog published by ESA in 1997, not necessarily its revision by van Leeuwen (2007)

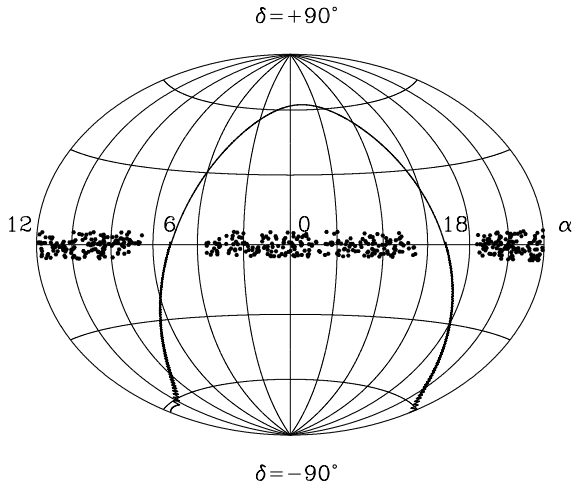

Figure 4.1: Aitoff projection in Equatorial coordinates of our target stars. The thick line represents the Galactic equator.

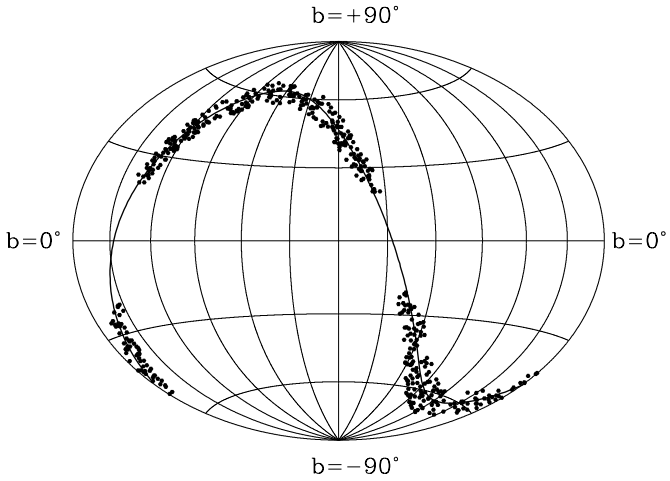

Figure 4.2: Aitoff projection in Galactic coordinates of our target stars.

Michigan Project catalog is the most complate and homogeneous compilation of spectral classifications. It contains all the Henry Draper Catalogue (HD) stars in the declination range $-12°$ up to $+6°$ (Houk & Swift, 2000 (Houk and Swift, 2000)). We only considered stars with:

- accurate spectral classification (quality index ≤ 2 in Michigan catalog),
- a declination within $-/+6°$ of the celestial equator (easily observable from Asiago),
- a Galactic latitude $\mid b \mid \geq 25°$ (avoid the reddening close to the Galactic plane).

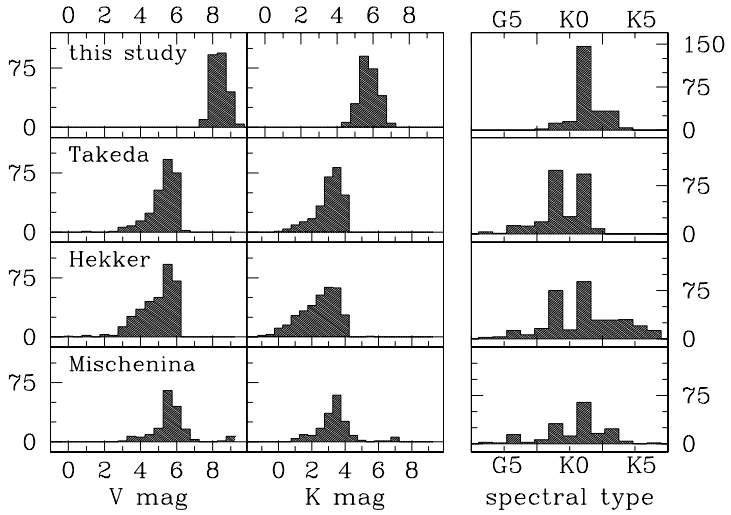

Figure 4.3: Distribution in V and K magnitudes and spectral type of our target stars and the other surveys of Red Clump stars in the literature: Takeda et al. (2008), Hekker & Melendez (2007), Mishenina et al. (2006).

Then we continued with astrometric and photometric selection criterias:

- valid entries in both Hipparcos and Tycho-2 catalogs,
- non-negative paralaxes in Hipparcos catalog,
- no binarity or variability flag in Hipparcos catalog,
- be present in the 2 MASS catalog,
- within the magnitude range $7.5 \geq V \leq 9.5$.

Finally, we considered Red Clump stars in other spectroscopic surveys, and eliminated stars that are already present in the Geneva-Copenhagen (Nördstrom et al. (2004) survey and the radial velocity survey of giant stars by Famaey et al. (2005).

These selection criterias mentioned above provided a total of 500 Red Clump stars. By the end of June 2010, we observed 245 of our target stars, and 60 of those had been observed at two distinct epochs. Fig. 4.4 shows the the properties of observed 245 Red Clump stars from our survey in comparison with 207 observed Red Clump stars from Valentini & Munari (2010) survey.

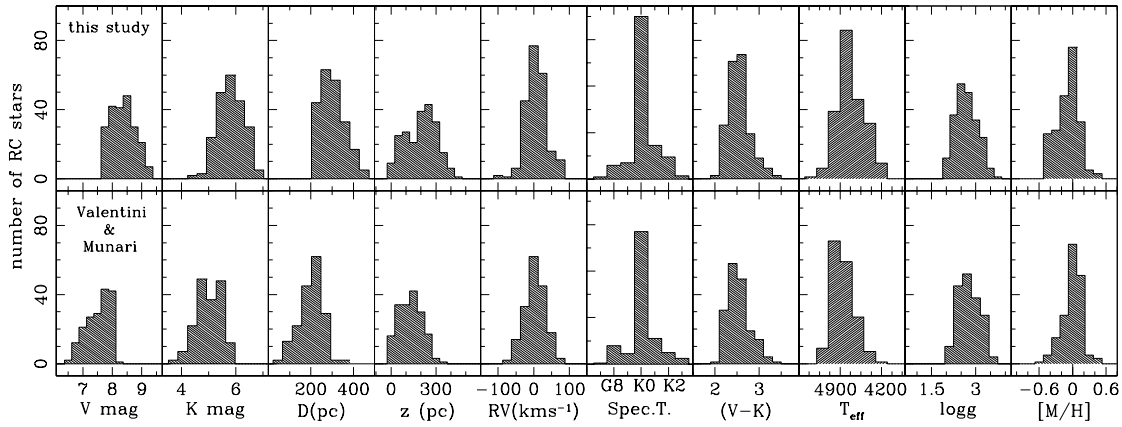

Figure 4.4: The comparison of the properties for Red Clump stars in Valentini & Munari (2010) spectroscopic survey and in this study.

Chapter 5

Observations And Data Reduction

5.1 The B&C Spectrograph At The 1.22 meter Telescope In Asiago

The 1.22 meter telescope of University of Padova Department of Astronomy is located at an altitude of 1045 meters in Asiago. The Cassegrain Focus of the telescope is $f/16$ and the scale is 10.78 arcsec/mm. It is equipped with a Boller & Chivens spectrograph (hereafter B&C) belonging to the INAF Astronomical Observatory of Padova. Fig. 5.1, shows the basic layout of 1.22 meter telescope with a schematic description.

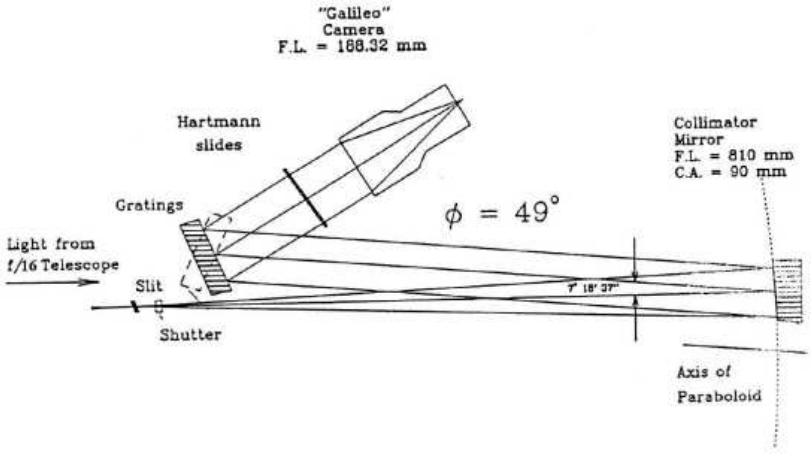

Figure 5.1: Schematic Description For The Instruments

The basic optical layout of the B&C spectrograph is a long-slit with an aperture variable up to more than 12 arcsec and a length of 5.0 arcmin, is located at the Cassegrain focus focal plane. The side of the slit turned to the incoming light beam has a reflecting surface

Table 5.1: Andor IDUS 440A Technical Data

Detector	E2V 42-10BU Back Illuminated
Active Pixel Array	512 × 2048
Pixel Size (μm)	13.5 × 13.5
Image Area (mm)	6.9 × 27.6
ReadOut Noise	3 e^-
Gain	1.4 e^-/ADU
Dark Current ($-70°C$)	0.004 $e^-/pixel/sec$

Table 5.2: List of available gratings and their characteristics

Grooves ln/mm	Blaze Angle	Blaze Wavelength $\mathring{A}$	Dispersion $\mathring{A}/pix$	$\Delta\lambda$ $\mathring{A}$
150	2°09′	5000	4.82	9820
300	4°18′	5000	2.41	4910
600	8°38′	4500	1.21	2460
1200	26°45′	6825	0.60	1230

which is viewed by a guiding tv camera that relay to a guiding tv screen field of view in the control room. An off-axis parabolic mirror with a diameter of 90 mm and a focal length of 810 mm ($f/9$) serves as beam collimator to the grating.

The dispersed light beam is directed to the Dioptric Blue Galileo Camera, having a focal length of 188 mm and currently coupled to the Andor IDUS CCD Detector which features a 2048 ×512 active pixel array with a pixel size 13.5×13.5 μm. CCD detector covers an image area of 6.9 ×27.6 mm. The principal characteristics of the CCD detector camera are summarized in Tab. 5.1.

The reflecting surface of the slit is viewed by a Andor iXon DV885 guiding camera, that covers a field-of-view of $5.2' \times 3.7'$. The spatial scale of the imaged field is $0.43''/pixel$.

To perform wavelength calibration an hollow cathode [Fe-Ar] comparison lamp is available. Presently, new comparison lamps are going to be available at the calibration set of the telescope.

There are four gratings available with the B&C spectrograph. Dispersion range from 4.8 to 0.6 $\mathring{A}/pix$. Gratings can be changed. Tab. 5.2, summarizes the main characteristics of the four gratings.

Among these available gratings, for our purpose on accurate RV determination we used 1200 ln/mm grating, with a slit with of 200 μm. This provided a resolving power of 5500. The blaze angle chosen as $20°25'$ gives a dispersion of 0.603 $\AA/pix$ and a wavelength coverage of $4750-5950$ $\AA$. The main selection of the wavelength range will discussed in the next sections.

5.2 Softwares To Use The 1.22 meter Telescope

The CCD detector and the guiding system are run with two different computers located in control room. The software *PyIDUS* for operating the CCD detector is working on a *Linux* based computer. There has been alot of effort to make the software user-friendly in last months. The latest version of *PyIDUS* works interactively with *IRAF*. This software allows switch-on and connect to the CCD detector, cool-down and warm-up the CCD from the control room. It also writes the key parameters (object type, i.e. object, calibration lamp, bias, flat, object name,exposure time) and the parameters of the telescope set up(sky coordinates,air mass,grating, blaze angle, slit width, position angle) and observation date, name of the observer to the image headers directly. The *PyIDUS* software also make allowances to control of the images with a *DS9* window at the end of the exposure time.

The software *Guide* is for operating the guiding system works on a *Windows* based computer. This software cools-down and warms-up the guiding camera from the control room. The *Guide* can run in two modes, a video mode to place the target object on the slit and a photo mode to select and guide on a field star. After starting the exposure time from *PyIDUS*, it allows to monitorize the position of the target star on the slit and the goodness of the guiding with giving the displacement of the target star on the slit in pixel coordinates and the FWHM values for the guide star. The values of the FWHM is also related to the goodness of the seeing conditions during the exposure time.

There is a third computer for running the *TPS*. The software *TPS* programme allows to monitor the pointing coordinates of the telescope and the star. It is also possible to run *TPS* simultaneously with *Guide 8.0* software which uses the new *Tycho-2 Catalog* of stars, clusters and galaxies.

5.3 Data Acquisition At The Telescope

Observations were obtained in between years 2008 and 2010 at different time intervals, in both summer and winter periods. The first period of the observations were dedicated to obtain Radial Velocity standard star's spectra for accuracy tests on radial velocity determination via cross-correlation between two spectra of each radial velocity standard star and will discussed in detailed later. The second period of the observation campaign were dedicated to the selected Red Clump stars in our observational program.

Each night's run is started with mandatory pipe-line of the instruments at the telescope.

Cooling-down the temperature of the CCD detector and stabilized at $-80\ ^{\circ}C$. Same application for the Guiding System that stabilized at a temperature of $-70\ ^{\circ}C$. Cool-down a CCD to at least $-80\ ^{\circ}C$ and more, its dark current can be neglected if also the CCD camera has very stable temperature regulations. The telescope was initialized by pointing it on a well known bright star.

We emphasis on several points to minimize and if possible, to avoid the errors originated during the observations:

- The placement of the stars on the slit. After bringing the target star on the center of the slit, we keep the target centered on the slit along the all exposure time and we monitored the excess light of the target star reflected off both sides of the slit. It is very important to be able to get the same amount of light from the same area of the target star along the exposure.
- The placement mismatches between different exposures of the same target. To obtain the same part of tracing and the background for different exposures of the same target. The target's path in the direction of dispersion in different exposures are very important in the case of combining them in one spectrum.
- The time interval between the first and the second exposure of the target. To minimize the replacement of the target stars position on the slit we try to keep the time interval between the 2 exposures as short as possible.
- The duration of the exposure times and the level of the S/N ratio. The total exposure time on a given target it depends on the required signal-to-noise ratio. Since our target stars are faint (V mag between $7-10$) we determined the most convenient exposure time according to the maximum counts and the S/N ratio achieved after a given exposure. During our observation campaign, we used the same exposure ($600-900$ sec. at the faint end) times for all the target stars.
- The variations of the target star's position on the slit and the guide star due to the changes of the seeing conditions during the given exposure. Our auto-guider system provide us to guide on a selected star off the slit in the guider camera's field. With the auto-guider tools we carefully monitored the changes of both the guide star, the target star, and sudden changes on the weather conditions to be sure that during the exposure time our target star's position on the slit is stable.

As discussed in detailed at Munari & Lattanzi (1992), another thing on which we had to pay attention during the observations was to control of the *spectrograph flexures*. They occurs as the telescope moves during the exposure or slews from the target to a another star. *Spectrograph flexures* are a dominant and a systematic biasing factor in radial velocity determination. To minimize the effects of the *spectrograph flexures*, we exposed the comparison spectrum immediately before and after each science target observation. Another advantage of this procedure is also minimizing the wavelength calibration errors. Because in this way, the calibration equations from the two comparison spectrum taken

at the beginning and at the end of the target spectrum can be interpolate to the time of targets observation.

As explained in the previous section, we also took advantage of the *PyIDUS* software that works interactively with *IRAF* during our observations. This gave us the ability to control and examine the scientific spectrum at the end of exposure time. If needed, to check and revised the spectrum, the S/N ratio at the end of exposure and to decide if it is necessary or not to take a new exposure for the same target.

5.4 Selecting The Wavelength Interval To Observe

As we already mentioned, Red Clump giants are helium burning, late-G and K spectral type of intermediate age stars. Thanks to their strong-lined spectra they are well adopted to the measure of accurate radial velocities and atmospheric parameters. The wavelength range that we choose for our observations ($4760-6000$ $\mathring{A}$) contains key, well-known features that are applicative for both radial velocity and atmospheric parameter determination for our target stars. Among these lines, we discussed the strongest features.

At 4862 $\mathring{A}$, there is Hβ line. The most basic study of stellar spectra makes it clear that the hydrogen lines are sensitive indicators of the physical conditions in the stellar atmospheres. The Balmer lines of the hydrogen atom, play a key role in spectral classification. Since the classifications may indicate not only the surface temperature and gravity of the star, but also in many cases, they indicate the abundances. Because Balmer lines are commonly seen in the spectra of various objects, they are commonly used to determine radial velocities due to Doppler shift.

In the middle of our wavelength range there are MgI-b lines (5167, 5173 and 5184 $\mathring{A}$). The MgI-b lines are among the strongest features in the spectra of our target objects because these lines falls at a wavelength which K spectral type stars has the peak of the energy distribution. Mg features shows a bi-parametric behavior as a function of metallicity and gravity.

And at the final part of our wavelength range, there are NaI $D_{1,2}$ lines (5890 and 5896 $\mathring{A}$) which are an interstellar absorption lines and also one of the strongest features in the spectra of our target stars. These lines are created when cold interstellar gas absorbs some of the radiation emitted by the distant star. They tend to be much sharper and more narrow than the absorption lines created in the atmosphere of the star, and indicates the temperature, density and chemical composition of the interstellar gas through which the light has passed. An example of our wavelength range can be seen in Fig. 5.2.

Since we experienced some complexity on continuum normalization in the range of MgI-b lines (5167, 5173 and 5184 $\mathring{A}$), we decided to try another wavelength range to observe for our survey. To avoid the MgI-b lines we moved 800 $\mathring{A}$ to the red. An example of our second wavelength range that we tested can be seen in Fig. 5.3. It is clear that we smoothed away the complexity of MgI-b, but we left behind strong and useful features.

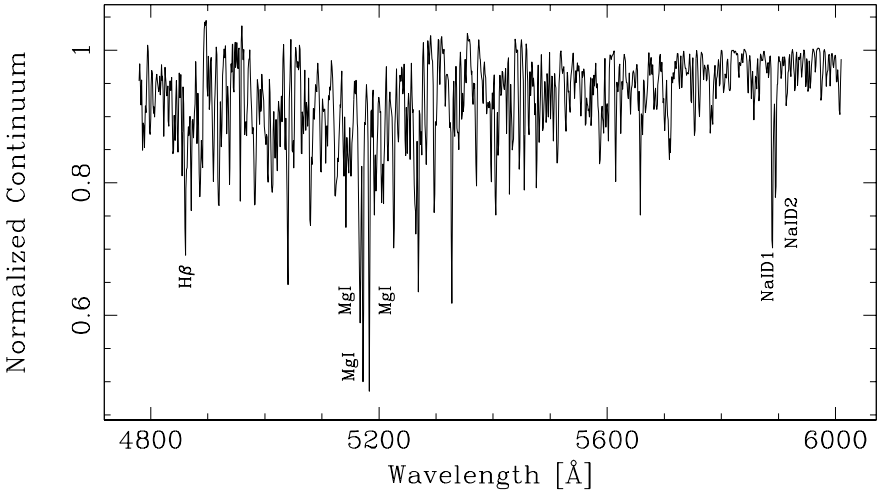

Figure 5.2: Synthetic spectrum of a star with T_{eff}=4750,$\log g$=2.5 and [M/H]=−0.5 to give an example of the wavelength that we observed.

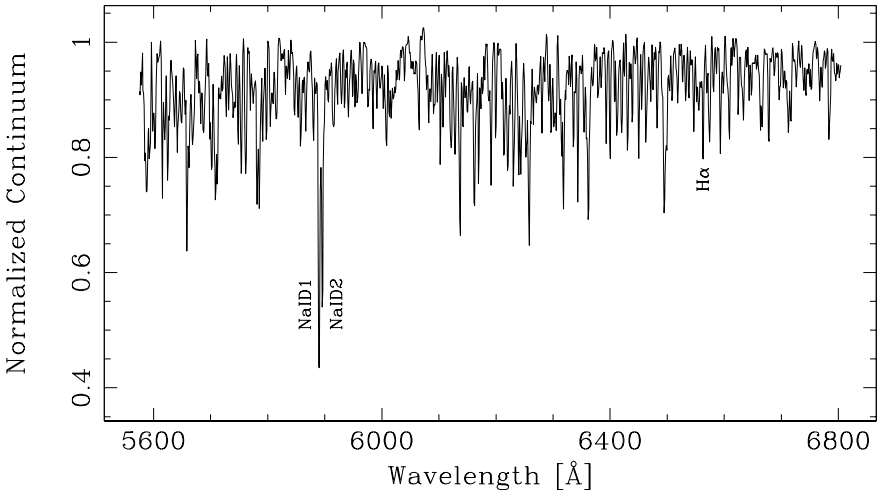

Figure 5.3: Synthetic spectrum of a star with T_{eff}=4250,$\log g$=1.5 and [M/H]=+0.0 to give an example of the wavelength that we observed.

Table 5.3: Observed Red Clump Giants from Takeda et al. (2008)

HD	Spec.T.	Alpha	Delta	V	T_{eff}	Logg	[Fe/H]	Note
		$h\ m\ s$	$\circ\ '\ ''$	mag.	K			
448	G9 III	00 09 02.34	+18 12 43.3	5.57	4780	2.51	+0.03	B&R
2952	K0 III	00 33 10.32	+54 53 42.3	5.93	4844	2.67	+0.00	R
3817	G8 III	00 41 07.20	+39 27 31.2	5.30	5041	2.52	−0.12	R
4627	G8 III	00 48 17.34	+07 17 59.7	5.92	4599	2.05	−0.20	B&R
5608	K0 III	00 58 14.19	+33 57 03.8	5.99	4854	3.03	+0.06	R
6186	K0 III	01 02 56.66	+07 53 24.3	4.27	4829	2.30	−0.31	B&R
7087	K0 III	01 11 27.19	+21 02 04.8	4.66	4908	2.39	−0.04	B&R
10348	K0 III	01 41 39.24	+30 02 49.7	5.97	4931	2.55	+0.01	R
10761	K0 III	01 45 23.59	+09 09 27.5	4.26	4952	2.43	−0.05	B&R
11037	G9 III	01 48 26.02	+03 41 07.5	5.91	4862	2.45	−0.14	B&R
13468	G9 III	02 11 35.84	−01 49 31.3	5.94	4893	2.54	−0.16	R
19525	G9 III	03 08 38.79	+08 28 15.2	6.28	4801	2.59	−0.11	B&R
192787	K0 III	20 15 23.79	+33 43 45.7	5.70	5025	2.86	−0.07	B
192944	G8 III	20 16 47.08	+24 40 16.1	5.30	4981	2.48	−0.06	B&R
209396	K0 III	22 03 16.43	−06 31 20.7	5.55	4999	2.81	+0.04	B&R
210434	K0 III	22 10 33.70	−04 16 00.7	5.98	4949	2.93	+0.12	B&R
219615	G7 III	23 17 09.49	+03 16 56.1	3.70	4802	2.25	−0.62	B&R
223252	G8 III	23 47 56.49	−02 45 41.8	5.49	5031	2.72	−0.03	B&R
224533	G9 III	23 58 40.41	−03 33 20.9	4.88	5030	2.73	−0.01	B

To test the performance of our χ^2 method (the detailed description of the χ^2 technique and the accuracy tests with the literature data will be discussed in Chapter 7) for atmospheric parameters determination at this two wavelength ranges, we observed 19 Red Clump giants from Takeda et al. (2008) and 23 Red Clump giants from Hekker & Melendez (2007) using both blue (4750−5950 $\mathring{A}$) and red (5550−6800 $\mathring{A}$) wavelength range. A list of observed Red Clump giants from two catalog can be found in Tab. 5.3 and Tab. 5.4. The last column of the tables (note) refers to the observations done with just the blue wavelength range (B), just the red wavelength range (R) and both with the blue and red wavelength ranges (B&R).

Since we wanted to apply a preliminary test to select the most consistent wavelength range, we implement five different solutions for atmospheric parameters in our χ^2 method (the reason for different solutions from different wavelength interwals will be discussed in

Table 5.4: Observed Red Clump Giants from Hekker & Melendez (2007)

HD	Spec.T.	Alpha	Delta	V	T_{eff}	Logg	[Fe/H]	Note
		$h\ m\ s$	$\circ\ \prime\ \prime\prime$	mag.	K			
3817	G8 III	00 41 07.18	+39 27 31.2	5.30	5025	2.65	−0.009	R
4627	G8 III	00 48 17.41	+07 17 59.7	5.92	4600	2.30	−0.015	B&R
6186	K0 III	01 02 56.61	+07 53 24.5	4.27	4900	2.70	−0.014	B&R
7087	K0 III	01 11 27.22	+21 02 04.7	4.66	4850	2.55	−0.009	B&R
7318	K0 III	01 13 44.95	+24 35 01.4	4.67	4815	2.55	−0.006	B&R
8763	K1 III	01 26 41.68	+19 14 25.5	5.50	4690	3.00	−0.001	R
10348	K0 III	01 41 39.24	+30 02 49.6	5.97	4885	2.60	−0.003	R
10761	K0 III	01 45 23.63	+09 09 27.8	4.26	5025	2.90	+0.000	B&R
13468	G9 III	02 11 35.83	−01 49 31.5	5.94	4925	2.80	−0.007	R
16161	G8 III	02 35 52.47	+05 35 35.7	4.87	5170	2.75	−0.011	R
184406	K3 III	19 34 05.35	+07 22 44.2	4.45	4670	3.20	+0.002	B&R
190327	K0 III	20 04 08.32	+07 16 40.7	5.51	4850	2.70	−0.009	B&R
192944	G8 III	20 16 47.09	+24 40 16.0	5.30	5000	2.70	−0.006	B&R
197912	K0 III	20 45 39.75	+30 43 11.0	4.22	4940	3.17	−0.002	B&R
197989	K0 III	20 46 12.68	+33 58 12.9	2.48	4785	2.75	−0.006	B&R
199253	K0 III	20 55 36.69	+13 43 17.5	5.19	4625	2.35	−0.011	B&R
209761	K2 III	22 05 11.33	+26 40 25.3	5.75	4420	2.35	−0.005	B&R
210762	K0	22 12 08.09	+24 57 02.3	5.97	4185	1.65	+0.000	B&R
213119	K5 III	22 29 07.98	+09 07 44.5	5.60	4090	1.65	−0.029	B&R
214995	K0 III	22 41 57.46	+14 30 59.0	5.92	4680	2.70	−0.002	B&R
219615	G7 III	23 17 09.94	+03 16 56.2	3.70	4940	2.90	−0.032	B&R
223252	G8 III	23 47 56.54	−02 45 41.8	5.49	5000	3.00	−0.005	B&R
224533	G9 III	23 58 40.38	−03 33 21.5	4.88	5115	3.30	−0.001	B

Chapter 6 in detailed). Those solutions diverge from each other in the wavelength interval. The restrictions that we applied while selecting the different solutions are:

- For the blue wavelength range
  (1) $4760 \leq \lambda \leq 6000$ Å
  (2) $4760 \leq \lambda \leq 5300$ Å
  (3) $5300 \leq \lambda \leq 5880$ Å
  (4) $4975 \leq \lambda \leq 5285$ Å
  (5) $\lambda \geq 4815.0$ Å& $\lambda \leq 4975.0$ Å$\| \lambda \geq 5285.0$ Å& $\lambda \leq 5950.0$ Å

- For the red wavelength range
  (1) $5560 \leq \lambda \leq 6800$ Å
  (2) $5560 \leq \lambda \leq 6200$ Å
  (3) $6100 \leq \lambda \leq 6800$ Å
  (4) $\lambda \leq 5880$ Å$\| \lambda \geq 5905$ & $\lambda \leq 6550$ Å$\| \lambda \geq 6570$ Å
  (5) $\lambda \leq 5865$ Å$\| \lambda \geq 6007$ & $\lambda \leq 6271$ Å$\| \lambda \geq 6593$ Å

We derived the atmospheric parameters for the selected stars in both blue and red wavelength range with five different methods for atmospheric parameters solutions as mentioned above. In Fig. 5.4 and Fig. 5.5, we show the differences between literature values and derived values from our χ^2 for T_{eff}, logg, and [M/H]. Fig. 5.4 represents the parameters derived from the blue wavelength and Fig. 5.5 from the red wavelength. The mean, and σ values of the differences can be seen in Tab. 5.5, that are calculated from the mean values of the five different solutions for two wavelength intervals.

From our preliminary analysis, the atmospheric parameters derived with blue wavelength (4750−5950 $\mathring{A}$) are stood out with a smaller mean and σ for the differences than those derived with the red wavelength (5550−6800 $\mathring{A}$). We also noted that going to redder wavelengths then 6000 $\mathring{A}$ the accuracy of our radial velocity calculations affected by telluric absorption. In addition, moving on to the near-infrared wavelengths confront us with the fringes, where night sky emission lines are bright and where the CCD becomes more transparent to light. Correcting the scientific data for fringing is a demanding procedure, and even a small failure during this procedure effects the following continuum normalization, consequently the accuracy of radial velocities and atmospheric parameters. Due to all these reasons, we decided to continue our survey's observations with the blue wavelength range.

5.5 Data Reduction

The data reduction was carried out in a homogeneous way with the *IRAF* [1] as following steps.

[1] Image Reduction and Analysis Facility

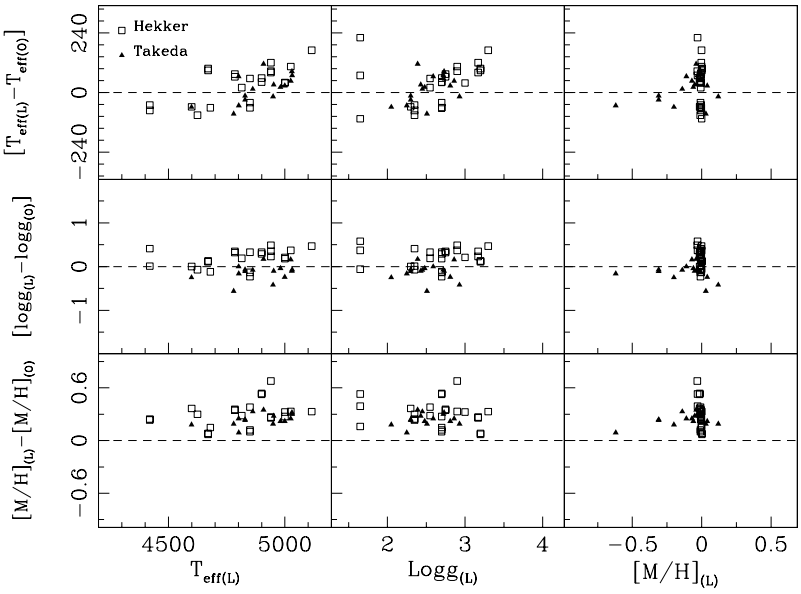

Figure 5.4: Comparison between the atmospheric parameters derived by chi^2 method and given by Hekker & Melendez (2007), Takeda et al. (2008) for the blue wavelength range.

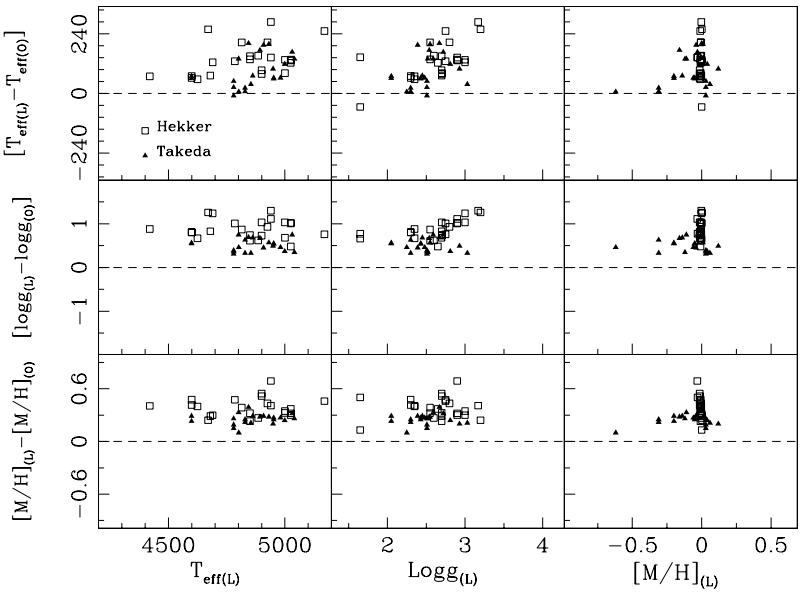

Figure 5.5: Comparison between the atmospheric parameters derived by χ^2 method and given by Hekker & Melendez (2007), Takeda et al. (2008) for the red wavelength range.

- **Bias Subtraction:** The bias is the most basic type of of CCD calibration image which is a zero-point offset. Zero-point offset corrects the counts from a given pixel where one gets zero counts when there is no light falling on it. A bias image is obtained by resetting the charges on the CCD and immediately reading it out with the shutter closed. The bias level depends on a number of parameters, including the temperature, the electronics and power level changes that can vary over the night. At each night of the observations we obtained 6 bias frames. To subtract the bias, first a median bias is created from all the 6 bias frames, than it is subtracted from each pixel in all other images.

- **Trimming The Images:** After the bias subtraction, as a routine procedure, we checked the scientific images with the *DS9* display package. This check could be necessary for detecting the columns and rows which are of little scientific interest or are effected by edge-reading problems. During our data reduction process, we trimmed the first 5, last 8 columns and the first 10, last 10 rows from all the scientific images, calibration lamps and the flat field images in the same way.

- **Flat Field Correction:** A CCD shows pixel to pixel quantum efficiency (QE) variations and non-uniform illumination. The flat field images used to correct for this systematic effect. The quality of the flats must be very high to correct the QE and illumination variations in the science images; the S/N ratios of the flats must be greater than the science images, that usually requires more than one flat image to be obtained. At each night of the observations we obtained six dome flats. These flat field images were obtained by pointing the telescope at a homogeneously illuminated surface in the dome. For flat field correction, a median flat field image created from all six flat field images with equal exposure times. Then we normalized each row of this flat to a mean value of 1.000 and finally the scientific spectrum divided by the normalized flat.

- **Aperture extraction:** Identification of the aperture and subtraction of sky background made by the *appall* task. This essentially refers to the process of correcting for the night sky background and reducing the spectrum to one dimension. Each pixel in this final 1D spectrum is then the total 'instrumental' flux of the object corrected for any sky emission. It is very important to determine the aperture accurately and select the background sky region that is subtracted. For not produce non-optimal extractions, *apall* task applied separately to each scientific images with checking the resulted 1D spectrum. For the background fitting a *Legendre* function with an order of 2 used and a median subtraction applied. To trace the fitting function a *spline3* function with an order of 1 used.

5.5.1 Wavelength Calibration

As we mentioned in previous sections, we obtained two comparison spectrum of Fe−Ar lamp for each target star during our observations in order to provide reference points for the precise determination of wavelength. At the beginning, we revised and build up the Fe−Ar calibration lamp spectrum to be able to give a convincing demonstration that the wavelengths were calibrated correctly. Furthermore, an improved calibration of the wavelength scale will allow a more precise determination of the stellar radial velocities. Thus, we re-identified all the lines in the Fe−Ar calibration lamp spectrum and we selected the most reliable and un-saturated lines among all the lines in our wavelength range for calibration. The pruning of the Fe−Ar calibration lamp was made as following steps:

- Re-identify all the lines in the Fe-Ar calibration lamp spectrum at the 4760−6000 $\AA$ using the *Identification List of Lines in Stellar Spectra* (C.E Moore,1957), *NIST Atomic Spectra Database* [2], and *The Atomic Line List v2.04* [3].
- Check the distribution of the residuals after the dispersion curve fitting with IRAF *Identify* task.
- Eliminate the lines which are not correlated well with the preliminary distribution of the dispersion curve and re-apply the *Identify* task to check the new distribution of the residuals. And proceed till the best solution achieved.

The final Fe−Ar calibration lamp spectra and the lines used for wavelength calibration can be seen on Fig. 5.6 and Fig. 5.7. The wavelength and the contributor of used lines for wavelength calibration is given in Tab. 5.6

Before applying the wavelength calibration, two calibration lamp spectrums were combined to an average calibration lamp spectrum. Then *apall* task applied to trace the same path in the direction of dispersion as their related scientific spectrum has. To calibrate the pixel scale of scientific spectra into a wavelength scale via identifying the lines in calibration lamp spectrum, the task *Identify* used. Lines in the calibration lamp spectrum of each scientific spectra identified via our pruned line list. In every step of the identification process the fitted dispersion curve to the identified lines checked. A *Legendre* function with an order of 5 used for this curve. The *Re-Identify* task has never been used during our identification process. Line identification applied one by one to the each calibration lamp spectrum of the scientific images. And finally, the *Dispcor* task used to apply the wavelength calibration.

5.5.2 Continuum Normalization

Continuum normalization is a convenient way of eliminating several factors that are poorly known including the wavelength sensitivity of the instrument and broad-band extinction

[2]National Institute of Standards and Technology http://physics.nist.gov/PhysRefData/ADS/
[3]http://www.pa.uky.edu/ peter/atomic/

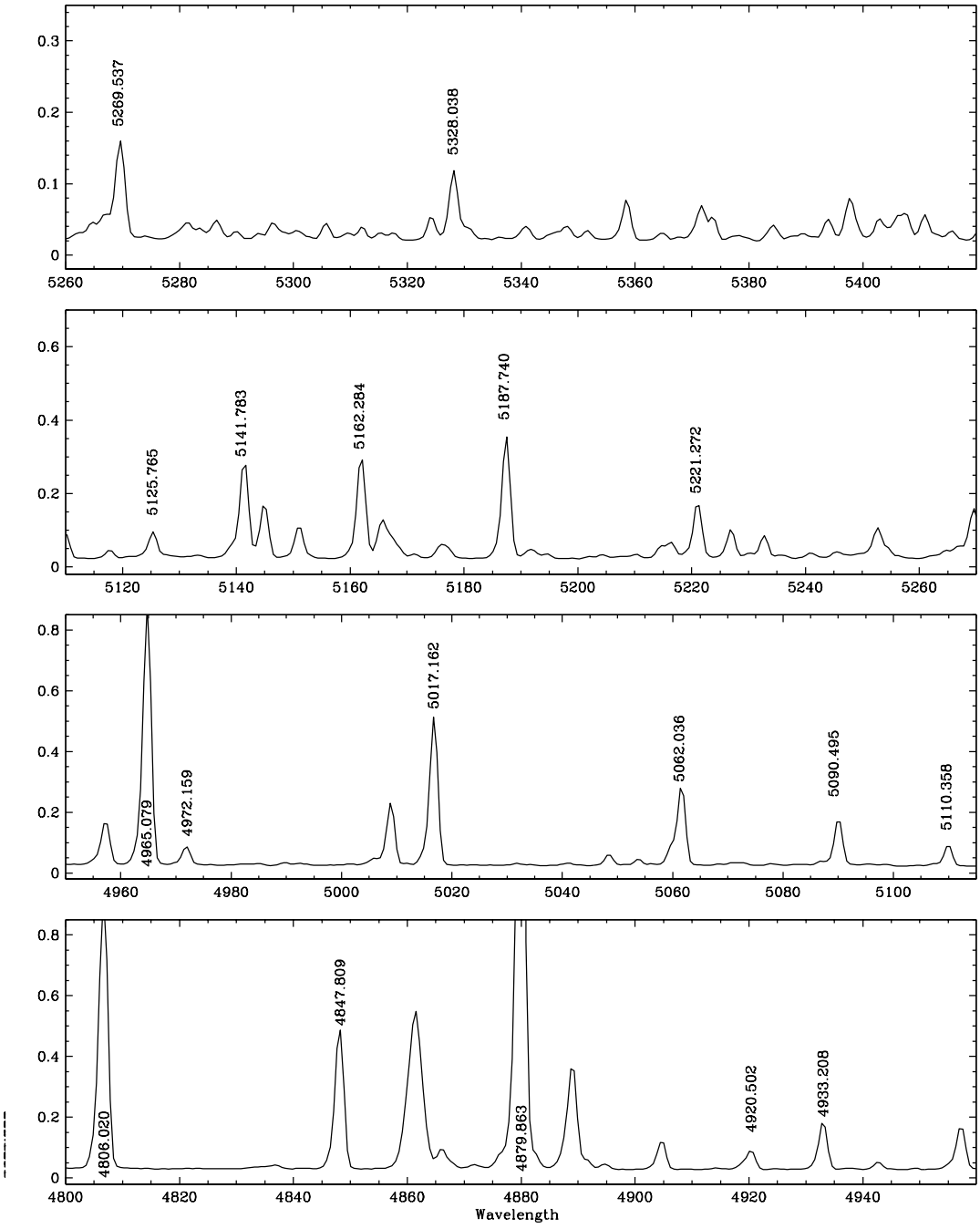

Figure 5.6: Re-identified Fe-Ar Calibration Lamp

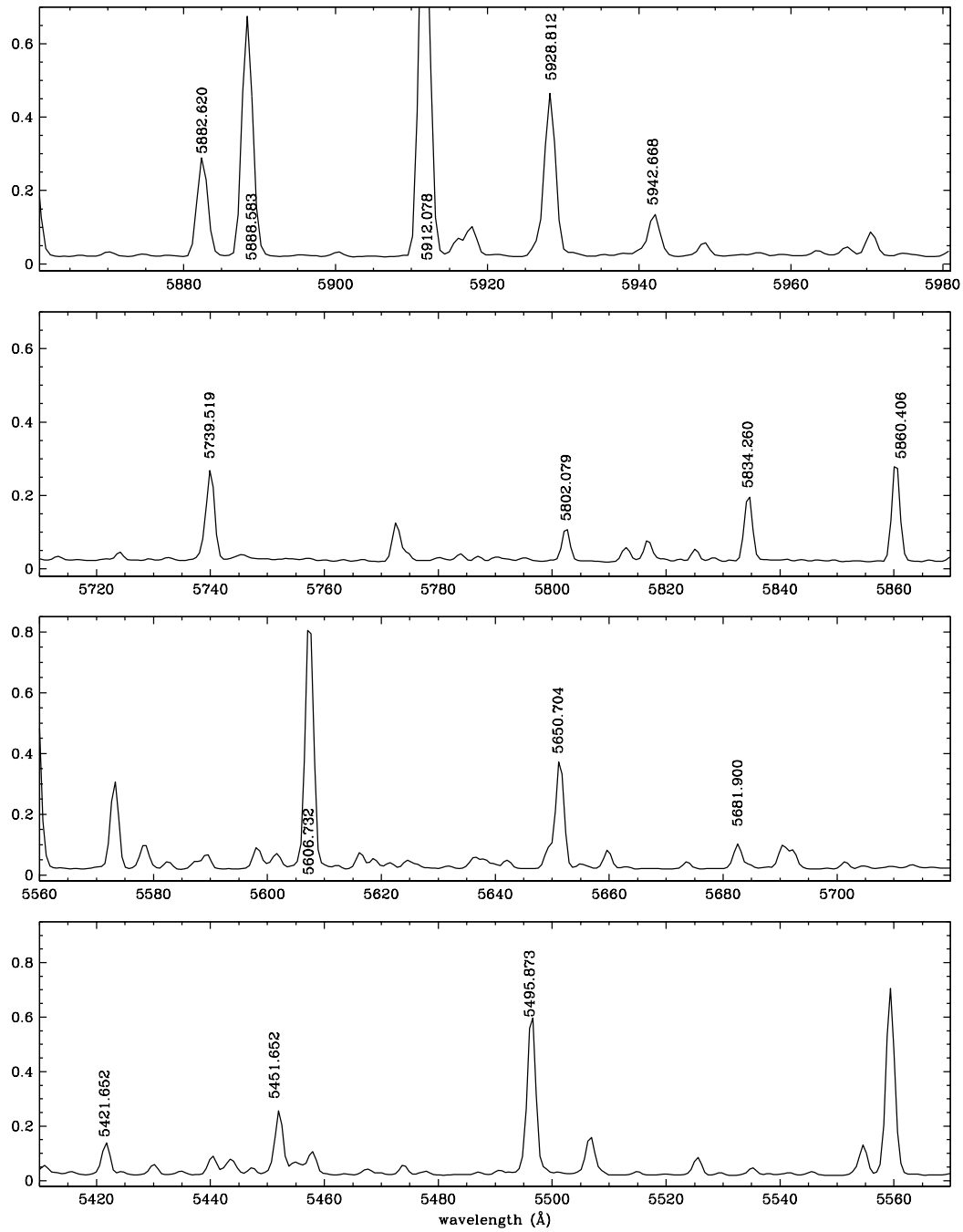

Figure 5.7: Re-identified Fe-Ar Calibration Lamp Continued

in the Earth's atmosphere and the interstellar medium. Continuum normalization is an important step in our analysis, since both the radial velocity determination via cross-correlation and the atmospheric parameter determination via chi^2 depend critically on the accuracy of continuum normalization and effected from different levels and asymmetries of it. To ensure the highest quality and homogeneity, the continuum normalization of all spectra was carried out manually in three steps for each spectra.

First, alot of care was put in training the operator's human responso. For this, we used the synthetic spectral library of Munari et al. (2005). About 100 synthetic spectra similar to the Red Clump were selected from the synthetic library. We multiplied them by randomly selected, arbitrary instrumental response and then we added a noise to simulate the $S/N \geq 200$ which caracterized our observed spectra. The resulting spectra were than manually normalized with the IRAF task *Continuum*. Then, the result of the normalization was compared to the originally computed as continuum normalized synthetic spectrum. The comparison revealed where improvements in the human decision were necessary. On average, the best results were obtained with a *Legendre* fitting poliynomial of 5^{th} order with a high-rejection treshold of 0.0 and a low-rejection treshold of $1.35 \times \sigma$.

The second step was to apply such human experiance to the observed speactra, normalizing them manually and individually with the same IRAF *Continuum* task and adopting the same fitting polynomials and associated parameters. In some cases, a different degree of polinomial, or masking some portion of the spectrum, or changes of other parameters were necessary for an optimal result, depending on the specific characteristic of individual observed spectra.

The third and final step was applied to be able to achive the best solution from the χ^2 fit. We automatically renormalized the whole Munari et al. (2005) synthetic spectral library with the same IRAF task *Contimuum* and associated parameters, so they would be in the same parameter space as the observed ones. Before running the χ^2 fit, a final refinement was applied by imposting that the geometric mean of each spectrum matched that of the observed ones. this forced the mean level of continuum in the obserevd and synthetic spectra to coincide.

5.5.3 Heliocentric Correction

Finally the scientific images corrected for the doppler shift due to the motion of the Earth. For this correction, first the heliocentric velocity for each target star is calculated with the IRAF task *rvcorrect* and then doppler shift of heliocentric velocity removed from each scientific spectrum with the IRAF task *dopcor*.

Table 5.5: The comparison of mean and sigma values for atmospheric parameters derived from chi^2 performed at both blue and red wavelength ranges.

For the blue wavelength range		
$< T_{eff} > = 35.80$	$\sigma = 83.70$	
$< logg > = 0.20$	$\sigma = 0.22$	Hekker & Melendez (2007)
$< [M/H] > = 0.30$	$\sigma = 0.15$	
$< T_{eff} >= 14.92$	$\sigma = 56.99$	
$< logg > = -0.12$	$\sigma = 0.19$	Takeda et al. (2008)
$< [M/H] > = 0.24$	$\sigma = 0.07$	
For the red wavelength range		
$< T_{eff} > = 130.21$	$\sigma = 73.55$	
$< logg > = 0.87$	$\sigma = 0.22$	Hekker & Melendez (2007)
$< [M/H] > = 0.38$	$\sigma = 0.11$	
$< T_{eff} >= 89.13$	$\sigma = 67.12$	
$< logg > = 0.51$	$\sigma = 0.14$	Takeda et al. (2008)
$< [M/H] > = 0.25$	$\sigma = 0.07$	

Table 5.6: Re-Identified Lines For Fe−Ar Calibration Lamp

Wavelength Å	Main Contributor
4764.8646	ArI
4806.0205	ArI
4847.8095	ArI
4879.8635	ArI
4920.5018	FeI
4933.2091	ArI
4965.0795	ArI
4972.1597	ArI
5017.1628	ArI
5062.0371	ArI
5090.4951	ArII
5110.3849	FeI
5125.7654	ArI
5141.7827	ArI
5162.2846	ArI
5187.7462	ArI
5221.2710	ArI
5269.5366	FeI
5328.0376	FeI
5421.3517	ArI
5451.6520	ArI
5495.8738	ArI
5606.7330	ArI
5650.7043	ArI
5681.9001	ArI
5739.5196	ArI
5802.0798	ArI
5834.2633	ArI
5860.3103	ArI
5882.6242	ArI
5888.5841	ArI
5912.0853	ArI
5928.8130	ArI
5942.6686	ArI
5987.3000	ArI
5998.9987	ArI

Chapter 6

Measuring Radial Velocities

One of the main goal of our survey is to derive the accurate radial velocities for our target stars. Accurate radial velocity determination is a challenging task. Accuracy implies absence of (significant) systematic errors. In the present context, the most important sources of systematic errors are either instrumental, flexures and slit illumination effects, or related to properties of the observed stellar spectrum itself, what is often referred to as 'template mismatch' effects. With the development of highly stable spectrometers it is not unreasonable to assume that instrumental effects can be eliminated to a high degree, and therefore should not be the limiting factor in a well-designed instrument operated under controlled conditions. Systematic errors from template mismatch are an entirely different matter: they seem to be inevitable unless the object and template spectra are almost identical, resulting from the same source, or at least the same stellar type, and recorded with the same instrument. For instance, it is generally recognized that the use of a single template for different spectral types is likely to cause a sliding and largely unknown zero-point error with additional systematics caused by differences in stellar rotation, gravity and chemical composition.

6.1 Cross-Correlation Technique

The application of cross-correlation methods to measure the velocity shifts has become a standard technique with the advent of massive spectroscopic surveys. Recently, the Radial Velocity Experiment (RAVE) used a standard cross-correlation procedure (Steinmetz et al. (2006)) to derive the radial velocities of programme stars. The plans for ESA's upcoming mission the Gaia satellite is to use cross-correlatin techniques for measuring the radial velocities for $\sim 10^8$ stars (Katz et al. (Katz et al., 2004)).

For our analyses, we used the *IRAF* cross-correlation technique *FXCOR* to determine the radial velocities. In simple terms, cross-correlation is a measure of similarity of two spectra. After the suitable calibrations, continuum normalization and heliocentric correction, *FXCOR* procedure searches for a correlation between the stellar spectrum and

a template to find the maximum of the cross-correlation function (CCF) that gives the differential velocity of the stellar spectrum with respect to a template. *FXCOR* calculates this differential velocity between the object and template as:

$$\Delta RV = RV_{Object} - RV_{Template} \tag{6.1}$$

The template can be a real stellar spectrum, such as a star of similar spectral type to the object of the study. Or alternatively, can be a synthetic stellar spectrum, such as from a model atmosphere, or from a synthetic spectral library. Measuring radial velocities with cross-correlation technique relies on the availability of accurate stellar templates to correlate with the observed spectra. Generally, using templates from a synthetic spectral library with the same resolving power and in the same wavelength interval is a widespread procedure for spectroscopic surveys that covers stars from entire color-magnitude diagram (i.e. Gaia and RAVE). Our survey resist on just the red clump stars which are scattered in a narrow spectral type with a fixed luminosity class. Instead of using templates from a synthetic spectral library, we decided to use real stellar spectrum with well known radial velocities (IAU radial velocity standard stars) and same spectral type as the target stars. Hereby, we also minimized the systematic errors due to the instrument (flexures and slit illuminations) or during the observations since both since spectrum and the template is taken in the same night, with the same instrument under the same conditions.

The *FXCOR* procedure can be performed in two ways; as in a pixel space correlation if the input spectra is not dispersion corrected or the *pixcor* parameter is set on and as in a wavelength space for dispersion corrected spectra. The *pixcor* option is useful when pixel shifts are the desired output for comparing the velocities calculated from the pixel shifts and those derived with the *FXCOR*. During our analyses, we kept the *pixcor* flag as off but we also checked the pixel shifts to calculate corresponding radial velocities to compare with the derived values directly from *FXCOR*.

Once the correlation computed, *FXCOR* applies a fit to the maximum peak with defined parameters (*rebin*, *osample*, *rsample*, *continuum*, *filter*, *width*, *height* and *peak*) and calculates a relative velocity between the object and the template spectrum. Determining the center of the cross correlation peak is the key step in measuring a relative shift or velocity between the object and template. A suitable fitting function and a sample width must be specified. In *FXCOR*, there are five methods for determining the correlation peak (Gaussian, Parabola, Lorentzian, Center1d and Sinc). For our calculations we used a Gaussian fit with a width defined approximately to the full width.

To perform a reliable fit, a convenient background determination is also required. To fix the background of the Gaussian fit, we set the *background* parameter graphically after the fit applied with *FXCOR* to the desired background level and re-do the fit for all the targets spectra.

If the image headers are complete (i.e. sufficient information for heliocentric velocity corrections) and dispersion correction made, *FXCOR* computes three velocities, a relative (VREL), an observed (VOBS) and a heliocentric velocity (VHELIO) for each object.

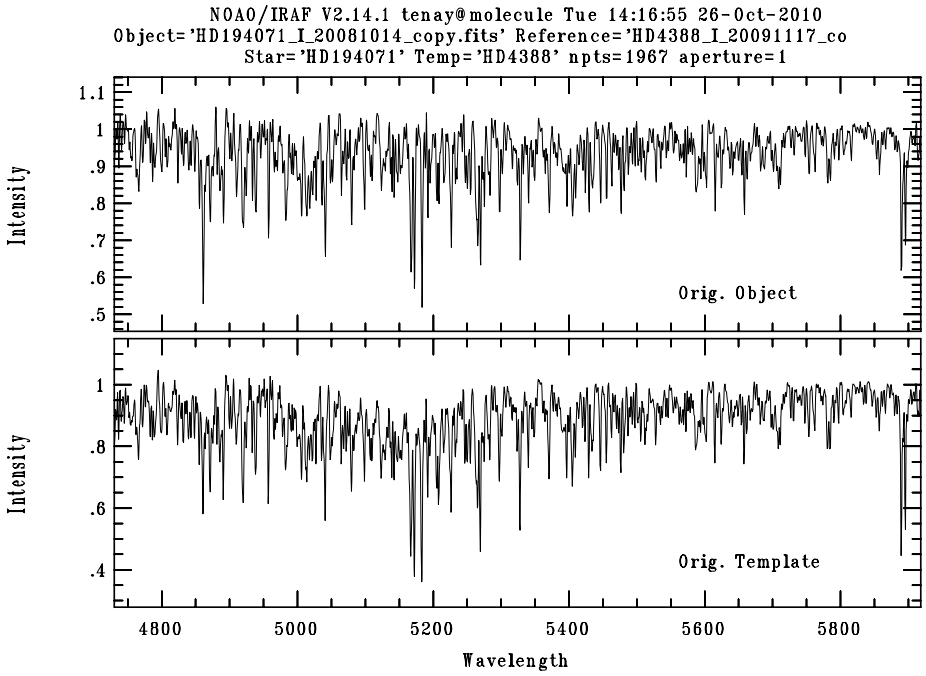

Figure 6.1: Gaussian fit to the maximum of the correlation peak

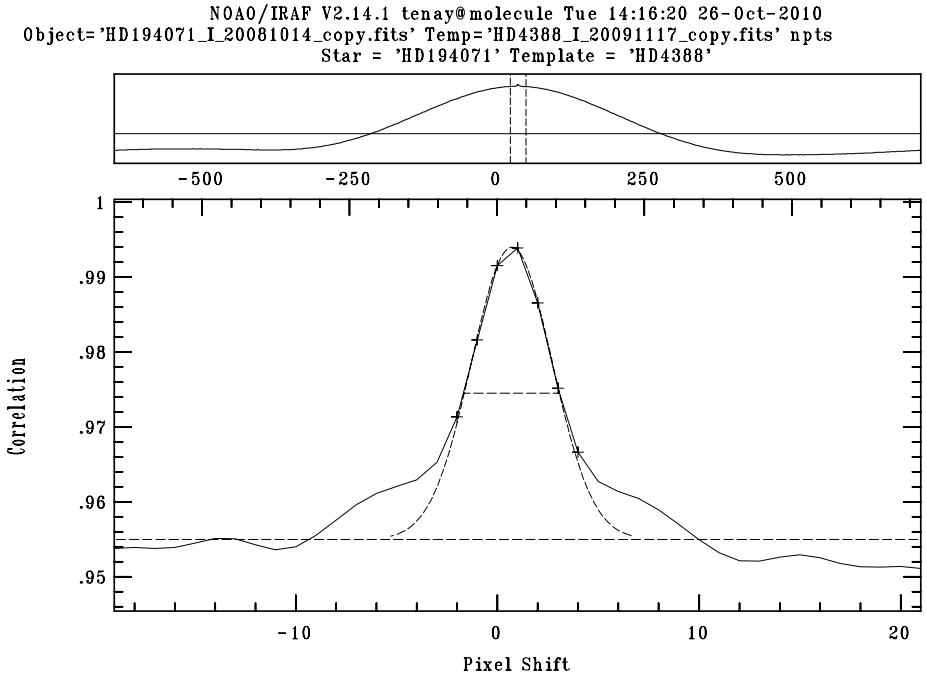

Figure 6.2: Object and the template spectra for cross-correlation at *FXCOR*

During our calculations we applied the heliocentric correction and completed our image headers with *keywpars* task, we were able to determine all three velocities for each object-template couple.

6.2 Accuracy Tests With IAU Radial Velocity Standards

Given the many problems related to the determination of accurate radial velocity, we spent a long time on accuracy tests of our radial velocity calculations. As a starting point we decided to use stars with well known parameters, like IAU Radial Velocity Standard stars.

We dedicated the first 5 nights of our observing campaign to observed IAU radial velocity standard stars. From *Astronomical Almanac of 2009* we choose 15 IAU standards with the similar spectral types and luminosity class to our target stars and we also choose IAU standards with different spectral types and different luminosity classes to investigate the effects of tamplete missmaches. We obtained multi-epoch observations (4-8 observations for each star) of 15 IAU radial velocity standard stars during those 4 nights. Our aim was to get to know the instrument, it's performance and to carry out the tests on the accuracy of radial velocity determination. A list of observed IAU standard stars is given in Tab. 6.1.

The data reduced with basic steps described before. Before performing the *FXCOR*, the blue and the red ends of the spectra ($\sim$ 20 $\mathring{A}$) are rejected with the *IRAF* task *scopy*. The reason for this is to avoid the poorer focus, lower resolving power, and lower quality of the wavelength calibrartion at the edges of the spectral interval while also brought all the targets spectra in the same wavelength interval. This procedure then applied for the all the other target stars that are observed during the campaign.

For test purposes, after reducing and re-scaling the effective wavelength interval, the spectra of IAU standards are divided 4 equal wavelength range (4746-5054 $\mathring{A}$, 5054-5362 $\mathring{A}$, 5362-5670 $\mathring{A}$, 5670-5978 $\mathring{A}$) with *scopy* task. Fig. 6.3 shows the 4 wavelength intervals.

Then for the stars that are observed at least 2 times or more during the 5 nights, we performed *FXCOR* using one observation of the IAU standard as object and the other onservation of the same IAU standard star as template in the following order:

- I.range, I.exposure - I.range,II.exposure
- II.range,I.exposure-II.range,II.exposure
- III.range,I.exposure- III.range,II.exposure
- IV.range,I.exposure-IV.range,IIexposure.

From this test one has to expect not a significant change on derived radial velocity values for each range, since it is the spectra of the same star just taken on another night. Such

Table 6.1: List of Observed Radial Velocity Standard Stars

Object Name	Right Ascension h m s	Declination ° ′ ″	V mag.	Spectral Type	RV km/s
HD4388	00 46 57.8	+31 00 12	7.34	K3 III	−28.3
HD62509	07 45 53.8	+28 00 09	1.14	K0 III	+3.3
HD132737	15 00 17.0	+27 07 23	7.64	K0 III	−24.1
HD136202	15 19 48.0	+01 43 48	5.06	F8 III	+53.5
HD144579	16 05 16.5	+39 07 52	6.66	G8 IV	−60.0
HD145001	16 08 30.3	+17 01 20	5.00	G5 III	−9.5
HD154417	17 05 45.9	+00 41 21	6.01	F8 IV	−17.4
HD161096	17 43 56.5	+04 33 50	2.77	K2 III	−12.0
HD182572	19 25 25.4	+11 57 55	5.16	G7 IV	−100.5
HD187691	19 51 28.9	+10 26 24	5.11	F8 V	+0.1
HD194071	20 23 01.3	+28 16 38	7.80	G8 III	−9.8
HD212943	22 28 20.4	+04 44 37	4.79	K0 III	+54.3
HD213014	22 28 39.2	+17 18 43	7.45	G9 III	−39.7
HD213947	22 35 03.4	+26 38 51	6.88	K2	+16.7
BD283402	19 35 23.1	+29 06 31	8.88	F7 V	−36.6

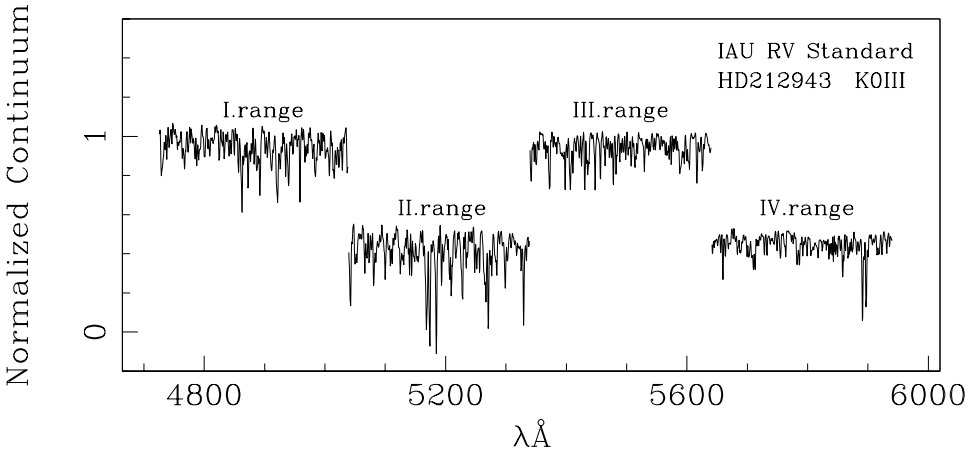

Figure 6.3: Radial velocity determination tests on IAU RV standards

that, when we calculated the mean ΔRV from 4 different range for each object-template couple of analysed 15 IAU standard, we found $+/-$ 0.742 kms^{-1} as the average difference. In the perfect case this difference ought to be 0 kms^{-1}. The systematic errors during the observation (different positions on the slit for the same object at different nights, the differences of weather conditions and guiding between different nights for the same object) and the systematic errors introduced during the data reduction procedure (the quality of the wavelength calibration, the different levels of continuum normalization) can be effected to produce this difference.

After this test, we continued our analysis for the same 15 IAU standard stars by using the all effective wavelength interval. We took one star as object and used the other 14 IAU standards as templates during the cross-correlation procedure. The mean error of radial velocity is $+/-2.18$ kms^{-1}. But in some cases the errors are slightly higher $+/-4.202$ kms^{-1} than this value which we thought could have been caused from systematic errors during the observations.

In Fig. 8.3, we plot the radial velocities of 15 IAU radial velocity standard star given by the *Astronomical Almanac of 2009* versus the mean radial velocity of stars derived by cross correlating against all the other srandards observed at the same night.

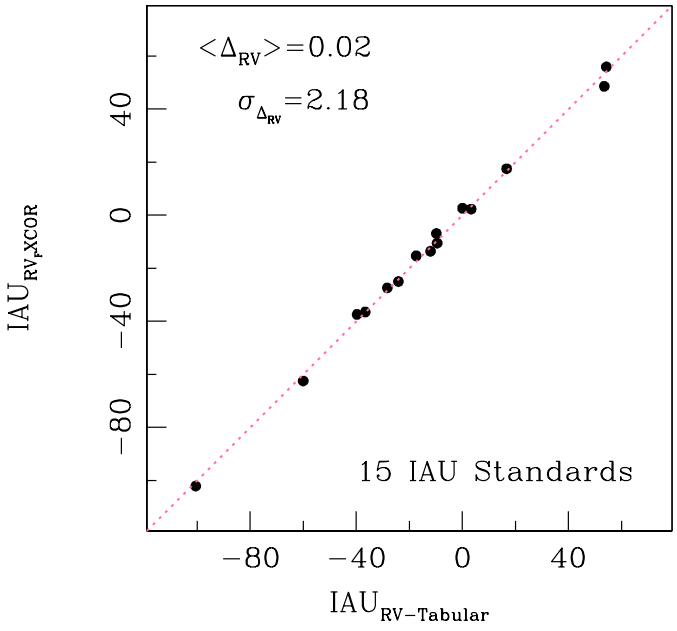

Figure 6.4: Comparison of radial velocities for IAU RV standards

Table 6.2: The radial velocities for 15 IAU standard stars derived from cross-correlation and their literature values.

Star	Spc.T.	Literature		Cross-Correlation	
		V_{rad}	σ_{Vrad}	V_{rad}	σ_{Vrad}
HD4388	K3 III	−28.3	0.6	−27.4	2.1
HD62509	K0 III	03.3	0.1	02.3	2.7
HD132737	K0 III	−24.1	0.3	−25.0	1.6
HD136202	F8 III	53.5	0.2	48.6	1.9
HD144579	G8 IV	−60.0	0.3	−62.5	0.8
HD145001	G5 III	−09.5	0.2	−10.5	1.2
HD154417	F8 IV	−17.4	0.3	−15.3	1.5
HD161096	K2 III	−12.0	0.1	−13.6	0.9
HD182572	G7 IV	−100.5	0.5	−102.1	1.1
HD187691	F8 V	00.1	0.3	02.6	0.8
HD194071	G8 III	−09.8	0.1	−06.9	0.5
HD212943	K0 III	54.3	0.3	55.9	1.9
HD213014	G9 III	−39.7	0.0	−37.4	1.7
HD213947	K2	16.7	0.3	17.5	1.3
BD283402	F7 V	−36.6	0.5	−36.5	0.4

6.3 Extended Tests On Radial Velocities

We started our survey 2 years ago and we aimed to observed Red Clump stars that are not observed by other spectroscopic surveys of Red Clumps. Thus, we checked our stars from the *SIMBAD* database to see if they are still not having valid entiries in other surveys. During this check we found 11 stars that were already existing in Pulkovo Compilation of Radial Velocities (Gontcharov, 2006).

Pulkovo catalog is a compilation of radial velocities for 35495 Hipparcos stars that have been observed by several authors in the literature and/or from the Hipparcos input catalog. Since it is a compilation of different measuring methods on radial velocities of stars, the velocities in this catalog have been calibrated to a weighted mean absolute radial velocity scale to be able to homogenise the different methods used to derive radial velocities from different sources.

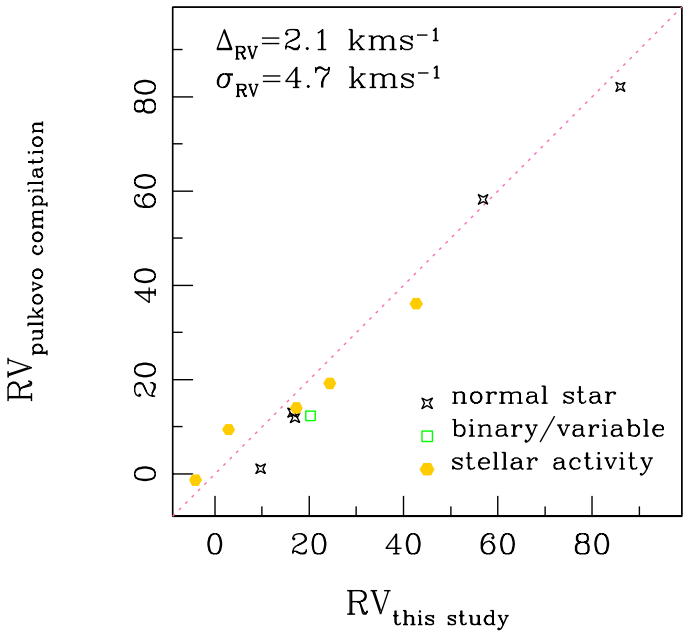

Figure 6.5: Comparison of radial velocities with Pulkovo compilation of radial velocities

In Fig. 6.5, we plot the radial velocities of this 11 stars derived from our cross correlation technique agains their radial velocities in Pulkovo Compilation. During our search we also found 5 stars that have been noticed by The Vienna-KPNO search for Doppler-imaging candidate stars (Strassmeier et al., 2000) with having entries in Catalog of Stellar Activity, that are shown in Fig. 6.5 with orange dots.

Surprisingly, we also found a star which has an entry in SB9: the ninth catalogue of spectroscopic binary orbits (Pourbaix et al., 2004), shown in Fig. 6.5 with a green square. While building our input catalog we tried to avoid stars with binary or variability flags in Hipparcos catalog. But this star has not been noted as possible binary in Hipparcos

catalog, because of it's period (P=407 days) and most likely it's eccentricity (e=0.41). Unfortunately, during our survey we just obtained one observation for this star. With a second epoch observation, which is saperated from the first one by more than 6 months, maybe we would have been able to detect it from the radial velocity variability. For the future, we would like to monitor this star during one year with minimum 4 different epoch observations.

Chapter 7

Atmospheric Parameter Determonation

Apart from accurate radial velocity determination, our survey aimed to derive also the atmospheric parameters (T_{eff}, $\log g$ and $[M/H]$) for target stars via χ^2 fitting. In this chapter we discussed the χ^2 method that we used and the accuracy tests on the derived atmospheric parameters.

7.1 χ^2 Technique

We have derived the atmospheric parameters ($T_{\rm eff}$, $\log g$, [M/H]) of program stars via χ^2 fitting to the synthetic spectral library of Munari et al. (2005), the same used in the analysis of RAVE spectra, which is based on the atmospheric models of Castelli & Kurucz (2003). We used the library in its solar scaled ($[\alpha/Fe] = 0$) and 2 kms^{-1} micro-turbulence version, computed at a resolving power of 5500, the same of our observed spectra.

The program that we used for the χ^2 fitting technique (by Massimo Fiorucci,2008) looks for the best matching template from the synthetic spectral library to the observed spectra and applies an interpolation to derive the grid parameters corresponding to the minimum of the χ^2 function.

The interface for the χ^2 program is shown in Fig. 7.1. This interface was developed for being able to control and check every step of the calculation, derived parameters and the final fit. The atmospheric parameters determination procedure with χ^2 technique was made with the following steps:

- The normalized final observed spectrum is used against the templates from the synthetic spectral library to find the atmospheric parameters from the best fit. As it can be seen in Fig. 7.1, we searched and selected the observed spectra that will be process in χ^2 fitting (top left in the figure, input data), than with *Graph* button we

plotted the spectrum for a final check of the continuum normalization (see Fig. 7.2).

- The radial velocity values for each observed spectrum derived from cross-correlation is used to set the step interval to search for the minumum of the χ^2 function. According to the input observed spectrum's radial velocity, we gave an velocity interval that χ^2 fit will be applied (In Fig. 7.1 and Fig. 7.2, Vrad min - Vrad max).

- After preparing everything, we run the χ^2 fit to find the best synthetic spectrum that will fit the observed one. And controlled the final derived parameters that are automatically written in the terminal window (see Fig. 7.3).

- At the end, we plotted the best fitting synthetic spectrum to check the quality and validity of the solution (Fig. 7.3, in red : the observed spectrum and in blue : the best fitting synthetic spectrum).

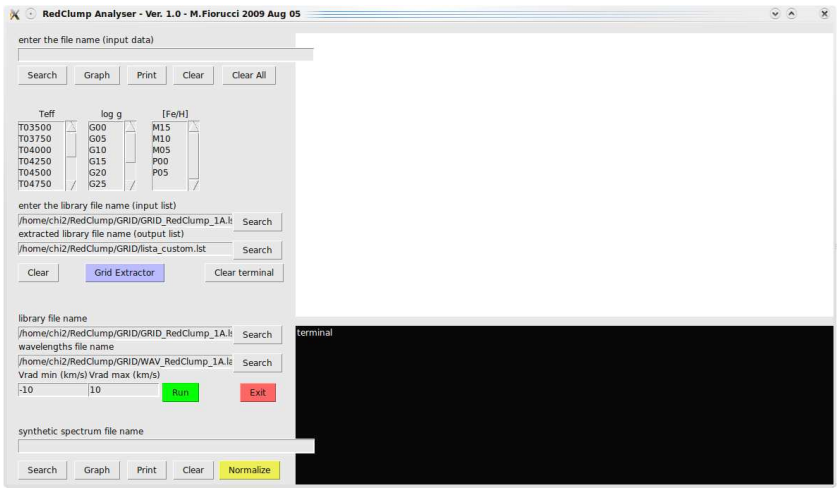

Figure 7.1: The χ^2 interface that we used for atmospheric parameter calculation

7.1.1 The Synthetic spectral Library

During our analyses we used synthetic spectral library of Munari et al. (Munari et al., 2005). This library based on Kurucz's atmosphere models and computed using the SYNTHE code by Kurucz. The microturbulent velocity is 2 kms^{-1} throughout the grid and some grids are also available for different microturbulent velocities (1 and 4 kms^{-1}) which is a very small part of the grid and only for α-enhanced mixtures [α/Fe = +0.4]. Different sets of rotational velocities (V_{rot}) available through the parameter space : as hotter stars are faster rotators, their synthetic spectra are calculated with V_{rot} up to 500 kms^{-1} while for cooler stars V_{rot} is limited to values lower than 100 kms^{-1}.

The library of synthetic spectra covers all the HR diagram. The effective temperatures ranges from 47500 K down to the lower limit of 3500 K. Surface gravities ranges from

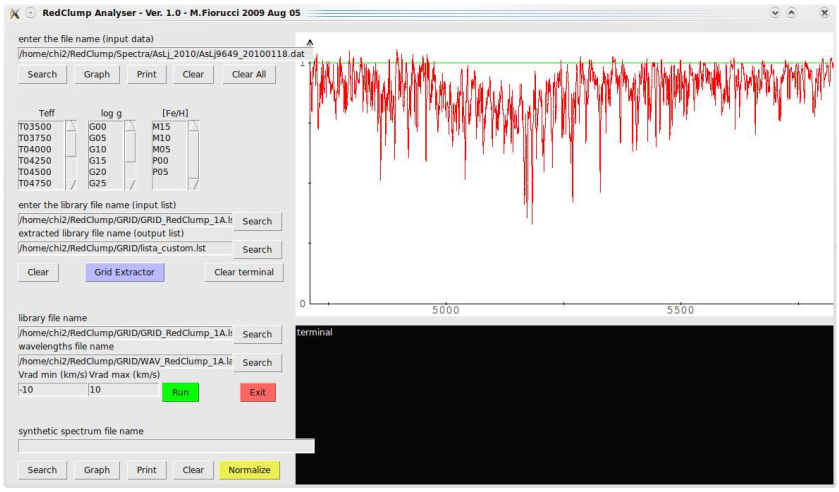

Figure 7.2: The χ^2 interface that we used for atmospheric parameter calculation

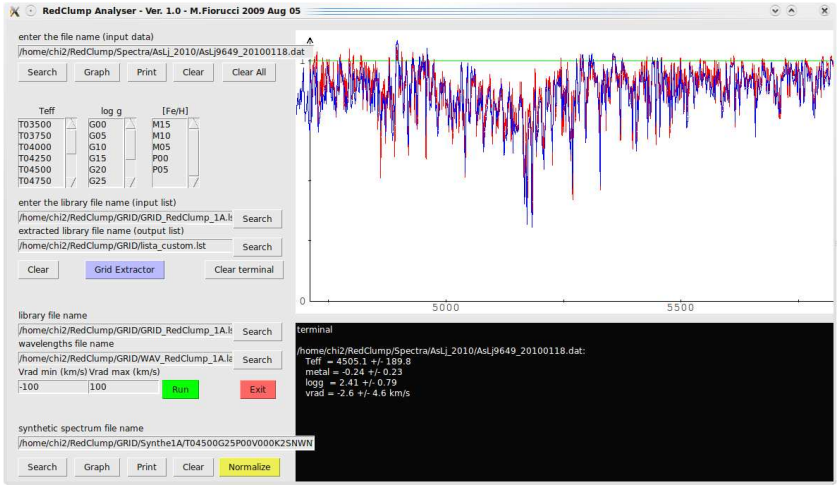

Figure 7.3: The χ^2 interface that we used for atmospheric parameter calculation

+0.0 to +5.0 in steps of 0.5 dex and the metallicities from −2.5 to +0.5 with 0.5 steps. In addition the grids considers the variations of alpha elements with α/Fe = +0.0 and α/Fe = +0.4. The synthetic spectra covers the 2500−10500 $\mathring{A}$ spectral range and available at two resolving powers, R_p = 20000 and R_p = 5500. Among those properties, we used α/Fe = +0.0, V_{rot} = 2kms^{-1} and R_p = 5500 set.

This library is the one of the main source of best-matching template for cross-correlation and *chi*^{2} techniques. Because, first of all the rotational velocity is not fixed by temperature and gravity to a common value for the associated spectral type in this synthetic library, which is very realistic approach while dealing with peculiarly rotating stars. Second, the predicted lines are excluded from the computations. This becomes a very important and preferable characteristic of this library when the spectroscopic applications are the main goal (Munari et al., 2005).

7.1.2 The χ^2 Methods

We carried out extensive preliminary tests to investigate what should be the optimal extension and positioning of the wavelength interval, within the recorded wavelength range, over which to carry out the χ^2 fitting. As we also did to select and test the best wavelength interval to perform our observations that we discussed in Chapter 3, Section 3.4.

The necessity of such a preliminary assessment was dictated by some considerations. On one side, the wider the wavelength range subject to χ^2 is, the larger the amount of information brought in. On the other hand, the wider the wavelength range is, the less trustworthy the continuum normalization is. In addition, while the χ^2 fitting is mainly driven by the countless amount of weak, optically thin lines forming over a large extension of the stellar atmosphere, the classical line-by-line analysis (usually based on ionization and excitation balance of Fe lines) works on a selected and limited sample of lines that could probe a less extended depth of the stellar atmosphere. Furthermore, while χ^2 fitting is a far more efficient method with large volumes of data and/or with medium (or low) resolution spectra that are packed with blended lines, it is also far more sensitive than the line-by-line method to the completeness of the line lists used to compute the synthetic spectra (see for example, the huge number of *new* FeII lines introduced by Castelli and Kurucz (2010)).

For these, and other subtler reasons, we extensively explored what could be gained by considering only a sub-interval of the whole wavelength range covered by our spectra.

To this aim, we used the spectra of 88 RC stars that we selected from the extensive surveys of RC stars by Hekker & Melendez (2007), Takeda et al. (2008) and Soubiran & Girard (Soubiran and Girard, 2005), and that we re-observed with our instrument with the same S/N of the spectra collected for the target stars (see next sect. for details). The atmospheric analysis in those papers was carried out on high-resolution spectra with the line-by-line method.

We considered wavelengths intervals progressively shorter (in steps of 100 $\mathring{A}$), and let

them to reposition freely within the recorded wavelength range of our spectra. For each spectrum, for each length and position of the wavelength interval, we compared the result of derived atmospheric parameters from our χ^2 fitting with those from the line-by-line methods.

The results of the comparison showed that the accuracy of the χ^2 fitting does not improve by considering wavelength intervals wider than 300 $\mathring{A}$.

Next, we explored what would be the best positioning of a $\Delta\lambda = 300$ $\mathring{A}$ interval that would minimize the difference between the results of χ^2 fitting and literature data based on the line-by-line method. We found that the interval 4761−5061 $\mathring{A}$ delivered the best results (in the sense of null off-set and lower dispersion) for $T_{\rm eff}$, 5614−5918 $\mathring{A}$ for $\log g$, and 5012−5312 $\mathring{A}$ for [M/H]. These intervals were consequently adopted for the analysis of target stars.

7.2 Accuracy Tests With Red Clump Stars In the Literature

Nowadays in the literature there are many available catalogs of Red Clump stars from high-resolution spectroscopic surveys based on atmospheric parameters derived with classical line-by-line methods (as we mentioned in the previous section). Among them we re-observed 48 Red Clump stars from Hekker & Melendez (Tab. 7.1), 34 Red clump stars from Takeda et al. (Tab. 7.3) and 6 Red Clump stars from Soubiran et al. (Tab. 7.5) with the same adopted instrumental set-up for our target stars.

The mean differences between derived atmospheric parameters and their literature values are :

- For Hekker & Melendez :
  $< (T_{our} - T_{HM}) >= -11K(\sigma = 83K)$,
  $< (logg_{our} - logg_{MH}) >= -0.06dex(\sigma = 0.38dex)$,
  $< ([M/H]_{our} - [M/H]_{HM}) >= 0.04dex(\sigma = 0.18)$.

- For Takeda et al. :
  $< (T_{our} - T_T) >= 28K(\sigma = 61K)$,
  $< (logg_{our} - logg_T) >= 0.28dex(\sigma = 0.23dex)$,
  $< ([M/H]_{our} - [M/H]_T) >= -0.10dex(\sigma = 0.11)$.

- For Soubiran et al. :
  $< (T_{our} - T_S) >= -84K(\sigma = 181K)$,
  $< (logg_{our} - logg_S) >= -0.18dex(\sigma = 0.20dex)$,
  $< ([M/H]_{our} - [M/H]_S) >= -0.01dex(\sigma = 0.21)$.

Table 7.1: Comparison between the atmospheric parameters obtained with χ^2 method and derived by Hekker and Melendez (2007)

HD	Spc.T.	Hekker & Melendez			χ^2		
		$T_{\rm eff}$ (K)	log$g$ (dex)	[M/H] (dex)	$T_{\rm eff}$ (K)	log$g$ (dex)	[M/H] (dex)
3807	K0 III	4625	2.30	−0.44	4526	1.80	−0.46
4627	G8 III	4599	2.05	−0.25	4664	2.42	−0.04
6186	K0 III	4829	2.30	−0.24	4845	2.55	−0.50
7087	K0 III	4850	2.55	−0.15	4915	2.74	−0.12
7318	K0 III	4815	2.55	−0.11	4832	2.50	−0.08
10380	K3 III	4300	2.20	−0.27	4410	1.99	0.00
10761	K0 III	4952	2.43	0.00	5020	2.84	−0.24
12929	K2 III	4600	2.70	−0.13	4480	2.28	−0.04
13468	G9 III	4893	2.54	−0.12	4919	2.64	−0.42
15176	K1 III	4650	2.85	−0.07	4531	2.45	−0.08
18449	K2 III	4500	2.65	−0.07	4314	2.30	0.00
19656	K1 III	4600	2.30	−0.18	4726	2.46	0.00
21755	G8 III	5012	2.45	−0.03	5064	2.95	−0.38
26162	K2 III	4800	2.90	0.06	4728	2.76	0.00
27382	K1 III	4550	2.50	−0.32	4371	1.67	−0.46
27697	G8 III	4984	2.64	0.09	4955	3.06	0.00
28100	G8 III	5011	2.54	−0.24	5039	3.17	−0.33
28305	K0 III	4883	2.57	0.05	4976	3.06	0.00
34559	G8 III	4998	2.74	0.03	5084	3.20	−0.12
38527	G8 III	5046	2.77	−0.07	5122	3.29	−0.29
42398	K0 III	4650	2.40	−0.15	4646	2.51	−0.17
48433	K1 III	4550	2.20	−0.20	4528	2.15	0.00
52556	K1 III	4700	2.65	−0.08	4627	2.55	0.00
54079	K0 III	4450	2.10	−0.42	4415	1.85	−0.38

Table 7.2: Table 7.1: Continues

HD	Spc.T.	Hekker & Melendez			χ^2		
		$T_{\rm eff}$ (K)	log$g$ (dex)	[M/H] (dex)	$T_{\rm eff}$ (K)	log$g$ (dex)	[M/H] (dex)
54719	K2 III	4500	2.55	0.14	4512	2.35	0.29
55751	K0 III	4550	2.10	−0.11	4619	2.28	0.00
59686	K2 III	4650	2.75	0.15	4706	2.51	0.00
65695	K2 III	4470	2.45	−0.15	4436	2.14	0.00
69994	K1 III	4650	2.60	−0.07	4518	2.38	−0.08
73471	K2 III	4550	2.40	0.05	4603	2.66	0.29
184406	K3 III	4520	2.41	0.04	4356	2.36	0.06
190327	K0 III	4850	2.70	−0.15	4832	2.83	0.18
192944	G8 III	5000	2.70	−0.10	5040	2.84	−0.08
194317	K3 III	4435	2.70	0.04	4338	1.73	0.12
197139	K2 III	4485	2.40	−0.08	4439	1.87	−0.04
197912	K0 III	4940	3.17	−0.03	4844	2.77	−0.06
197989	K0 III	4785	2.27	−0.11	4791	2.25	−0.04
199253	K0 III	4625	2.35	−0.19	4520	2.49	0.00
209761	K2 III	4420	2.35	−0.08	4371	1.68	0.00
210762	K0 III	4185	1.65	0.00	4181	1.98	0.42
211073	K3 III	4360	2.45	−0.09	4434	2.51	0.31
211388	K3 III	4260	2.15	0.01	4173	1.48	0.46
213119	K5 III	3910	1.59	−0.48	3955	1.34	−0.37
214995	K0 III	4680	2.70	−0.04	4540	2.25	0.13
219615	G7 III	4830	2.57	−0.54	4958	2.26	−0.50
220954	K1 III	4775	2.95	0.02	4779	2.51	0.00
223252	G8 III	5031	2.72	−0.08	5041	2.88	−0.12
224533	G9 III	5030	2.72	−0.02	5084	2.87	−0.04

Table 7.3: Comparison between the atmospheric parameters obtained with χ^2 method and derived by Takeda et al. (2008)

HD	Spc.T.	Takeda			χ^2		
		$T_{\rm eff}$ (K)	log$g$ (dex)	[M/H] (dex)	$T_{\rm eff}$ (K)	log$g$ (dex)	[M/H] (dex)
448	G9 III	4780	2.51	0.03	4731	2.63	0.04
587	K1 III	4893	3.08	−0.09	4791	3.25	−0.34
4627	G8 III	4599	2.05	−0.20	4664	2.42	−0.04
6186	K0 III	4829	2.30	−0.31	4845	2.55	−0.50
7087	K0 III	4850	2.55	−0.04	4915	2.74	−0.12
10348	K0 III	4931	2.55	0.01	4895	3.06	0.00
10761	K0 III	4952	2.43	−0.05	5020	2.84	−0.24
10975	K0 III	4866	2.47	−0.17	4874	2.68	−0.25
11037	G9 III	4862	2.45	−0.14	4957	2.51	−0.37
13468	G9 III	4893	2.54	−0.16	4919	2.64	−0.42
19525	G9 III	4801	2.59	−0.11	4813	2.69	−0.08
21755	G8 III	5012	2.45	−0.13	5064	2.95	−0.38
23526	G9 III	4837	2.50	−0.15	4852	2.63	−0.42
27371	G8 III	4923	2.57	0.10	4985	3.21	0.00
27697	G8 III	4984	2.64	0.12	4955	3.06	0.00
28100	G8 III	5011	2.54	−0.08	5039	3.17	−0.33
28305	K0 III	4883	2.57	0.13	4976	3.05	0.00
34559	G8 III	4998	2.74	0.00	5084	3.20	−0.12
35410	K0 III	4809	2.58	−0.33	4794	2.94	−0.50
38527	G8 III	5046	2.77	−0.11	5122	3.29	−0.29

Table 7.4: Table 7.3: Continues

HD	Spc.T.	Takeda			χ^2		
		$T_{\rm eff}$ (K)	log$g$ (dex)	[M/H] (dex)	$T_{\rm eff}$ (K)	log$g$ (dex)	[M/H] (dex)
39007	G8 III	4994	2.69	0.08	5148	3.30	0.00
39019	G9 III	4964	2.91	0.19	5017	3.25	0.00
45415	G9 III	4753	2.39	−0.12	4852	2.73	−0.25
51814	G8 III	4846	2.23	−0.02	4753	2.79	−0.04
192787	K0 III	5025	2.86	−0.07	4958	2.76	−0.12
192944	G8 III	4981	2.48	−0.06	5040	2.84	−0.08
209396	K0 III	4999	2.81	0.04	5041	3.17	−0.04
210434	K0 III	4949	2.93	0.12	4919	3.13	0.08
210702	K1 III	4967	3.19	0.01	4974	3.21	−0.12
217264	K1 III	4946	2.80	0.12	4978	3.27	0.00
219615	G7 III	4802	2.25	−0.62	4958	2.26	−0.50
223252	G8 III	5031	2.72	−0.03	5041	2.88	−0.12
224533	G9 III	5030	2.72	−0.01	5084	2.87	−0.04

Table 7.5: Comparison between the atmospheric parameters obtained with χ^2 method and derived by C.Soubiran and P.Girardi (2005)

HD	Spc.T.	Soubiran & Girardi			χ^2		
		$T_{\rm eff}$ (K)	log$g$ (dex)	[M/H] (dex)	$T_{\rm eff}$ (K)	log$g$ (dex)	[M/H] (dex)
188512	G8 IV	5106	3.54	−0.15	5073	3.42	−0.46
190404	K1 V	4963	3.90	−0.82	4539	3.44	−0.66
191026	K0 IV	5050	3.49	−0.10	4979	3.40	−0.25
197964	K1 IV	4813	3.03	0.17	4773	3.13	0.46
212943	K0 III	4586	2.81	−0.34	4521	2.50	−0.29
219615	G7 III	4830	2.57	−0.42	4958	2.26	−0.50

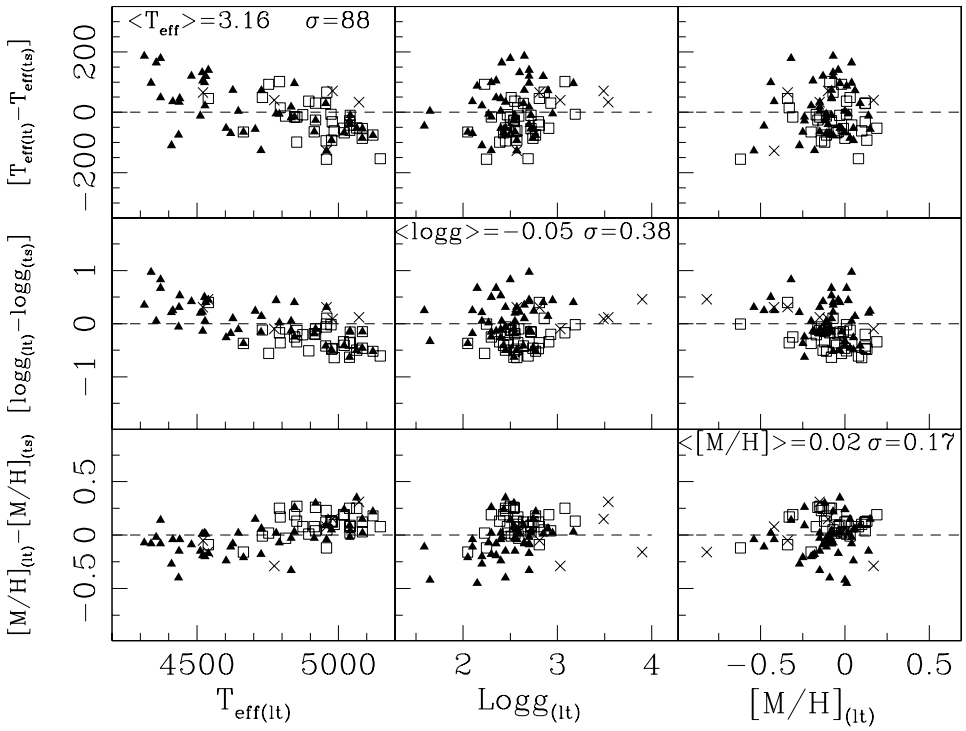

Figure 7.4: Differences between atmospheric parameters derived from χ^2 and those from literature. Empty squares are the data from Takeda et al. (2008),filled triangles Hekker & Melendez (1997) and the crosses from Soubiran (2005).

Combining the results from the three different catalog, for observed 88 Red Clump stars in common we found that,

$$< (T_{our} - T_{lit}) >= +3K(\sigma = 88K) \tag{7.1}$$

$$< (Logg_{our} - Logg_{lit}) >= -0.05dex(\sigma = 0.38dex) \tag{7.2}$$

$$< [M/H]_{our} - [M/H]_{lit} >= +0.02dex(\sigma = 0.17dex) \tag{7.3}$$

7.3 Comparison With Photometric Temperatures

Theoretically, it is also possible to derive effective temperatures using the photometric colors. Most frequently, they are used as starting pointnin the iterative analysis based on the ionization and extiction equilibrium of FeI and FeII lines from high-resolution spectroscopy (Gratton et al. 2006; Fulbright et al. 2007), but sometimes they are directly imported as fixed values into abundance analysis (McWilliam 1990; Honda et al. 2004).

In literature, the calibrations of colors to derive effective temperatures of stars for different photometric systems are available and widely used. Since all of the program stars were observed by 2MASS and Tycho, we have additional photometric information which can be used to calculate effective temperatures and compare them with the ones derived from our χ^2 analysis.

Following the relation given by Ramirez & Melendez (2005), we calculated effective temperatures with color calibrations for different photometric systems, such as ($B_{Tycho} - V_{Tycho}$), ($V_{Tycho} - K_{2Mass}$), ($J_{2Mass} - K_{2Mass}$), their coefficients are listed in Tab. 7.6 and Tab. 7.7. Also for (V − K) calibration by Mc William (1990).

In Ramirez & Melendez (2005) the T_{eff} is defined as a function of both color and metallicity (see Eq. 7.4, Eq. 7.5 and Eq. 7.6).

$$T_{eff} \;=\; \frac{5040}{\theta_{eff}} \;+\; P(X, [Fe/H]) \tag{7.4}$$

$$\theta_{eff} \;=\; a_0 \;+\; a_1 X \;+\; a_2 X^2 \;+\; a_3 X[Fe/H] + a_4[Fe/H] \;+\; a_5[Fe/H]^2 \tag{7.5}$$

$$P(X, [Fe/H]) \;=\; \sum\nolimits_i P_i X^i \tag{7.6}$$

In Fig. 7.5 and Fig. 7.6, we plotted the comparisons of temperatures derive with Ramirez & Melendez (2005) calibrations. For the temperatures derived from ($B_{Tycho} - V_{Tycho}$) calibration, the mean differences found to be smaller compare to the differences of ($V_{Tycho} - K_{2Mass}$) calibration while both two calibrations were including the [Fe/H] factor.

Thus, we also determined the effective temperatures of our target stars using the 2MASS (J−K) colors. For this, we used a calibration by Alonso et al. (1999) and the equations by

Table 7.6: Coefficients of different color calibrations for various photometric systems that used to calculate the effective temperatures.

Color (X)	Source	a_0	a_1	a_2	a_3	a_4	a_5
$(B_T - V_T)$	RM	0.5726	0.4461	−0.0324	0.0518	−0.1170	−0.0094
$(V_T - K_2)$	RM	0.4813	0.2871	−0.0203	−0.0045	0.0062	−0.0019
$(J_2 - K_2)$	AL	0.5816	0.9134	−0.1443	0.0000	0.0000	0.0000

Table 7.7: Coefficients of different color calibrations for different metallicities in $P(X, [Fe/H]$ term that used to calculate the effective temperatures.

Color (X)	Source	[Fe/H]	P_0	P_1	P_2	P_3	P_4
$(B_T - V_T)$	RM	+0.0	346.881	−1690.16	2035.65	−797.248	70.7790
		−1.0	196.416	−372.164	126.196	...	...
$(V_T - K_2)$	RM	+0.0	−37.2128	31.2900	−6.72743	...	...
		−1.0	−193.512	166.183	−33.2781	...	...

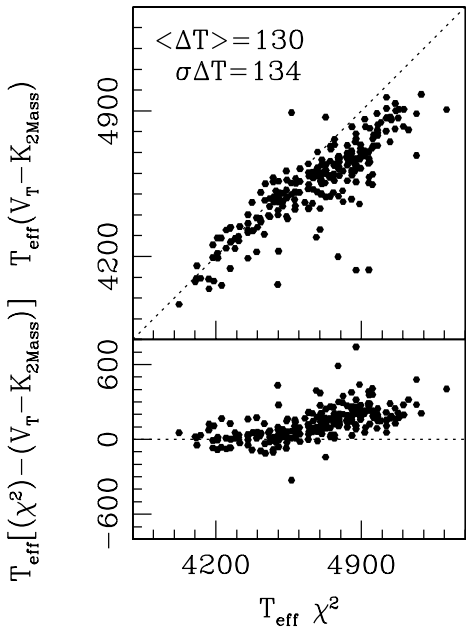

Figure 7.5: The comparison and the differences between temperatures derived from χ^2 and temperatures derived from $V_{tycho} - K_{2Mass}$

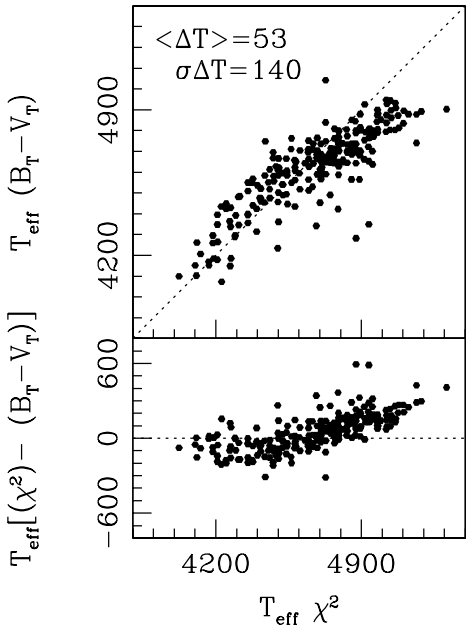

Figure 7.6: The comparison and the differences between temperatures derived from χ^2 and temperatures derived from $B_{Tycho} - V_{Tycho}$

Ramirez & Melendez (2005) to transform 2MASS colors into Alonso's TCS color system. This calibration is free from the errors on [Fe/H] since it is not including any terms of [Fe/H]. In Fig. 7.7, we plotted the comparison of temperatures derived from (J−K) calibration and χ^2. The mean differences and the sigma values are found close to the values from $(V_{Tycho} - K_{2Mass})$ calibration. To apply a nother test, we calculated the temperatures adopting Mc William calibration of $(V - K)$ (Fig. 7.8).

$$\theta_{eff} = 0.5816 + 0.9134(J - K) - 0.1443(J - K)^2 \tag{7.7}$$

$$\theta_{eff} = 5040/T_{eff} \tag{7.8}$$

$$J_{TCS} = J_{2MASS} + 0.012 - 0.063\ (J - K)_{2MASS} \tag{7.9}$$

$$H_{TCS} = H_{2MASS} - 0.013 - 0.009\ (J - K)_{2MASS} \tag{7.10}$$

$$K_{TCS} = K_{2MASS} - 0.014 + 0.027\ (J - K)_{2MASS} \tag{7.11}$$

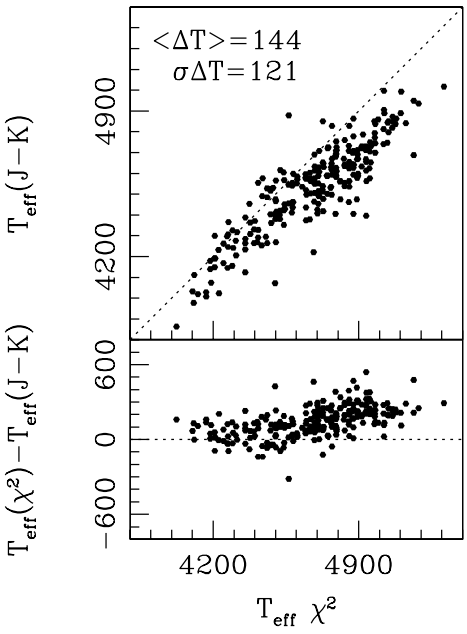

Figure 7.7: The comparison and the differences between temperatures derived from χ^2 and temperatures derived from (J-K) colors.

All photometric temperatures derived with color calibrations are systematically cooler than the spectroscopic (χ^2) temperatures. It is also a well documented result, for example, Hill et al. (2000) found a mean difference of ΔT_{eff}=150 K, while Allende Prieto et al. (2004) derived ΔT_{eff}=119 K. As discussed in detailed by Valentini & Munari (2010), photometric

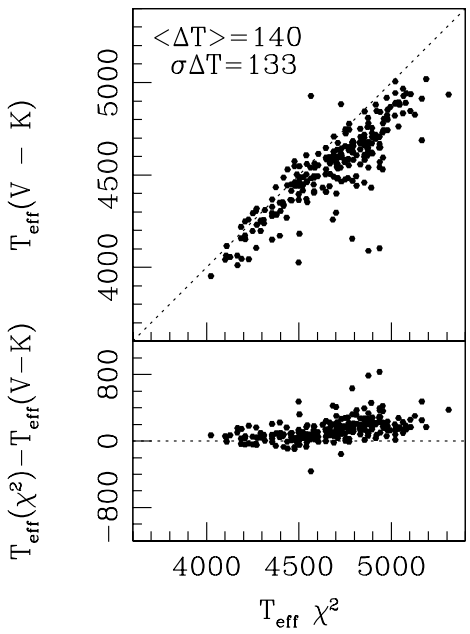

Figure 7.8: The comparison and the differences between temperatures derived from χ^2 and temperatures derived from Mc William Temperature-Color calibration.

temperatures may be useful starting points, a far more robust determination of T_{eff} is obtained by either the FeI/FeII line-by-line analysis and the χ^2 fitting.

Chapter 8

Repeated Observations Of Target Stars

We re-observed 60 target Red Clump stars at a second epoch seperated in time from the first observations by 3 months on average. The reason to go for second epoch observations of target stars are in twofold: first to check the internal consistency of our survey on derived atmospheric parameters and radial velocities, second to be able to detected binarity and variability among target Red Clump stars with monitoring the radial velocity changes in between two epoch observations.

8.1 The Final Data Quality Control From Repeated Observations

In comparison with the differences that we get on atmospheric parameter tests from the common literature stars and on the radial velocity tests from the IAU standard stars, the differences that we obtained from repeated observations were much more higher. Thus, we decided to apply a final check on the quality of the data that we obtained.

The wavelength range covered by our spectra includes four appreciably intense night-sky and city-lights lines, namely [OI] 5577.333, and HgI 5460.734, 5769.579, 5790.643 $\mathring{A}$ (Fig. 8.1). We measured them on all recorded spectra, to check the wavelength calibration from their radial velocity, and the spectrograph focusing from their sharpness. During data analysis we noticed that the spectra characterized by a FWHM ≤ 2.0 $\mathring{A}$ for the night sky lines, invariably returned the radial velocity of the night sky lines as $|RV| < 1.8$ kms^{-1}, independently from the FWHM. The spectra with FWHM > 2.0 $\mathring{A}$, showed instead a larger dispersion of the radial velocity of the night sky lines, that increased with increasing FWHM.

The same dividing threshold affected the accuracy of radial velocities and atmospheric parameters obtained for the target stars. Comparing the results of repeated observations

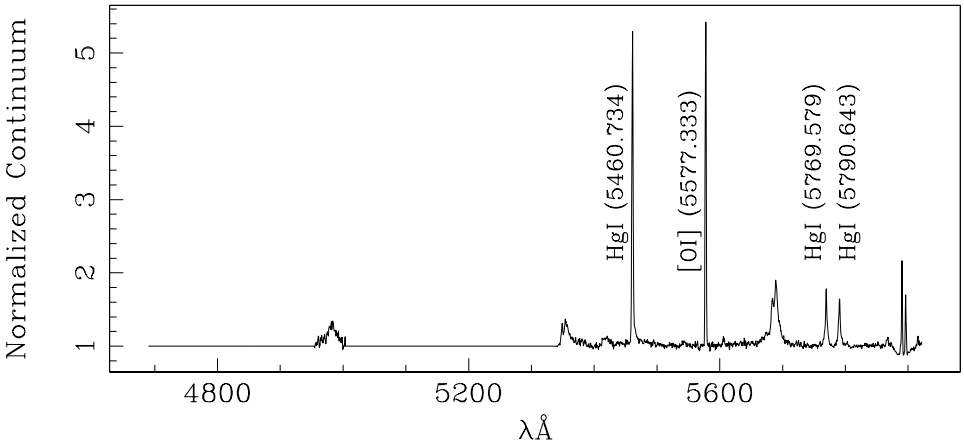

Figure 8.1: Used night sky lines for data quality control from FWHM of the lines.

of the same targets, spectra characterized by a FWHM $\leq$ 2.0 $\mathring{A}$ for the night sky lines showed a well behaving, sharp and Gaussian distribution of the differences (see Fig. 8.2), which could not be further improved by a more strict limit imposed on the FWHM of the night sky lines. Conversely, spectra with FWHM $>$ 2.0 $\mathring{A}$ showed larger dispersion in the differences between 1^{st} and 2^{nd} observations, clearly tracing a different and looser statistical population.

Being interested only in the best products our instrumentation could deliver, we ignored all observations characterized by a FWHM $>$ 2.0 $\mathring{A}$ for the night sky emission lines, and they will not be further considered in this paper. This meant reducing by 43 objects the number of targets inserted in the paper's output catalog, which in its final version includes 245 RC target stars and 60 stars with second epoch observations.

8.2 Radial Velocities

The comparison of the two epoch radial velocities for the 60 Red Clump stars are shown in Fig. 8.3, which indicates a negligible value for the mean differences between the two epochs ($< RV > = 0.09$ kms^{-1}). The standard deviation of the differences amounting to 2.6 kms^{-1}.

It is interesting to note that, none of the 60 stars in Fig. 8.3 shows a radial velocity difference between first and second epoch observations exceeding 3σ, indicating that all observed differences could be entirely ascribed to just observational uncertainties without the necessity to invoke binarity or pulsation.

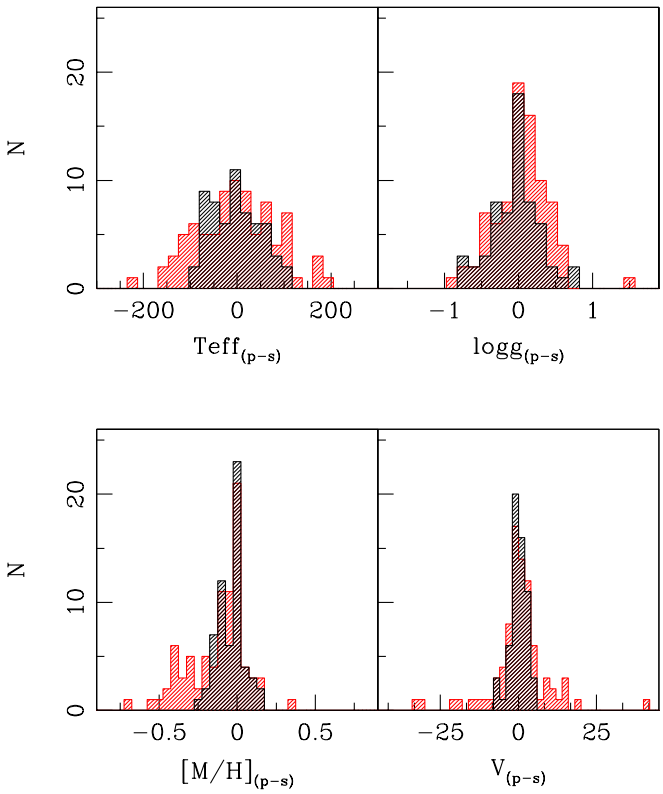

Figure 8.2: The comparison of the differences in T_{eff}, $logg$, $[M/H]$ and RV for repeated observations. The red shaded histograms are from the all repeated observations and the black shaded histograms are just for the observations with FWHM<2.0 $\mathring{A}$.

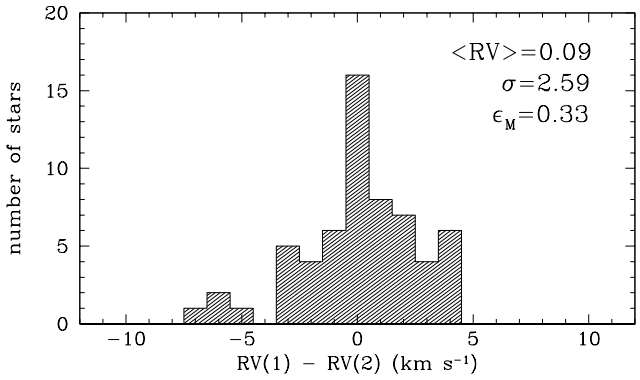

Figure 8.3: Distribution of the differences in radial velocities for repeated observations of 60 Red Clump stars.

8.3 Atmospheric Parameters

Fig. 8.4 presents the distribution of the differences in T_{eff}, $\log g$ and [M/H] between these two observations. The distribution for all the three parameters are quite sharp and characterized by $\sigma(T_{eff} = 50$ K, $\sigma(\log g) = 0.33$ dex and $\sigma([M/H]) = 0.10$.

In Fig. 8.5, we showed the differences versus T_{eff}, $\log_g$ and [M/H] of the first epoch observations. It is clear that the differences did not show a trend with the parameters.

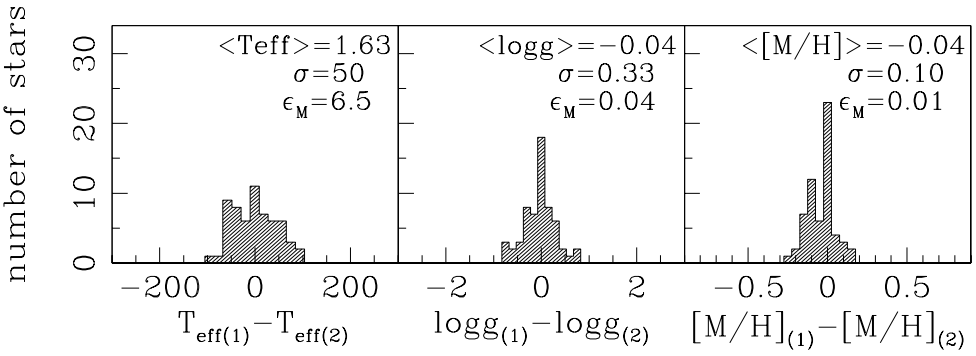

Figure 8.4: Distribution of the differences in atmospheric parameters for repeated observations of 60 Red Clump stars.

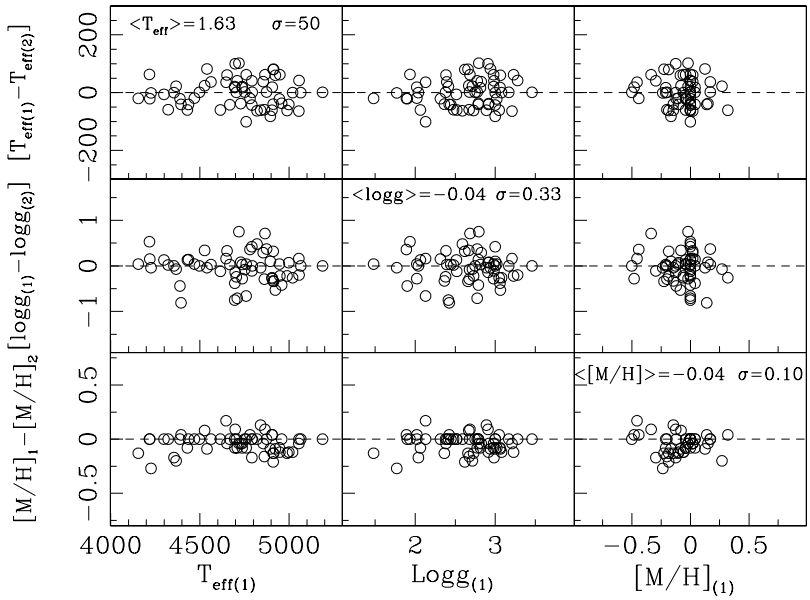

Figure 8.5: The differences in effective temperature, gravity and metallicity against same values from first epoch observations for repeated observations.

Chapter 9

Constructing The Output Catalog

In this chapter we briefly discussed the reason to derive the spectro-photometric distances and the method in the firt section. Then we explained the methodology to calculate both the Galactic (X, Y, Z) positions and the space velocity components (U, V, W) which will be discuss in more detail in the following chapters.

9.1 Determination Of Spectro-photometric Distances

Hipparcos Catalog (ESA 1997, new reduction (van Leeuwen, 2007)) contains parallaxes which are measured better than 10% for mostly bright Red clump stars. As it can be seen in Fig. 9.1, apart from 2 stars in our sample, the parallax errors are larger than $\sigma\pi/\pi > 0.2$ and reaches a maximum value of ~ 1.4.

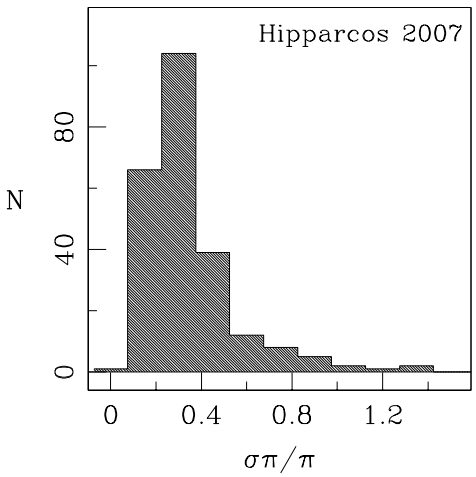

Figure 9.1: The distribution of uncertainty of distances $\sigma\pi/\pi$ from Hipparcos New Reduction (2007) for target stars.

One of the main property of red clump stars is their near-constant luminosity which makes Red Clump stars standard candles. In the literature there has been quite an effort to calibrate their observed magnitudes in to the mean absolute magnitudes. Thus we decided to derive more accurate distances for our target stars from photometry.

We used the instrinsic absolute magnitudes in Johnson V band calibrated by Keenan & Barnbaum (1999). According to MK (Morgan & Keenan, 1973) system, for late spectral type (G,K and M) giants (luminosity class III), they applied a reduction of mean Hipparcos (ESA 1997) parallaxes to derive absolute magnitudes. They defined three sub classes; class III for normal giants, class IIIa for V = 5.5 that stars might belong to asymptotic branch and class IIIb for the clump giants. The calibration of the revised luminosity classes for III and IIIb by Hipparcos parallaxes can be find in the Fig. 9.2. The mean M_V values as a function of spectral type can be find in Tab. 9.1.

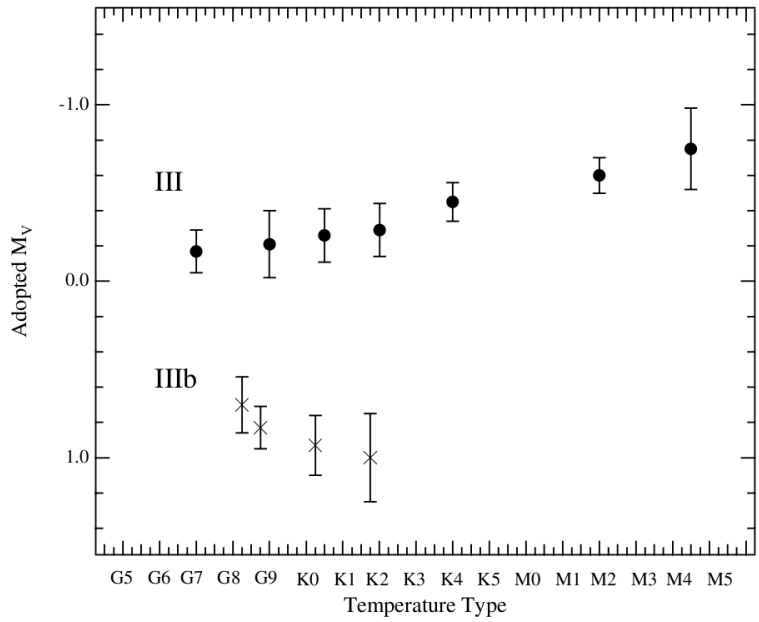

Figure 9.2: The intrinsic absolute magnitude in Johnson V band calibration by Keenan & Barnbaum (1999) as a function of spectral type for class IIIb giants.

To derive the distances, we used Tycho-2 V_T magnitudes and transformed them into Johnson V band magnitudes following the Bessel (2000) relation:

$$V - T_T = -0.09 \times (B_T - V_T) \tag{9.1}$$

According to Tab. 9.1 we applied the absolute magnitudes for each spectral type bin. Then we performed the distance modulus to derive the distances:

$$m_V - M_V = -5 + 5logd + A_V \tag{9.2}$$

Table 9.1: Mean M_V as a function of spectral type for class IIIb from Keenan & Branbaum

Spectral Type	Adopted M_V
G8 +	0.70
G9 −	0.83
K0 +	0.93
K2 −	1.00

Even if our target stars have galactic latitudes higher than $|b| \geq 25°$, we also considered extinction, A_V, while determining the distances. We adopted to different methods for derivation of extinction: the three-dimensional galactic interstellar extinction model by Arenou et al. (1992) and the three-dimensional galactic extinction model by Drimmel et al. (2003). Both models are treated that the interstellar extinction is a function of the position in the Galaxy (heliocentric distance, galactic latitude and galactic longitude). However, we prefered to use the A_V values derived with the Drimmel et al. (2003) model, cause their model, in particular, treats different assumpions depending on the stellar position (i.e Spiral Arms, Galactic Disk and beyond).

The comparison of the distances modulus derived Keenan & Barnbaum calibration with the distance modulus from Hipparcos (ESA 2007) and corresponding Tycho-2 V magnitudes is shown in Fig. 9.3 for parallaxes errors in between $10\% < \sigma_\pi < 20\ \%$ and parallax errors $\sigma_\pi > 20\%$.

It can be seen that for $10\% < \sigma_\pi < 20\%$ panel the distances modules derived photometric calibrations and the ones from Hipparcos parallaxes are in agreement but for those $\sigma_\pi > 20\%$, while the Hipparcos distances increase the photometric distances remain in the smaller values compare to the Hipparcos ones.

The error determinations for the photometric distances are made by *error propogation*. The *error propogation* (or the propogation of uncertainty) is the effect of variables' uncertainties (or errors) on the uncertainty of a function based on them. Thus, we consider all the parameter's errors that are used in Equation 9.2 and calculated the errors on the photometric distances.

We also calculated the spectro-photometric distances with the 2Mass absolute K magnitude calibration by Alves (K band calibration of the Red Clump luminosity, 2000) as seen in Equation 9.3 and 9.4. A comparison between the distances derived by absolute magnitude calibration by Keenan & Barnbaum with Alves is shown in Fig. 9.4.

$$M_K = -1.62 \pm 0.03^m \tag{9.3}$$

$$\log\ r = 0.2\ (K_s - M_K) + 1 \tag{9.4}$$

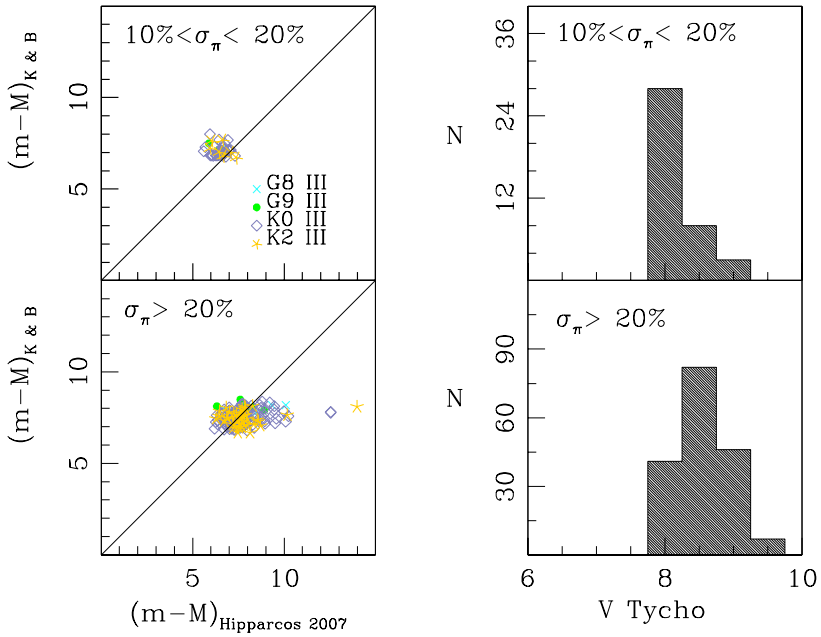

Figure 9.3: The comparison of distances from Hipparcos New Reduction (2007) and photometric distance from Keenan & Barnbaum (1999) calibrations. Each panel shows stars with different errors on Hipparcos parallaxes. Different symbol represents different spectral type. The diagonal line represents the 1:1 relation.

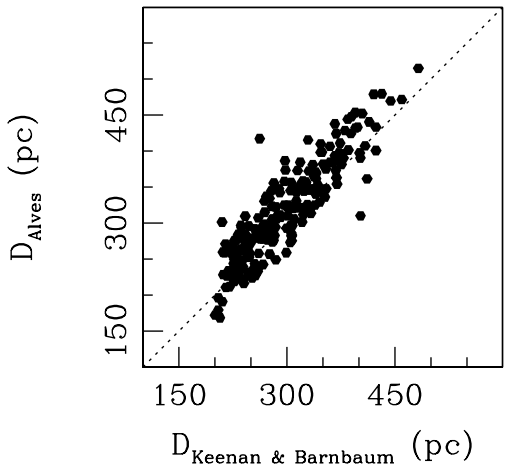

Figure 9.4: The comparison of distances derived with absolute V band magnitude calibration by Keenan & Barnbaum and with absolute K band magnitude calibration by Alves.

9.1.1 Luminosity Class II

Red Clump stars are of giants. From the first introduction of the MK system (Morgan, Keenan Kellman 1943), it was intended that luminosity class III should present the normal giant stars. When the luminosity classes were first defined, the existance of clumps was not known, but it turned that class IIIb, which was introduced with the revised MK system (Morgan Keenan 1973), neatly defines the clump.

The surface gravity of genuine Red Clump stars is confined to $\log g \geq 2$ while the surface gravity of G-K giants of luminosity class II is $1 \leq \log g \leq 2$ (Straizys 1992). In Fig. 9.5 we plotted the $\log g$-orbital energy diagram for our target stars. As shown in the lower panel of Fig. 9.5, there are 26 stars with $\log g \leq 2$ and it is shown that these stars have an orbital energy ($\sqrt{U^2+V^2}$) systematically lower than stars with $\log g \geq 2$. If the absolute magnitude calibration for those stars with $\log g \leq 2$ is revised as luminosity class II with $M_V = -2$ given by Sowell et al. (2007) we obtained the upper panel in Fig. 9.5. It is shown that now the orbital energy of stars with $\log g \leq 2$ are comparable to that of $\log g \geq 2$.

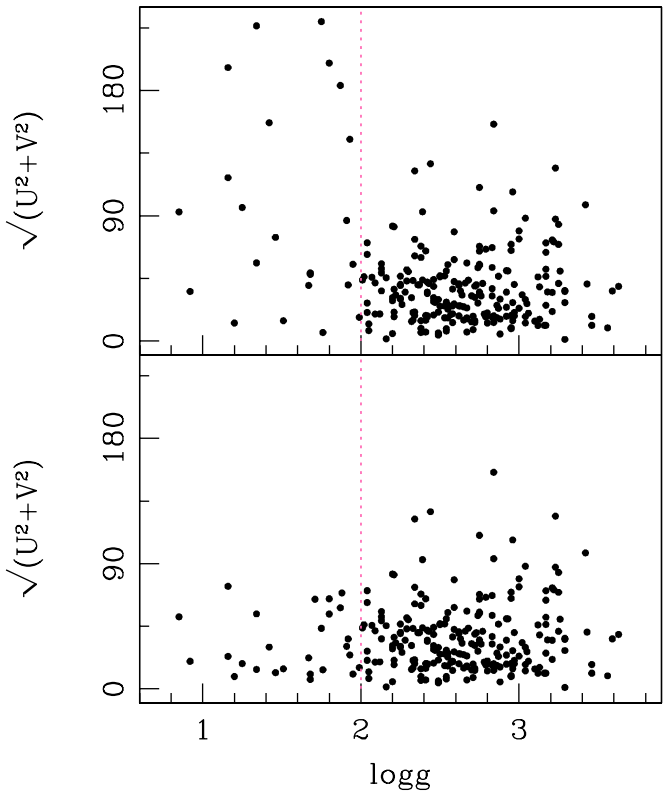

Figure 9.5: Relation between surface gravity and orbital energy. The top panel is assuming the absolute magnitude calibration for luminosity class II for stars with $\log g \leq 2$. Bottom panel is assuming the absolute magnitude calibration for luminosity class IIIb for all stars.

In the catalog associated with the thesis, the distances (and also the related quantities) for these 26 stars with $\log g \leq 2$ are derived assuming the absolute magnitude calibration of luminosity class II using $M_V = -2$ for Keenan & Barnbaum calibration. These 26 stars have entries in our final catalog but are not considered during the rest of our calculations and discussions.

9.2 Determination Of The Galactocentric Galactic Coordinates

If the distance is known, the distances and the position on the sky can be converted to the cartesian system of Galactic coordinates (X, Y, Z).

$$X = R_0 - Dcos(b)cos(l) \tag{9.5}$$

$$Y = Dcos(b)sin(l) \tag{9.6}$$

$$Z = Dsin(b) \tag{9.7}$$

Where; R_0 is the distance of the Sun from the center of the Galaxy, D is the distance of the stars, l is the Galactic longitude and b is the Galactic latitude of stars. The measurements of the Sun's distance from the Galactic center varies with the method, the best current estimate $R_0 = (8.0 \pm 0.5)kpc$ comes from the orbits of stars near the black hole that is believed to be marking the center. We do not want to affected from the uncertainties on the distance determination of Sun, thus we calculated the (X, Y, Z) positions of the sats as sun centered, not Galactic centered ($R_0 = 0\ kpc$). The distribution of the Sun centred Galactic coordinates of our target stars is shown in Fig. 9.6.

9.3 Determination Of The Galactic Velocities

The description of (U, V, W) velocities can be summarized as: U is the radially inwards velocity in the direction of Galactic Center, V is the velocity in the direction of Galactic rotation and W is the vertically upwards velocity. Figure 6.5 shows the U and V velocity component of the Sun.

If the radial velocity is known, the radial velocity, the stellar positions on the sky and the apperent motions on the sky can be converted to the Galactic velocities (U, V, W). For the calculation of (U, V, W) velocities we used the formula by Johnson & Soderblom (1987). The used input data and their uncertainties:

The Galactic coordinate system is defined by three angles. Two give the equatorial position of the North Galactic Pole, $\alpha_{NGP} \equiv 12^h49^m = 192^\circ.25$ and $\delta_{NGP} \equiv 27^\circ.4$. The third angle, $\theta_\circ \equiv 123^\circ$, is the position angle of the North Celestial Pole relative to the great

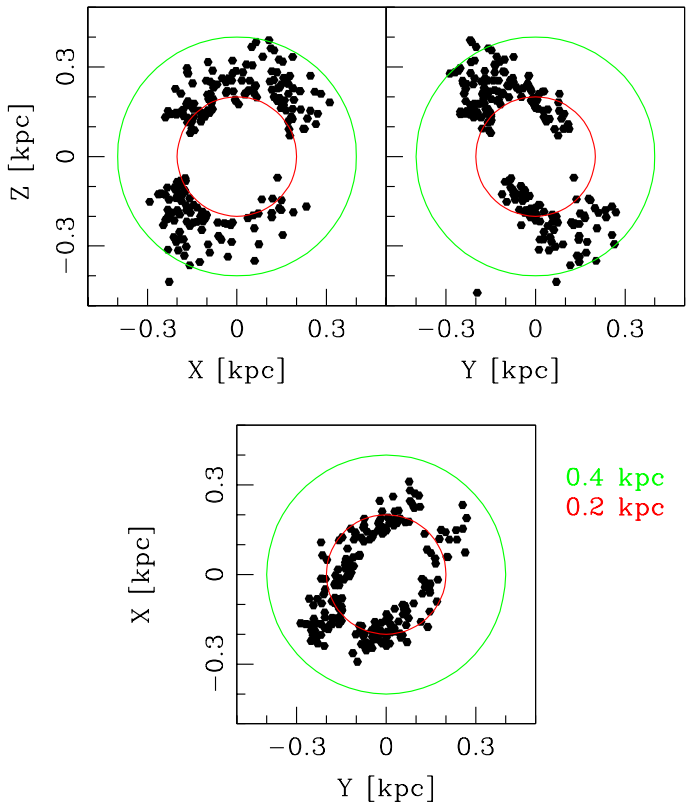

Figure 9.6: The derived Galactic positions (X, Y, Z) for target stars as seen from the vantage point of North Galactic Pole ($\alpha = 12^h49^s, \delta = 27°.4$). The red circle represents $0.2kpc$ field and the green circle represents $0.4kpc$ field.

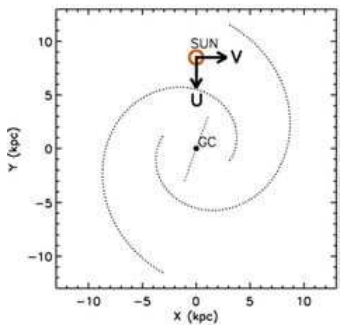

Figure 9.7: The definition of Galactic velocities (U, V, W).

Table 9.2: Used quantities and their uncertainties for (U, V, W) velocity calculation.

$\pi \pm \sigma_\pi$	the parallax in $arcsec$.
$\rho \pm \sigma_\rho$	the radial velocity in kms^{-1}.
$\mu_\alpha \pm \sigma_{\mu_\alpha}$	the proper motion in right ascension, in $arcsecyr^{-1}$.
$\mu_\delta \pm \sigma_{\mu_\delta}$	the proper motion in declination, in $arcsecyr^{-1}$.

semi-circle passing through the North Galactic Pole and zero Galactic longitude. If we want to write the transformation matrix:

$$T = \begin{bmatrix} +cos\theta_\circ & +sin\theta_\circ & 0 \\ +sin\theta_\circ & -cos\theta_\circ & 0 \\ 0 & 0 & +1 \end{bmatrix} \begin{bmatrix} -sin\delta_{NGP} & 0 & +cos\delta_{NGP} \\ 0 & -1 & 0 \\ +cos\delta_{NGP} & 0 & +sin\delta_{NGP} \end{bmatrix} \begin{bmatrix} +cos\alpha_{NGP} & +sin\alpha_{NGP} & 0 \\ +sin\alpha_{NGP} & -cos\alpha_{NGP} & 0 \\ 0 & 0 & +1 \end{bmatrix}$$

Using the above definitions of α_{NGP}, δ_{NGP} and $\theta_\circ$ we can write:

$$\mathbf{T} = \begin{bmatrix} -0.06699 & -0.87276 & -0.48354 \\ +0.49273 & -0.45035 & +0.74458 \\ -0.86760 & -0.18837 & +0.46020 \end{bmatrix}$$

The coordinate matrix can be defined as:

$$\mathbf{A} \equiv \begin{bmatrix} +cos\alpha cos\delta & -sin\alpha & -cos\alpha sin\delta \\ +sin\alpha cos\delta & +cos\alpha & -sin\alpha cos\delta \\ +sin\delta & 0 & +cos\delta \end{bmatrix} = \begin{bmatrix} cos\alpha & sin\alpha & 0 \\ sin\alpha & -cos\alpha & 0 \\ 0 & 0 & -1 \end{bmatrix} \begin{bmatrix} cos\delta & 0 & -sin\delta \\ 0 & -1 & 0 \\ -sin\delta & 0 & -cos\delta \end{bmatrix}$$

The Galactic space velocity compomenents are then can be define:

$$\begin{bmatrix} U \\ V \\ W \end{bmatrix} = \mathbf{B} \cdot \begin{bmatrix} \rho \\ k\mu_\alpha/\pi \\ k\mu_\delta/\pi \end{bmatrix}$$

where $\mathbf{B} = \mathbf{T} \cdot \mathbf{A}$ and $k = 4.74057$, the equivalent in kms^{-1} of one astronomical unit in one tropical year. For calculations, we used Tycho-2 proper motions with derived spectrophotometric distances. We also corrected the (U, V, W) velocities for the motion of the Sun

with respect to the Local standard of the Rest (LST). For our catalog, which is available in CDS archive, We used a solar motion of $(U_\odot, V_\odot, W_\odot) = (-10.00, 5.25, 7.17)$ by Dehnen & Binney (1998), in a left-handed system with U positive outward the Galactic Center to be able to provide homogenity in between our catalog and the catalog of Valentini & Munari (2010) where the $V_\odot$ value was taken as 5.25 kms^{-1}.

Lately Binney J. (2010), expressed that the value of the V component of the Sun's pecular velocity should be revised upwards from 5.2 to $\sim$ 11 kms^{-1}. Thus, in this thesis the space velocities for target stars derived using $(U_\odot, V_\odot, W_\odot) = (-10.00, 11.00, 7.17)$.

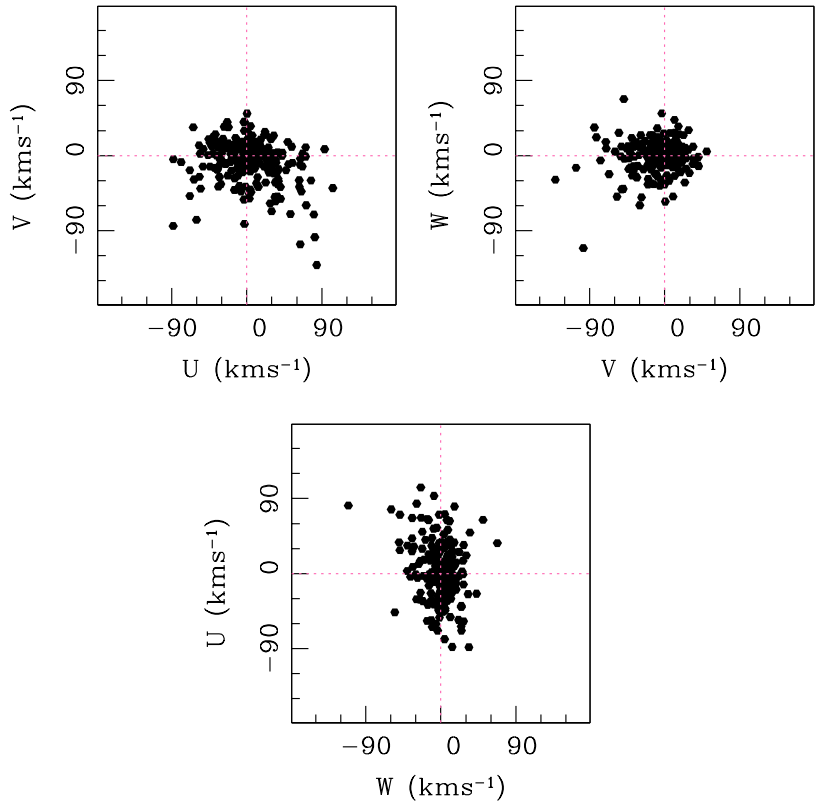

Figure 9.8: The derived Galactic velocities (U, V, W) for target stars.

9.3.1 The Uncertainties In The Velocity Components

The errors of U,V and W space velocities derived by the formula used in Johnson & Soderblom (1987). In Johnson & Soderblom (1987), assumed that the matrices T and A introduce no error into U,V and W; only ρ, μ_α, μ_δ and π contributes. Thus the errors can be written :

$$\begin{bmatrix} {\sigma^2}_U \\ {\sigma^2}_V \\ {\sigma^2}_W \end{bmatrix} = \mathbf{C} \cdot \begin{bmatrix} {\sigma^2}_\rho \\ (k/\pi)^2({\sigma^2}_{\mu_\alpha} + (\mu_\alpha \sigma_\pi/\pi)^2) \\ (k/\pi)^2({\sigma^2}_{\mu_\delta} + (\mu_\delta \sigma_\pi/\pi)^2) \end{bmatrix} + 2\mu_\alpha \mu_\delta k^2 {\sigma^2}_\pi/\pi^4 \begin{bmatrix} b_{12} \cdot b_{13} \\ b_{22} \cdot b_{23} \\ b_{32} \cdot b_{33} \end{bmatrix}$$

The cross terms arise from squaring ∂/∂_π terms. The elements of matrix C are the squares of the indvidual elements of matrix B, $c_{ij} = {b^2}_{ij}$ for all i and j.

In Fig. 9.9, we showed the distribution of the calculated uncertainties for (U, V, W) space velocity components with the mean and sigma values on uncertainties.

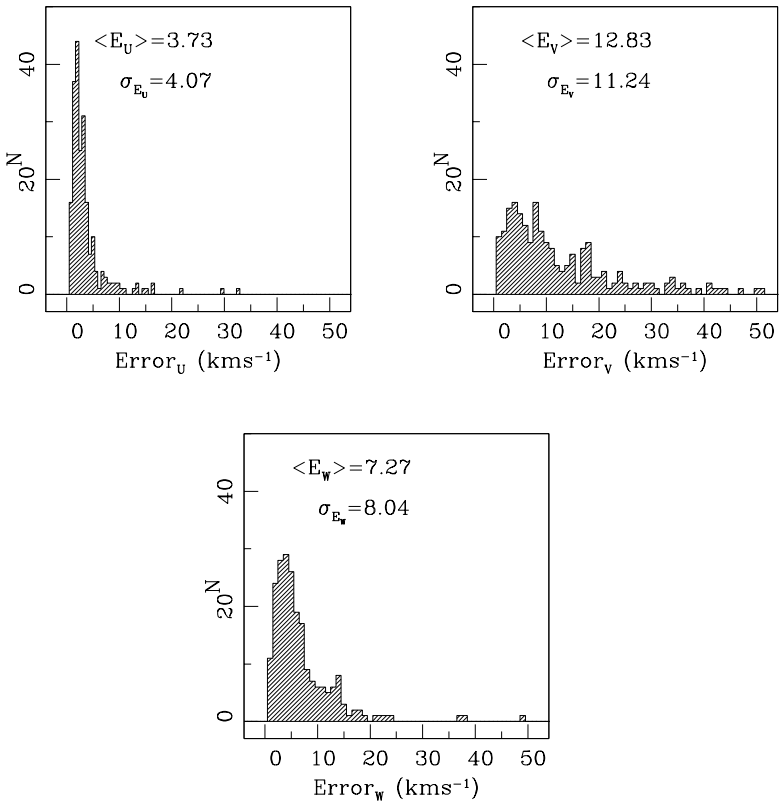

Figure 9.9: The distribution of the uncertainties of the (U, V, W) velocity components.

9.4 The Output Catalog Of 305 Red Clump Stars

The results of our observations are presented in an output catalog (available electronic only via CDS). To be able to work with a homogenous and extensive sample of Red Clump giants, We tried to build our output catalog as similar as possible to that accompanying Valentini & Munari (2010). The major difference is that we do not provide a projected rotation velocity, given the lower resolution of our spectra. In this chapter we will discuss

the content of our output catalog and we represented all the parameters that are derived by our spectroscopic survey.

The output catalog of our survey consist in two parts, with observations for all 245 target stars going into the first part, and the second reporting the results of the re-observations for 60 targets. Both two parts are devided by the all available spectro-photometric data congregated from the literature and other surveys (i.e. Simbad, Hipparcos, 2Mass, Tycho-2, Denis), and the parameters derived by our spectroscopic survey. The content of the output catalog is illustrated in Tab. 9.3. And the derived parameters by the survey are given in for the first epoch observation Tab. 9.4 and the second epoch observation in Tab. 9.5.

Table 9.3: Content and description of the catalog

Characters	Code	Units	Symbol	Description
1-8	I8	...	HD	HD number
9-15	I5	...	HIP	HIP number
16-21	I6	...	TYC1	TYCHO-2 1st identier
25-30	I5	...	TYC2	TYCHO-2 2nd identier
33	I1	...	TYC3	TYCHO-2 3rd identier
37-45	A11	...	spTyp	Spectral type from Michigan catalog
49-61	F12.8	...	RA	Right ascension (J2000)
65-77	F12.8	...	DE	Declination (J2000)
82-90	F8.4	deg	GLat	Galactic latitude
94-102	F8.4	deg	DLon	Galactic longitude
106-112	F6.4	mag	Hp	Hipparcos Hp magnitude
114-120	F6.4	mag	eHp	error on Hp
122-126	F4.2	mag	V-I	(VI)C from Hipparcos catalog
130-134	F4.2	mag	eV-I	error on (VI)C
137-141	F7.2	mas	parHip	Hipparcos (ESA 1997) parallax
143-147	F6.2	mas	eparHip	error on Hipparcos (ESA 1997) parallax
154-158	F7.2	mas	parVL	Hipparcos (van Leeuwen 2007) parallax
163-167	F6.2	mas	eparVL	error Hipparcos (van Leeuwen 2007) parallax
169-175	F6.3	mag	BT	Tycho BT magnitude
178-183	F5.3	mag	eBT	error on Tycho BT magnitude
186-191	F6.3	mag	VT	Tycho VT magnitude
194-199	F5.3	mag	eVT	error on Tycho VT magnitude
201-207	F6.1	mas/yr	pmRA	Tycho-2 RA proper motion
211-213	F4.1	mas/yr	epmRA	error on Tycho-2 RA proper motion
215-221	F6.1	mas/yr	pmDEC	Tycho-2 DEC proper motion
223-226	F4.1	mas/yr	epmDEC	error on Tycho-2 DEC proper motion
230-235	F6.3	mag	J2MASS	2MASS J magnitude
242-247	F5.3	mag	eJ2MASS	error on 2MASS J magnitude
250-255	F6.3	mag	K2MASS	2MASS H magnitude
258-263	F5.3	mag	eK2MASS	error on 2MASS H magnitude
266-271	F6.3	mag	K2MASS	2MASS K magnitude
274-279	F5.3	mag	eK2MASS	error on 2MASS K magnitude
281-284	A3	...	2MASSQF	2MASS quality index
286-291	F6.3	mag	IDENIS	DENIS I magnitude
298-302	F4.2	mag	eIDENIS	error on IDENIS
305-308	I3	...	DENISQF	DENIS quality index
311-327	F16.8	...	HJD	Heliocentric Julian date of Observation
330-334	F4.2	...	FWHM	FWHM of the night sky lines
336-341	F5.1	...	S/N	S/N ratio of the spectra
343-349	F6.1	(kms^1)	RV	Heliocentric radial velocity
354-357	F3.1	(kms^1)	eRV	Error on heliocentric radial velocity
362-366	I5	K	Teff	Effective temperature
371-374	I2	K	eTeff	Error on effective temperature
379-383	F4.2	dex	logg	Surface gravity
388-392	F5.2	dex	elogg	Error on surface gravity
398-403	F5.2	dex	[M/H]	Metallicity
408-412	F4.2	dex	e[M/H]	Error on metallicity
419-424	F6.2	mag	d	spectro-photometric distance
429-433	F5.2	pc	ed	error on spectro-photometric distance
440-447	F9.4	pc	X	Galactic X coordinate
453-460	F9.4	pc	Y	Galactic Y coordinate
466-473	F9.4	pc	Z	Galactic Z coordinate
477-486	F7.2	(kms^1)	U	U velocity
489-498	F7.2	(kms^1)	V	V velocity
501-510	F7.2	(kms^1)	W	W velocity

Name	V_{rad}	E_{Vrad}	T_{eff}	E_{Teff}	$\log g$	$E_{\log g}$	[M/H]	$E_{[M/H]}$	D_{pho}	E_{Dpho}	Gal_X	Gal_Y	Gal_Z	U_{vel}	V_{vel}	W_{vel}
HD	kms^{-1}	kms^{-1}	K	K	dex	dex	dex	dex	pc	pc	pc	pc	pc	kms^{-1}	kms^{-1}	kms^{-1}
127	−17.6	1.6	4748	249	2.84	0.71	−0.04	0.14	271.79	9.39	−23.00	134.83	−243.03	−1.90	−13.23	14.66
342	−16.7	1.8	4791	245	3.00	0.57	−0.08	0.18	271.97	10.02	−34.56	147.17	−226.48	−78.71	−7.89	4.49
1301	−39.3	4.5	4855	258	2.75	0.87	−0.21	0.25	367.83	17.79	−30.43	147.40	−336.47	64.40	−3.53	50.59
1644	−15.6	1.4	4460	196	2.04	0.72	−0.04	0.14	261.85	9.65	−42.16	128.77	−221.43	26.17	−7.29	21.70
2236	4.9	2.3	5077	275	3.18	0.65	0.00	0.10	318.45	14.66	−52.04	144.49	−277.77	−32.08	14.66	−0.66
2690	−4.9	2.7	4581	273	2.41	0.73	0.17	0.24	310.17	15.00	−60.78	145.30	−264.10	14.16	−4.52	9.89
3819	−0.8	4.4	5104	277	3.29	0.59	−0.25	0.25	260.25	9.59	−61.02	115.25	−211.06	−36.30	−0.031	−5.52
3915	−34.5	2.6	4705	224	2.26	0.80	0.00	0.10	375.49	18.16	−90.54	168.67	−320.37	−24.63	−8.98	32.70
6465	28.5	1.2	4562	229	2.71	0.94	−0.25	0.25	401.93	19.43	−118.30	139.12	−335.86	15.43	−9.00	−24.60
7347	4.0	5.3	4706	243	2.47	0.82	−0.25	0.25	323.36	14.15	−100.11	95.38	−304.91	25.95	9.75	14.19
9149	0.4	3.2	4728	216	2.34	0.72	0.08	0.19	414.08	27.65	−159.86	117.66	−367.53	−10.75	−14.80	−1.87
9459	−8.9	1.8	4648	258	2.33	0.71	−0.33	0.24	401.03	21.24	−166.65	131.83	−314.68	−6.95	−42.87	−3.05
10642	15.0	2.1	4771	215	3.04	0.77	0.13	0.22	240.73	8.87	−105.81	63.00	−207.16	−6.01	−16.47	−16.60
10816	21.6	3.4	4790	300	2.72	0.62	−0.04	0.14	279.48	10.94	−118.02	61.25	−246.19	22.76	−32.20	−12.42
10930	20.0	2.0	4523	234	2.32	0.80	0.00	0.10	227.12	7.84	−102.32	56.96	−194.81	31.11	2.23	2.86
10955	23.1	4.9	4729	277	2.67	0.69	0.04	0.14	228.62	8.42	−102.49	55.55	−198.39	−5.09	15.80	−15.74
11028	56.1	0.5	4854	294	2.73	0.63	−0.25	0.25	252.77	9.31	−114.66	62.00	−218.82	32.32	24.12	−32.24
11455	11.1	2.4	4914	256	3.10	0.62	−0.38	0.22	244.65	10.70	−123.63	70.69	−202.79	−9.21	10.89	−5.95
12343	17.3	3.7	5102	296	3.16	0.69	−0.29	0.25	275.35	10.78	−132.73	67.77	−200.85	−0.27	11.31	−7.84
12378	16.2	1.7	4646	278	2.37	0.67	−0.38	0.21	352.80	19.50	−170.09	67.25	−302.62	−3.43	40.18	−1.58
12607	45.5	5.5	4727	235	2.55	0.66	−0.50	0.10	263.22	9.09	−133.94	57.00	−219.28	53.83	10.68	−8.54
12784	22.6	2.2	4853	237	3.29	0.55	−0.42	0.18	482.31	25.54	−216.39	66.79	−400.74	4.67	35.37	−6.80
14204	24.4	5.2	4479	257	2.25	0.69	0.00	0.10	220.23	7.61	−114.00	28.22	−184.25	−2.80	40.54	−12.79
14427	4.3	4.7	4791	246	2.67	0.59	−0.08	0.18	373.71	20.65	−196.76	45.29	−314.82	1.79	6.21	8.74
14712	−19.9	2.9	4725	191	2.75	0.63	−0.08	0.18	283.92	12.42	−159.62	41.84	−235.79	−52.58	−13.07	−1.64

Table 9.4: Continues

Name	V_{rad}	E_{Vrad}	T_{eff}	E_{Teff}	$\log g$	$E_{\log g}$	[M/H]	$E_{[M/H]}$	D_{pho}	E_{Dpho}	Gal_X	Gal_Y	Gal_Z	U_{vel}	V_{vel}	W_{vel}
HD	kms^{-1}	kms^{-1}	K	K	dex	dex	dex	dex	pc	pc	pc	pc	pc	kms^{-1}	kms^{-1}	kms^{-1}
15031	53.7	4.2	4499	176	2.38	0.95	0.12	0.22	354.48	19.59	−211.9229	56.2996	−297.6527	33.61	−49.73	−39.96
15390	−16.0	2.1	4584	254	2.09	0.70	0.16	0.24	331.62	16.03	−180.9901	26.8561	−280.0207	−32.86	−25.72	7.99
15780	16.0	2.5	4109	189	1.42	0.84	0.00	0.10	848.28	29.30	−125.3169	21.8267	−178.7614	29.80	−153.84	−4.69
16061	0.2	3.7	5188	252	3.46	0.48	−0.20	0.25	346.70	15.17	−189.8449	44.0760	−242.1009	−7.91	8.05	8.01
16658	−9.2	3.9	4853	254	2.42	0.60	−0.20	0.25	318.71	13.94	−191.3001	28.1440	−252.3343	−12.18	12.38	17.26
16710	−1.3	5.6	4728	216	2.09	0.67	0.00	0.10	340.01	15.66	−175.1668	12.9345	−250.4478	15.30	11.78	26.49
17295	32.5	2.4	4916	210	3.23	0.60	0.08	0.18	275.75	15.24	−169.3688	15.4698	−219.7801	52.37	−70.06	8.44
17370	70.3	5.8	4874	258	2.83	0.77	−0.16	0.23	388.58	17.89	−233.0022	11.7059	−314.7700	67.05	2.41	−23.62
18176	−0.3	4.2	4668	234	2.01	0.73	0.00	0.10	216.96	9.99	−134.4661	1.3673	−172.5990	−14.90	−41.18	3.32
18682	−76.3	3.5	4489	175	2.34	0.78	−0.46	0.13	217.46	8.01	−151.6105	10.6314	−169.8224	−88.33	−84.36	33.67
18976	29.7	4.3	4709	225	2.54	0.66	−0.04	0.14	944.75	47.86	−166.1604	−3.3399	−200.7285	25.53	−11.22	−1.61
19271	20.5	2.2	4167	117	1.25	0.80	−0.04	0.13	278.53	11.54	−210.6082	14.5632	−219.8526	37.46	−88.28	17.63
19847	20.9	2.6	5165	308	3.56	0.45	−0.38	0.22	236.29	8.16	−175.3046	15.2401	−167.1506	−1.06	9.34	−13.95
20055	11.4	2.1	4378	214	2.68	0.80	0.13	0.22	273.34	12.59	−220.4326	4.5574	−224.1340	−14.35	−41.27	−14.16
20214	20.3	3.3	4602	257	2.70	0.56	−0.16	0.23	300.05	13.13	−226.8544	1.0199	−231.1866	21.10	24.63	9.30
20792	62.1	5.8	4792	283	2.04	0.80	−0.38	0.22	237.79	8.21	−162.3415	−15.7873	−174.8280	70.57	−1.17	−1.84
21195	−15.7	2.4	4853	214	2.96	0.72	−0.24	0.25	313.35	13.71	−260.0580	1.4647	−234.3879	−13.08	6.33	27.17
21365	65.7	1.9	4832	234	3.17	0.51	−0.41	0.19	319.69	12.51	−256.8303	0.6755	−228.1008	27.98	−57.30	−49.21
21838	−6.4	2.7	4731	305	2.32	0.65	−0.46	0.14	248.59	8.59	−174.1262	−32.9166	−186.1332	−11.75	−7.73	17.68
21926	16.9	4.2	4706	224	2.58	0.64	0.00	0.10	270.69	9.97	−211.6354	−15.7454	−195.5825	3.96	−19.18	−0.23
22199	−2.9	5.1	4937	207	2.46	0.75	−0.46	0.14	304.95	13.34	−246.8246	−18.7958	−222.4414	−14.80	−27.37	9.43
22271	86.0	5.5	4273	160	2.75	0.52	0.38	0.21	307.49	14.87	−264.3100	−15.4534	−231.2005	66.72	−13.15	−34.25
22673	67.4	7.1	4668	213	2.42	0.70	−0.08	0.18	269.83	9.94	−210.9048	−23.9352	−190.1875	42.25	−0.11	−34.49
23364	59.1	3.9	4729	216	2.75	0.80	0.04	0.14	340.48	18.81	−268.0549	−51.5339	−249.4852	26.72	−20.20	−34.53
23876	77.7	7.4	4438	226	2.53	0.65	0.04	0.14	290.15	13.36	−252.9559	−42.2087	−219.0960	37.57	−27.80	−50.05

Table 9.4: Continues

Name HD	V_{rad} kms^{-1}	E_{Vrad} kms^{-1}	T_{eff} K	E_{Teff} K	$\log g$ dex	$E_{\log g}$ dex	[M/H] dex	$E_{[M/H]}$ dex	D_{pho} pc	E_{Dpho} pc	Gal_X pc	Gal_Y pc	Gal_Z pc	U_{vel} kms^{-1}	V_{vel} kms^{-1}	W_{vel} kms^{-1}
24604	2.9	3.9	4936	251	2.55	0.56	0.00	0.10	214.86	8.41	−182.9254	−43.8105	−161.7794	−12.34	19.29	−2.16
25114	37.1	5.6	4502	179	2.25	0.56	0.17	0.24	229.10	9.49	−226.3027	−24.2267	−160.1594	27.19	−14.15	−0.94
25542	37.4	2.9	4753	249	2.64	0.58	0.00	0.10	242.32	8.93	−212.6431	−49.2943	−169.8839	30.50	−12.45	3.77
25980	20.2	5.0	4874	239	2.97	0.62	0.00	0.10	297.35	10.95	−258.1564	−60.3637	−199.3399	9.41	−15.38	6.68
26065	41.9	4.2	4498	179	2.75	0.55	0.04	0.14	256.45	11.22	−296.7043	−45.1075	−203.1394	11.47	−33.27	−26.39
26373	29.4	6.7	4891	275	2.20	0.74	−0.21	0.25	225.45	7.27	−225.7322	−41.6182	−157.0112	−0.75	5.20	−30.06
27008	−3.6	1.5	4934	230	2.65	0.79	−0.29	0.25	213.36	8.35	−194.6894	−42.0119	−132.2871	−6.10	13.81	18.53
27324	−36.6	1.8	4935	230	2.74	0.69	−0.21	0.25	211.26	8.27	−192.8908	−39.1701	−124.6910	−52.11	7.93	11.38
27351	−4.4	1.9	5066	252	3.00	0.67	−0.21	0.25	232.39	8.56	−185.6369	−46.8727	−128.3438	−21.17	10.22	−0.81
28737	−0.8	5.2	4476	187	2.22	0.83	−0.33	0.24	277.92	12.16	−229.8156	−68.5752	−146.0509	−22.79	−23.98	5.00
28959	−0.6	1.7	4127	125	1.51	0.78	0.00	0.10	362.47	20.86	−193.9963	−68.8944	−130.0433	−3.74	13.97	16.05
28956	34.1	6.5	4940	232	2.58	0.84	0.00	0.10	242.43	8.37	−328.8731	−80.9178	−189.5163	16.55	18.94	−19.98
29913	16.6	3.9	4647	237	2.46	0.80	0.00	0.10	237.20	8.74	−219.4004	−48.4379	−108.2479	−3.84	−18.20	−5.54
29914	−1.8	5.9	4958	225	2.62	0.71	−0.25	0.25	217.44	8.01	−202.6439	−52.9193	−106.5832	−13.42	12.10	4.08
30057	25.3	3.6	4977	216	2.70	0.75	−0.12	0.21	242.87	8.95	−196.6106	−72.5132	−119.0257	11.80	−7.03	2.94
30172	39.7	1.7	5127	384	3.46	0.48	−0.33	0.24	283.84	10.46	−236.7904	−62.4862	−121.3205	7.89	−15.75	−33.56
30356	−19.6	2.5	4355	156	2.04	0.79	−0.21	0.25	290.93	12.06	−260.8050	−79.4191	−139.3979	−56.71	−25.44	−16.41
30510	15.7	2.6	4207	171	1.68	0.94	0.16	0.23	1150.66	47.69	−259.7910	−84.9459	−141.1049	−17.15	−45.85	−5.98
30618	−27.7	4.3	4854	294	3.05	0.69	−0.21	0.25	290.51	11.37	−258.4015	−68.1168	−125.6617	−24.11	11.68	42.89
30979	72.1	3.5	4871	309	2.95	0.66	−0.25	0.25	343.24	15.02	−272.0814	−89.6584	−141.2425	62.80	−29.61	10.14
31256	−16.4	2.1	4416	234	2.88	0.72	0.38	0.21	254.46	9.96	−218.4520	−80.5436	−117.0633	−29.99	2.70	12.09
32951	1.8	4.9	5043	247	3.04	0.66	−0.12	0.21	268.62	10.51	−238.2625	−85.1748	−106.1678	−12.09	−4.82	10.51
33278	0.4	3.7	4765	237	2.28	0.72	0.04	0.14	313.07	13.70	−280.7535	−119.1109	−134.9529	−33.00	−11.76	−21.57
34909	−4.1	2.1	4994	348	2.76	0.75	−0.37	0.22	210.13	7.74	−205.4027	−107.6249	−97.6175	−31.91	−4.94	−10.80
34966	−2.9	1.1	5165	275	2.97	0.56	0.04	0.14	223.45	7.72	−198.0608	−91.8905	−85.2726	−15.93	12.88	−0.67

Table 9.4: Continues

Name HD	V_{rad} kms^{-1}	E_{Vrad} kms^{-1}	T_{eff} K	E_{Teff} K	$\log g$ dex	$E_{\log g}$ dex	[M/H] dex	$E_{[M/H]}$ dex	D_{pho} pc	E_{Dpho} pc	Gal_X pc	Gal_Y pc	Gal_Z pc	U_{vel} kms^{-1}	V_{vel} kms^{-1}	W_{vel} kms^{-1}
35220	−20.0	1.0	4354	213	2.39	0.67	−0.04	0.13	211.59	7.79	−208.8072	−98.2399	−88.3566	−27.11	34.46	−3.41
35778	3.7	2.4	4101	122	2.05	0.81	0.04	0.14	240.20	9.95	−249.3120	−126.8851	−105.8513	−5.30	5.37	14.54
70435	36.5	1.0	4975	276	2.92	0.67	−0.20	0.25	229.96	7.94	−153.0947	−147.1052	77.1549	20.53	−13.08	7.55
71094	24.3	3.1	4896	277	2.67	0.83	−0.42	0.18	342.75	16.57	−216.2426	−187.1118	118.4001	23.32	−4.34	−14.39
72212	−0.3	6.4	4564	270	1.99	0.73	0.00	0.10	290.63	12.04	−191.8281	−192.7476	110.1540	−15.81	6.29	8.24
73413	61.3	2.9	5040	284	2.95	0.63	−0.04	0.14	228.67	8.42	−141.4087	−154.8672	87.4045	64.09	−11.12	7.46
73686	19.8	2.0	4940	271	2.54	0.72	−0.17	0.24	252.45	9.30	−141.5382	−167.3225	87.5564	8.06	−3.77	3.13
73891	25.2	1.3	4688	178	2.62	0.85	−0.17	0.24	364.12	19.28	−223.1670	−252.3828	141.7381	25.12	−2.66	−7.47
74059	21.9	4.6	5021	259	2.95	0.66	−0.16	0.23	359.65	15.73	−210.6773	−209.6210	139.2456	9.29	2.16	16.31
74349	15.2	4.7	4980	341	2.88	0.65	−0.37	0.22	348.60	15.25	−206.1891	−225.6121	137.1503	4.98	0.09	3.83
74444	22.0	3.7	4354	187	2.16	0.65	0.00	0.10	264.68	9.75	−166.9807	−159.5987	114.4839	−0.94	−1.20	26.49
74816	15.2	2.2	5063	307	3.29	0.52	−0.25	0.25	329.26	13.65	−204.2682	−220.5000	141.2256	1.09	0.15	9.94
75559	17.1	2.7	4852	311	2.41	0.61	−0.12	0.21	350.40	14.52	−201.1930	−242.0097	145.2041	13.27	12.59	18.39
75996	72.9	2.7	4581	212	2.79	0.62	0.12	0.22	255.52	10.00	−155.1043	−161.3237	118.2241	40.70	−51.83	10.99
76082	56.9	2.6	4644	214	2.50	0.67	0.04	0.14	311.07	13.61	−183.0423	−207.8582	139.0270	34.19	−32.10	11.39
76399	16.7	2.1	4501	203	2.38	1.11	0.25	0.25	279.84	10.31	−167.0100	−182.0514	130.4965	−2.71	−8.61	6.23
76525	9.9	4.8	4106	123	1.34	0.77	−0.16	0.31	1024.91	40.12	−153.9200	−171.3474	121.2634	47.39	30.00	−17.57
76767	−3.8	6.8	4875	276	2.25	0.62	−0.50	0.10	305.74	11.26	−185.8011	−196.7782	149.7424	−36.39	−16.13	−3.59
77055	16.6	3.4	4564	181	2.49	0.85	−0.42	0.18	346.94	15.18	−178.3697	−240.4817	143.9085	−1.72	−3.98	10.18
77858	22.9	2.4	4978	237	2.95	0.65	−0.16	0.23	314.76	14.49	−183.0258	−208.0072	159.1063	−3.55	−17.88	7.97
78664	40.2	3.1	4315	206	2.25	0.63	0.00	0.10	275.69	10.16	−147.3270	−184.7371	134.7256	25.07	−16.34	12.49
79410	64.5	4.5	4728	216	2.59	0.80	−0.08	0.19	225.40	7.78	−119.3058	−148.3981	114.9169	65.51	−43.08	−16.23
80163	−15.8	1.9	4645	276	2.97	0.68	−0.20	0.25	225.93	8.84	−119.9213	−148.0957	121.5012	−40.48	1.95	−3.16
80477	77.9	3.1	4605	257	2.41	0.78	0.17	0.24	323.81	17.15	−166.7338	−218.2824	172.5919	34.37	−54.89	27.39
80733	42.6	2.6	4791	246	2.75	0.48	0.00	0.10	308.23	14.19	−163.4189	−182.6464	170.9268	40.39	−37.59	−18.45

Table 9.4: Continues

Name HD	V_{rad} kms^{-1}	E_{Vrad} kms^{-1}	T_{eff} K	E_{Teff} K	$\log g$ dex	$E_{\log g}$ dex	[M/H] dex	$E_{[M/H]}$ dex	D_{pho} pc	E_{Dpho} pc	Gal_X pc	Gal_Y pc	Gal_Z pc	U_{vel} kms^{-1}	V_{vel} kms^{-1}	W_{vel} kms^{-1}
81325	−1.2	4.0	4832	234	2.53	0.63	−0.12	0.21	272.62	11.93	−146.9986	−167.1114	159.8161	6.50	24.21	3.74
81489	14.6	1.6	4500	201	2.38	0.77	−0.04	0.13	397.95	28.41	−216.0859	−244.7180	237.4736	−55.48	−39.59	21.24
81643	−9.0	3.9	4540	196	2.54	0.66	0.00	0.10	340.12	18.01	−164.5342	−233.7024	185.2567	−3.82	−6.01	−36.31
81691	8.9	4.6	4500	266	2.38	0.92	−0.29	0.25	369.42	17.86	−185.5860	−236.1785	208.2494	4.20	−4.48	−7.42
82333	16.5	3.9	4689	206	2.33	0.77	−0.46	0.14	236.08	9.24	−124.1940	−156.2278	145.6953	14.74	2.65	5.11
82462	18.3	3.3	4750	204	2.92	0.67	0.25	0.25	286.93	10.57	−126.7783	−205.3685	153.6368	−9.31	−15.14	5.73
82841	42.7	3.2	4499	175	3.43	0.60	0.00	0.10	306.71	11.30	−143.8075	−204.6584	176.9613	4.06	−40.72	9.86
82888	−5.9	5.2	4979	278	2.46	0.77	−0.42	0.19	240.37	8.86	−117.3543	−160.2286	144.1385	1.38	28.30	7.09
83024	6.2	5.0	4829	235	3.22	0.65	0.04	0.14	239.89	8.84	−118.7239	−151.1722	146.0328	70.58	9.99	−49.14
83046	14.6	2.4	5044	301	3.17	0.69	−0.17	0.24	227.28	7.33	−107.4515	−150.1720	133.7406	−18.26	−18.08	6.04
85845	−2.8	4.8	5310	354	3.17	0.66	−0.17	0.24	236.89	8.73	−91.6790	−163.4729	146.6819	−1.77	11.18	−2.32
85990	9.7	3.0	4647	215	3.25	0.38	0.08	0.19	246.12	9.07	−98.3812	−166.3887	157.4371	−68.26	−48.45	−3.90
86477	21.5	2.9	4812	271	2.58	0.60	0.04	0.14	375.21	24.19	−148.0694	−241.6613	243.8780	−1.32	−37.34	−13.04
86708	−17.5	1.4	4791	283	2.36	0.70	−0.29	0.25	431.48	34.77	−165.2548	−289.2930	280.9307	−21.96	33.98	10.73
86901	22.6	2.9	4604	214	2.55	0.48	0.21	0.25	423.63	26.34	−165.5524	−267.2858	280.4361	7.04	−15.02	6.26
87740	−19.4	1.4	4897	328	2.62	0.76	−0.46	0.14	423.49	26.33	−148.8634	−224.7956	263.5064	−37.91	15.67	−0.83
88083	−21.2	3.2	4504	204	2.30	0.52	0.17	0.24	239.03	11.01	−82.9331	−161.1420	160.5235	−45.66	19.77	2.43
88803	−1.5	4.6	4478	189	2.41	0.87	0.21	0.25	260.87	11.41	−86.8090	−172.7394	179.4875	−5.94	−2.48	−9.97
88866	38.2	2.4	4453	282	2.13	0.68	0.00	0.10	276.12	11.44	−95.4775	−174.6500	193.5025	38.01	−30.76	0.59
89603	−24.6	3.2	4436	181	2.72	0.68	0.16	0.23	283.10	13.04	−101.4695	−171.3762	213.5372	−30.92	−4.69	−29.12
90184	32.3	5.9	5019	295	3.26	0.56	0.12	0.22	366.52	17.72	−104.7967	−248.4817	258.4119	47.02	−17.46	3.37
90305	15.6	1.8	4960	283	3.02	0.63	−0.21	0.25	288.97	10.65	−92.1637	−184.1959	216.3317	33.05	−3.31	−1.81
90983	67.2	4.3	4412	184	2.21	0.55	0.08	0.18	263.85	9.72	−82.8614	−153.7740	200.0772	−2.88	−82.01	21.94
91565	1.5	1.7	4540	201	2.21	0.94	−0.42	0.27	345.24	19.08	−83.7070	−237.2587	249.7432	−4.90	16.69	13.00
92425	4.9	4.2	4355	214	2.80	0.66	0.21	0.25	322.83	14.12	−94.1886	−189.7093	262.8928	−12.18	−4.17	3.29

Table 9.4: Continues

Name HD	V_{rad} kms^{-1}	E_{Vrad} kms^{-1}	T_{eff} K	E_{Teff} K	$\log g$ dex	$E_{\log g}$ dex	[M/H] dex	$E_{[M/H]}$ dex	D_{pho} pc	E_{Dpho} pc	Gal_X pc	Gal_Y pc	Gal_Z pc	U_{vel} kms^{-1}	V_{vel} kms^{-1}	W_{vel} kms^{-1}
92687	−0.2	3.1	5080	257	2.59	0.61	−0.25	0.25	297.97	13.04	−79.1896	−174.0918	233.4615	−22.25	14.68	13.81
92929	49.2	6.3	4895	189	3.00	0.57	−0.25	0.25	394.67	21.81	−83.9046	−265.8460	296.8127	63.04	−37.53	10.55
93275	26.1	3.0	4688	229	2.63	0.89	0.00	0.10	326.04	14.26	−67.3775	−212.1015	245.0188	34.98	−8.57	13.12
93878	−12.7	3.3	4476	160	2.44	0.88	−0.42	0.18	408.10	21.61	−101.7208	−227.0456	332.5316	81.58	−97.76	−110.96
94819	−4.1	5.7	4271	158	1.67	0.85	0.08	0.19	1440.01	72.95	−80.9037	−208.4139	305.5425	−36.23	16.80	12.99
95832	0.2	2.6	4794	283	2.88	0.71	−0.25	0.25	336.01	16.25	−51.1512	−210.7674	271.2526	−7.97	13.62	9.08
96720	5.1	5.5	4707	200	1.46	0.69	0.00	0.10	826.31	30.44	−26.9848	−132.5953	171.3044	31.37	−67.50	−53.61
96742	9.5	4.4	4792	247	2.71	0.65	0.00	0.10	267.92	10.49	−36.9436	−159.6973	216.5606	5.53	−6.02	3.88
96796	4.0	2.6	4869	234	2.46	0.65	−0.21	0.25	280.71	12.93	−33.6479	−177.5566	225.1426	−35.30	−16.98	−5.98
97892	−14.6	4.2	4521	214	2.25	0.69	−0.16	0.23	304.31	13.31	−36.8395	−174.1318	252.9574	−44.01	15.33	−2.75
99179	18.1	3.1	4542	172	2.05	0.72	0.08	0.19	312.70	16.56	−28.3610	−170.6621	264.5550	8.47	−8.80	14.04
99226	14.9	4.6	4767	238	3.13	0.77	−0.04	0.14	354.11	19.57	−14.1370	−220.3378	283.0767	32.55	−21.17	−1.10
99689	6.9	4.8	4955	246	3.13	0.62	−0.04	0.14	269.27	10.54	−12.5885	−159.3407	221.8099	−15.44	1.83	9.40
100629	20.9	4.1	4686	208	2.13	0.79	0.04	0.14	227.70	9.96	−4.5710	−128.9657	184.9249	49.22	16.40	34.96
100763	32.2	5.2	4751	249	2.62	0.58	−0.04	0.14	380.63	22.79	−14.8369	−202.1613	318.4603	13.84	−37.38	13.51
100975	5.0	2.4	4542	283	2.49	0.68	0.00	0.10	227.09	8.37	−6.0389	−121.6811	187.9714	−0.61	5.67	9.37
101092	16.8	3.0	4788	283	2.66	0.71	−0.16	0.23	291.75	12.76	−17.1132	−140.3277	251.7200	38.21	−16.45	7.86
102106	−2.2	3.3	4579	210	2.29	0.74	−0.08	0.18	333.00	16.87	−3.1678	−168.5063	284.1826	−41.80	10.79	4.84
102274	−14.1	4.2	4250	174	2.29	0.85	0.00	0.10	217.36	8.01	6.0778	−121.0105	179.7825	50.07	−10.34	−22.17
103341	17.0	2.3	4520	216	1.95	0.59	−0.42	0.18	1100.62	38.01	11.6454	−147.7549	243.0781	28.02	−47.50	−6.66
103476	13.0	3.6	4769	258	2.50	0.64	−0.16	0.23	301.80	11.12	16.6535	−160.3693	253.1094	−44.20	−13.29	4.94
103752	−7.1	2.7	4186	148	1.71	0.48	0.08	0.18	1217.12	44.84	7.2099	−147.2062	277.8284	175.48	−253.53	−136.21
105323	1.3	4.4	4915	234	1.88	0.74	−0.46	0.14	1717.47	114.68	34.6151	−208.6654	390.6074	184.57	−245.50	−111.13
105587	1.9	4.8	4730	216	2.42	0.81	−0.04	0.14	324.46	13.45	20.6168	−139.5996	288.7644	10.44	14.72	12.54
106316	−3.0	7.8	4705	199	2.20	0.78	0.00	0.10	237.99	8.22	26.6413	−111.8590	205.7481	31.01	2.70	4.53

Table 9.4: Continues

Name HD	V_{rad} kms^{-1}	E_{Vrad} kms^{-1}	T_{eff} K	E_{Teff} K	$\log g$ dex	$E_{\log g}$ dex	[M/H] dex	$E_{[M/H]}$ dex	D_{pho} pc	E_{Dpho} pc	Gal_X pc	Gal_Y pc	Gal_Z pc	U_{vel} kms^{-1}	V_{vel} kms^{-1}	W_{vel} kms^{-1}
106497	−6.8	1.6	5021	277	2.67	0.66	−0.33	0.24	420.47	20.33	44.2888	−178.1452	329.2898	−55.90	2.33	−11.48
106695	28.5	5.5	4771	237	2.07	0.86	−0.42	0.18	264.19	9.12	40.9354	−137.7628	223.8341	2.87	−45.60	8.55
106775	16.6	3.1	5038	202	2.67	0.62	−0.16	0.23	254.99	8.81	36.1240	−126.5552	218.8790	−8.36	−13.53	12.63
106817	3.6	2.2	4791	301	2.79	0.52	0.00	0.10	238.94	8.25	27.6855	−108.3025	210.0012	14.31	−9.52	3.87
107069	−18.7	1.7	4459	244	2.75	0.66	0.34	0.23	338.68	15.60	31.0418	−135.0190	303.4720	103.24	−38.98	−24.04
107136	74.5	2.8	4646	216	2.34	0.59	−0.04	0.14	443.82	25.55	64.6637	−215.3318	386.4573	36.61	−49.01	67.72
108263	20.3	4.5	4707	225	2.54	0.59	0.04	0.14	285.80	11.19	42.8236	−123.6030	253.5440	37.10	−34.08	15.99
108850	−10.9	2.8	4832	307	1.76	0.56	−0.46	0.14	1751.31	112.9	75.0315	−192.0743	404.2427	−6.10	0.59	−9.29
108978	−15.4	2.0	4687	208	2.38	0.86	0.09	0.19	348.51	20.06	53.1525	−137.8798	312.7472	9.07	11.29	−6.49
109757	−16.4	4.1	4502	205	2.33	1.14	0.12	0.22	459.30	28.55	107.5135	−218.5155	390.2459	−4.99	−19.81	−28.03
110123	−11.8	0.9	4920	255	3.63	0.36	−0.04	0.24	246.99	8.53	57.5869	−111.9746	215.2808	33.48	−20.31	−11.16
111030	−10.5	4.3	4417	211	1.93	0.77	0.00	0.10	1137.20	49.75	61.5656	−106.9142	266.6411	95.85	−108.78	−27.99
111544	23.3	5.2	4271	120	1.34	0.66	−0.54	0.14	1136.20	41.86	69.1734	−110.0630	261.1323	47.59	−221.36	−49.48
111909	−24.3	3.7	4855	277	2.87	0.73	−0.50	0.10	263.21	8.48	55.3359	−83.3021	212.6586	−23.56	40.11	−11.81
111940	−1.9	3.3	5020	238	2.95	0.63	−0.12	0.22	368.40	16.12	82.4205	−123.2216	317.7163	−0.57	8.83	6.68
112222	8.2	2.7	4689	269	2.83	0.66	0.17	0.24	258.69	9.53	62.1481	−88.4961	233.9131	−8.83	−36.53	−1.47
112282	37.5	3.6	4267	159	1.87	0.64	0.00	0.10	1438.14	72.85	102.9136	−146.2928	324.4649	−107.08	−149.08	−52.98
112477	5.7	2.3	4208	170	2.13	0.74	0.16	0.23	424.78	25.43	116.9143	−161.8762	371.4270	−34.68	9.71	5.31
112739	−6.9	6.0	4871	238	2.34	0.85	−0.08	0.18	227.20	7.85	65.7935	−87.9668	196.0182	29.81	−66.67	−22.23
113641	16.0	6.6	4951	224	2.78	0.88	−0.29	0.25	404.58	20.49	123.3543	−146.2231	352.5390	−19.25	1.99	18.40
115724	−18.0	3.5	4539	197	2.84	0.74	−0.04	0.14	337.31	14.76	120.2774	−111.5069	293.9373	83.84	−131.20	−28.99
117349	6.3	3.5	4186	177	0.92	0.81	−0.04	0.14	1324.27	73.18	137.6951	−106.0609	301.2573	−35.35	4.38	0.53
117406	2.6	2.6	4710	248	2.65	0.71	−0.42	0.19	368.80	16.98	126.6395	−93.1822	291.3876	−22.37	10.15	4.47
117529	−3.2	5.0	4665	233	2.96	0.88	0.00	0.10	372.40	20.58	154.8997	−120.3696	321.0042	80.42	−70.70	16.41
117557	−16.6	2.7	4543	200	2.21	0.56	0.04	0.14	328.36	15.12	135.5795	−103.8933	285.2729	36.98	3.73	7.50

Table 9.4: Continues

Name HD	V_{rad} kms^{-1}	E_{Vrad} kms^{-1}	T_{eff} K	E_{Teff} K	$\log g$ dex	$E_{\log g}$ dex	[M/H] dex	$E_{[M/H]}$ dex	D_{pho} pc	E_{Dpho} pc	Gal_X pc	Gal_Y pc	Gal_Z pc	U_{vel} kms^{-1}	V_{vel} kms^{-1}	W_{vel} kms^{-1}
117914	−18.5	7.3	4310	204	2.12	0.87	0.04	0.14	284.71	12.46	113.7055	−77.3203	258.3910	19.37	−0.39	−4.27
118390	1.7	3.6	4789	283	2.83	0.51	0.00	0.10	296.57	12.29	124.1020	−84.4974	255.7938	−30.11	11.66	−0.40
119373	−12.5	3.3	4667	235	1.80	0.72	0.00	0.10	893.05	30.84	106.1461	−67.1337	200.2774	224.16	−173.95	54.52
120967	−7.5	6.9	4770	258	3.21	0.80	0.00	0.10	258.19	9.51	118.1083	−55.9650	225.2255	19.79	7.65	13.29
121627	0.4	2.8	4166	155	1.20	0.77	−0.38	0.30	1691.28	124.6	223.8109	−114.5155	369.9624	12.78	−1.55	17.55
121814	−26.7	3.9	4459	173	3.23	0.56	0.12	0.21	325.94	17.26	167.8274	−81.5585	281.7065	64.18	−106.34	−14.63
122346	−34.0	6.8	4771	258	3.17	0.65	−0.17	0.24	389.41	26.00	189.1531	−74.2414	337.4412	−46.38	0.67	−55.18
122575	−35.1	3.1	4876	191	2.42	0.81	−0.46	0.14	279.34	10.93	151.0094	−67.2331	243.6129	29.03	19.65	−8.66
123211	−7.0	6.1	4309	203	2.16	0.65	−0.04	0.14	306.69	12.71	172.7707	−77.5172	259.1956	−37.57	25.53	−15.53
123324	−49.3	2.7	4226	159	1.75	0.43	−0.37	0.22	943.55	32.59	122.9185	−42.9419	209.7776	−13.33	−229.07	−101.95
123410	36.2	9.3	4433	206	1.80	0.82	0.00	0.10	256.24	8.85	140.4224	−53.9265	226.1416	−18.23	−198.82	−4.50
123509	34.3	1.2	4354	236	2.43	0.83	0.16	0.23	247.63	8.55	131.7621	−49.9552	211.4475	−38.65	−14.57	24.49
124069	−22.9	1.6	4832	234	2.53	0.72	−0.28	0.25	269.34	9.92	132.3042	−40.1240	221.8459	14.19	8.73	−5.80
125978	47.6	1.0	4896	237	3.04	0.66	−0.29	0.25	285.17	11.82	149.6529	−26.9357	243.2901	−88.05	−4.37	13.59
127414	−12.2	2.9	4374	189	2.02	0.79	0.16	0.23	323.63	14.16	182.7527	−23.9554	277.8186	−30.95	−34.19	−25.15
127988	−100.6	2.3	4249	174	2.20	0.77	0.00	0.10	308.97	14.23	180.3669	−27.3675	256.4271	76.96	−29.83	−59.48
129449	12.8	1.1	4893	237	2.34	0.66	−0.25	0.25	230.09	8.48	136.5926	−12.8014	186.2210	−19.47	−7.58	14.84
129887	11.5	1.4	4833	211	2.50	0.74	−0.33	0.24	242.76	8.38	142.9082	−8.0091	197.2379	−23.46	8.46	11.53
130969	−3.2	1.4	5062	251	3.59	0.45	−0.20	0.25	296.50	15.02	191.9578	−18.5169	233.7057	21.77	28.67	30.52
131455	−11.4	4.7	4688	181	3.06	0.78	0.00	0.10	247.12	10.81	163.5835	−14.8317	193.7433	1.41	19.88	2.54
132587	22.2	7.9	4750	204	3.21	0.52	0.00	0.10	378.65	27.90	267.8458	−23.5677	294.2535	−64.15	33.86	−10.23
133583	11.5	7.3	4545	199	2.84	0.73	0.00	0.10	240.42	11.07	165.6241	−3.2478	185.7668	−17.86	−3.09	15.33
133927	9.4	4.8	4894	214	2.96	0.43	0.00	0.10	271.54	11.88	195.8874	13.4295	238.4680	−25.53	−10.30	7.79
133893	4.2	2.8	4582	235	2.83	0.77	0.21	0.25	304.77	17.54	198.6545	−12.7531	206.4655	2.57	16.97	25.47
133987	−31.7	7.6	4706	200	2.04	0.72	0.00	0.10	231.30	9.05	158.7201	−3.0531	173.6799	15.40	13.59	−12.52

Table 9.4: Continues

Name HD	V_{rad} kms^{-1}	E_{Vrad} kms^{-1}	T_{eff} K	E_{Teff} K	$\log g$ dex	$E_{\log g}$ dex	[M/H] dex	$E_{[M/H]}$ dex	D_{pho} pc	E_{Dpho} pc	Gal_X pc	Gal_Y pc	Gal_Z pc	U_{vel} kms^{-1}	V_{vel} kms^{-1}	W_{vel} kms^{-1}
134408	−18.3	2.0	4708	198	2.57	0.60	−0.12	0.22	218.85	7.56	149.9301	0.5982	164.2631	9.65	16.45	0.32
136515	8.7	0.5	4855	238	3.25	0.63	−0.08	0.18	268.96	9.91	196.9147	6.4931	195.8451	−37.28	17.83	−8.15
137929	−12.5	2.2	4585	212	2.46	0.59	0.00	0.10	305.01	13.34	217.5604	29.3067	224.2299	4.92	−43.95	11.33
139076	5.3	4.4	4396	236	2.63	0.81	0.42	0.19	254.07	10.53	217.7726	10.6596	186.0135	−13.56	21.20	10.58
139136	102.4	1.4	4228	189	1.16	0.77	−0.71	0.25	1458.54	94.03	276.1727	41.9980	267.5426	−15.72	−195.8	181.77
139802	−48.9	2.8	4770	239	3.17	0.72	−0.04	0.14	226.72	7.83	168.1500	26.5403	157.6235	3.08	−51.46	−40.33
140347	24.4	3.0	4628	238	3.42	0.57	0.08	0.18	340.00	18.01	296.2877	26.1032	246.0249	−60.28	−76.99	−5.76
143876	−46.4	2.0	4702	298	2.77	0.84	0.00	0.10	226.96	8.88	212.0824	33.0440	154.2195	36.21	−19.94	−2.17
144518	−42.4	7.5	4936	251	3.21	0.75	−0.16	0.23	268.57	10.51	231.3098	44.6303	170.1536	34.56	−5.20	−0.41
146048	−25.6	3.6	4292	136	1.91	1.04	0.16	0.23	1453.47	73.63	321.2987	80.1094	233.3573	73.11	46.33	65.03
146231	−31.4	0.9	4875	296	2.96	0.38	0.17	0.24	211.67	8.29	181.6224	38.5891	124.0446	17.22	3.53	−7.17
146364	−28.6	3.9	4523	190	2.20	0.74	0.04	0.13	371.75	18.83	302.1812	86.0141	225.1008	13.02	−25.78	3.02
147116	−76.3	4.2	4023	190	0.85	0.82	−0.29	0.38	1322.20	76.11	289.5598	77.0556	201.7003	25.16	−89.23	−40.70
147293	15.6	3.7	4581	212	2.92	0.60	0.08	0.19	237.17	10.38	197.9545	50.1700	133.7229	−28.52	20.34	4.73
148425	−19.9	1.0	4208	170	1.16	0.83	0.04	0.14	1145.65	60.67	245.7210	75.0733	164.7186	−104.24	−53.74	−140.78
148981	26.2	7.3	4190	177	1.92	0.78	−0.08	0.18	881.86	42.64	196.7558	53.6145	120.5581	−20.25	34.73	31.38
149180	−11.1	8.1	4701	200	3.12	0.62	0.00	0.10	367.76	21.17	357.2683	88.5526	207.8295	6.48	9.11	13.72
149755	−3.3	3.3	4954	224	2.49	0.64	−0.37	0.22	300.70	12.46	252.7211	82.2633	157.4294	−13.70	−26.40	14.30
152583	−24.8	1.3	4953	264	2.80	0.72	−0.13	0.22	321.19	14.05	249.9098	89.2303	131.8209	19.80	3.29	13.14
152582	−3.8	3.5	4874	216	2.92	0.57	0.34	0.23	281.92	11.04	279.0848	103.5479	150.1501	−34.04	−37.33	−12.62
152898	−14.4	3.2	4269	215	2.86	0.61	0.04	0.14	207.11	7.15	185.1073	68.1235	96.7603	−10.22	−13.36	−8.80
156656	37.6	6.6	4875	238	3.25	0.56	0.12	0.22	267.73	9.25	265.6728	111.7550	110.5643	−63.20	−28.67	24.40
156669	−31.3	8.6	4936	249	2.83	0.62	−0.50	0.10	306.07	13.39	323.8501	133.8194	132.7162	−3.39	−52.73	−0.81
157415	−54.2	1.9	4788	221	2.59	0.61	−0.08	0.18	204.71	7.07	194.1648	83.3166	76.7685	42.57	3.58	−10.53
158333	−0.1	1.0	4790	282	2.72	0.74	0.13	0.22	269.35	9.92	238.8960	119.1940	97.4226	−13.83	−5.04	17.11

Table 9.4: Continues

Name	V_{rad}	E_{Vrad}	T_{eff}	E_{Teff}	$\log g$	$E_{\log g}$	[M/H]	$E_{[M/H]}$	D_{pho}	E_{Dpho}	Gal_X	Gal_Y	Gal_Z	U_{vel}	V_{vel}	W_{vel}
HD	kms^{-1}	kms^{-1}	K	K	dex	dex	dex	dex	pc	pc	pc	pc	pc	kms^{-1}	kms^{-1}	kms^{-1}
194164	−99.7	2.1	4209	134	2.39	0.66	0.00	0.10	206.84	6.67	146.9507	139.2026	−76.8139	71.28	−59.58	4.78
198347	−11.0	1.2	4892	236	2.72	0.69	0.00	0.10	397.18	18.29	251.7580	277.1620	−181.7185	5.68	12.06	12.25
202395	−40.7	5.1	5023	215	3.29	0.65	0.00	0.10	278.48	11.54	152.4126	188.2595	−149.6090	25.78	−9.82	21.97
202464	−23.4	2.5	4810	287	2.87	0.61	−0.08	0.19	378.52	22.66	195.3202	278.2055	−193.2167	23.24	2.55	8.74
204776	−29.6	4.5	4683	207	2.55	0.66	0.00	0.10	256.76	9.46	125.1270	187.1173	−148.1912	−10.37	−23.67	17.54
204980	25.3	4.8	4935	250	3.04	0.68	−0.08	0.18	330.41	15.22	150.2296	237.3398	−181.8187	−2.89	29.68	−20.88
205225	1.5	2.3	4665	252	2.21	0.66	−0.37	0.42	299.53	13.79	143.7901	201.7457	−175.3149	1.55	20.65	6.21
208279	10.9	3.3	4293	169	2.49	0.61	0.00	0.10	306.48	15.52	124.9527	226.2358	−201.9609	2.14	20.63	−7.25
208919	−29.5	1.7	4400	158	2.13	0.76	−0.08	0.18	344.29	22.99	123.2583	250.6297	−215.3820	54.81	−8.87	−4.74
209247	5.7	4.3	4767	257	2.59	0.67	−0.04	0.14	397.91	22.90	159.0331	266.1569	−272.3789	−57.18	12.29	27.34
209321	−26.4	6.3	4396	234	2.74	0.75	0.33	0.24	215.38	7.93	89.5068	146.8211	−153.6505	27.15	−0.76	13.91
210185	−10.4	2.0	4378	159	1.68	0.66	−0.12	0.22	849.89	31.31	80.1528	145.9663	−151.1601	−2.10	−47.84	−38.36
213999	27.9	5.0	4416	184	2.86	0.65	0.04	0.14	253.14	10.49	73.4774	153.5497	−195.9993	−22.80	11.84	−24.32
215861	0.3	4.6	4979	238	3.12	0.68	−0.12	0.22	402.09	24.07	48.6897	175.1028	−194.3644	−40.13	22.44	24.61
215851	24.1	5.2	4812	269	2.93	0.80	−0.38	0.21	262.23	9.06	88.6214	268.7529	−324.1546	0.34	50.33	4.96
216230	−20.8	3.5	4794	224	3.17	0.47	−0.50	0.10	322.07	11.87	62.2122	219.6280	−256.1461	−68.27	−17.48	24.76
217876	−23.1	2.1	4710	200	2.96	0.63	0.13	0.22	266.85	11.67	37.3347	169.4103	−210.6672	−10.77	−15.08	16.25
219818	11.4	2.0	4793	223	2.42	0.64	−0.46	0.14	408.53	19.75	54.1260	186.0180	−320.2626	22.65	25.56	−3.21
224278	16.8	2.4	4748	225	2.84	0.75	−0.08	0.18	334.80	14.65	−17.4461	172.5562	−285.2059	93.23	7.73	−8.16
225059	5.2	1.8	4296	171	2.58	0.57	0.00	0.10	260.04	9.58	−15.3025	124.5426	−229.2000	1.65	−13.14	−11.10

Name	V_{rad}	E_{Vrad}	T_{eff}	E_{Teff}	$\log g$	$E_{\log g}$	[M/H]	$E_{[M/H]}$	D_{pho}	E_{Dpho}	Gal_X	Gal_Y	Gal_Z	U_{vel}	V_{vel}	W_{vel}
HD	kms^{-1}	kms^{-1}	K	K	dex	dex	dex	dex	pc	pc	pc	pc	pc	kms^{-1}	kms^{-1}	kms^{-1}
127	−19.5	1.3	4727	216	3.12	0.36	0.00	0.10	271.79	9.39	−22.0967	134.8304	−243.0266	−1.90	−13.23	14.66
342	−16.5	2.3	4729	188	2.96	0.56	0.00	0.10	271.97	10.02	−34.5634	147.1733	−226.4789	−78.71	−7.89	4.49
1644	−14.6	1.3	4479	121	2.00	0.58	−0.04	0.13	261.85	9.65	−42.1611	128.7721	−221.4325	26.17	−7.30	21.70
2236	04.6	1.0	5035	247	3.38	0.54	0.00	0.10	318.45	14.67	−52.0395	144.4890	−277.7725	−32.08	14.66	−0.66
2690	−05.7	0.4	4544	224	2.38	0.65	0.17	0.24	310.17	15.00	−60.7801	145.3060	−264.0988	14.16	−4.52	9.89
3915	−34.2	0.7	4704	245	2.50	0.65	0.00	0.10	375.49	18.16	−90.5307	168.6658	−320.3659	−24.63	−8.98	32.70
16061	00.2	3.7	5187	252	3.46	0.48	−0.20	0.25	346.70	15.17	−189.8449	44.0760	−242.1009	−7.91	8.05	8.01
20055	17.6	2.8	4356	213	2.75	0.80	0.38	0.22	273.34	12.59	−220.4326	4.5574	−224.1340	−14.35	−41.27	−14.16
25542	33.0	7.6	4751	268	2.72	0.59	0.00	0.10	242.32	8.93	−212.6431	−49.2943	−169.8839	30.50	−12.45	3.77
25980	19.1	2.8	4836	275	2.68	0.68	0.04	0.14	297.35	10.95	−258.1564	−60.3637	−199.3399	9.41	−15.38	6.68
26065	41.9	4.2	4497	179	2.75	0.55	0.04	0.14	256.45	11.22	−296.7043	−45.1075	−203.1394	11.47	−33.27	−26.39
26373	26.7	5.2	4931	250	2.53	0.59	−0.08	0.18	225.45	7.27	−225.7322	−41.6182	−157.0112	−0.75	5.20	−30.06
27351	−4.4	1.9	5066	252	3.00	0.67	−0.21	0.25	232.39	8.56	−185.6369	−46.8727	−128.3438	−21.17	10.22	−0.81
28956	29.7	4.5	4977	238	3.00	0.54	0.00	0.10	362.47	20.86	−328.8731	−80.9178	−189.5163	−3.74	13.97	16.05
29913	13.7	2.7	4689	209	2.43	0.64	0.00	0.10	237.20	8.74	−219.4004	−48.4379	−108.2479	−3.84	−18.20	−5.54
29914	−03.3	2.8	5020	238	2.84	0.59	−0.12	0.22	217.44	8.01	−202.6439	−52.9193	−106.5832	−13.42	12.10	4.08
30356	−12.4	1.1	4355	123	2.04	0.63	0.00	0.10	290.93	12.06	−260.8050	−79.4191	−139.3979	−56.71	−25.44	−16.41
30618	−27.7	0.7	4936	271	2.95	0.59	−0.12	0.22	290.51	11.37	−258.4015	−68.1168	−125.6617	−24.11	11.68	42.89
77858	19.4	3.1	5019	259	2.88	0.61	−0.04	0.14	314.76	14.49	−183.0258	−208.0072	159.1063	−3.55	−17.88	7.97
105323	−02.6	3.9	4896	257	2.16	0.77	−0.50	0.10	1717.47	114.68	34.6151	−208.6654	390.6074	184.57	−245.50	−111.13
105587	00.3	1.9	4689	231	3.13	0.36	0.04	0.14	324.46	13.45	20.6168	−139.5996	288.7644	10.44	14.72	12.54
106316	−03.6	5.1	4687	287	3.25	0.63	0.08	0.19	237.99	8.22	26.6413	−111.8590	205.7481	31.01	2.70	4.53
106695	28.3	7.4	4791	282	1.71	0.74	−0.46	0.14	264.19	9.12	40.9354	−137.7628	223.8341	2.87	−45.60	8.55
111940	01.4	1.1	5020	258	3.21	0.69	0.00	0.10	368.40	16.12	82.4205	−123.2216	317.7163	−0.57	8.83	6.68
113641	15.1	1.2	4871	259	2.46	0.66	0.00	0.10	404.58	20.49	123.3543	−146.2231	352.5390	−19.25	1.99	18.40

Table 9.5: Continues

Name HD	V_{rad} kms^{-1}	E_{Vrad} kms^{-1}	T_{eff} K	E_{Teff} K	$\log g$ dex	$E_{\log g}$ dex	[M/H] dex	$E_{[M/H]}$ dex	D_{pho} pc	E_{Dpho} pc	Gal_X pc	Gal_Y pc	Gal_Z pc	U_{vel} kms^{-1}	V_{vel} kms^{-1}	W_{vel} kms^{-1}
115724	−14.7	0.6	4515	189	2.50	0.79	−0.12	0.21	337.31	14.76	120.2774	−111.5069	293.9373	83.84	−131.20	−28.99
118390	0.8	1.3	4852	257	2.35	0.82	0.00	0.10	296.57	12.29	124.1020	−84.4974	255.7938	−30.11	11.66	−0.40
119373	−14.9	3.8	4813	271	2.46	0.77	0.00	0.10	893.05	30.84	106.1461	−67.1337	200.2774	224.16	−173.95	54.52
120967	−04.8	0.8	4813	270	2.79	0.56	0.00	0.10	258.19	9.51	118.1083	−55.9650	225.2255	19.79	7.65	13.29
123324	−48.3	1.3	4227	123	1.79	0.51	0.00	0.10	943.55	32.59	122.9185	−42.9419	209.7776	−13.33	−229.07	−101.95
124069	−21.3	2.7	4891	255	2.82	0.63	−0.12	0.21	269.34	9.92	132.3042	−40.1240	221.8459	14.19	8.73	−5.80
125978	45.3	1.6	4834	235	2.33	0.71	−0.38	0.22	285.17	11.82	149.6529	−26.9357	243.2901	−88.05	−4.37	13.59
127414	−08.9	1.8	4415	155	2.83	0.84	0.12	0.21	323.63	14.16	182.7527	−23.9554	277.8186	−30.95	−34.19	−25.15
127988	−99.9	2.3	4186	147	1.67	0.68	0.00	0.10	308.97	14.23	180.3669	−27.3675	256.4271	76.96	−29.83	−59.48
133987	−25.5	3.3	4685	230	2.79	0.85	0.00	0.10	231.30	9.05	158.7201	−3.0531	173.6799	15.40	13.59	−12.52
137929	−12.1	1.9	4645	214	2.58	0.64	0.00	0.10	305.01	13.34	217.5604	29.3067	224.2299	4.92	−43.95	11.33
139136	104.3	2.3	4165	118	1.46	0.38	0.00	0.10	1458.54	94.03	276.1727	41.9980	267.5426	−15.72	−195.80	181.77
139802	−49.8	1.8	4668	236	2.42	0.53	0.00	0.10	226.72	7.83	168.1500	26.5403	157.6235	3.08	−51.46	−40.33
146231	−35.4	4.8	4873	295	2.59	0.81	0.17	0.24	211.67	8.29	181.6224	38.5891	124.0446	17.22	3.53	−7.17
147293	15.7	3.6	4499	203	2.96	0.47	0.17	0.24	237.17	10.38	197.9545	50.1700	133.7229	−28.52	20.34	4.73
149755	01.9	1.7	4873	328	2.83	0.66	−0.04	0.14	300.70	12.46	252.7211	82.2633	157.4294	−13.70	−26.40	14.30
152583	−27.5	0.5	4893	294	3.33	0.59	−0.04	0.24	281.92	11.04	249.9098	89.2303	131.8209	−34.04	−37.33	−12.62
152582	−01.5	1.3	4935	253	3.18	0.55	0.30	0.25	321.19	14.05	279.0848	103.5479	150.1501	19.80	3.29	13.14
156669	−33.1	1.4	4729	278	2.80	0.77	−0.17	0.24	306.07	13.39	323.8501	133.8194	132.7162	−3.39	−52.73	−0.81
194164	−97.0	1.3	4230	67.	2.24	0.55	0.00	0.10	206.84	6.67	146.9507	139.2026	−76.8139	71.28	−59.58	4.78
202395	−40.9	3.1	5087	185	3.13	0.54	0.04	0.14	278.48	11.54	152.4126	188.2595	−149.6090	25.78	−9.82	21.97
202464	−23.4	1.0	4871	214	2.91	0.45	−0.21	0.25	378.52	22.66	195.3202	278.2055	−193.2167	23.24	2.55	8.74
204776	−31.8	2.1	4471	190	2.22	0.85	0.04	0.14	256.76	9.46	125.1270	187.1173	−148.1912	−10.37	−23.67	17.54
204980	21.2	3.6	4957	265	3.00	0.67	0.00	0.10	330.41	15.22	150.2296	237.3398	−181.8187	−2.89	29.68	−20.88
205225	2.9	3.5	4629	160	2.05	0.87	−0.54	0.43	299.53	13.79	143.7901	201.7457	−175.3149	1.55	20.65	6.21

Table 9.5: Continues

Name HD	V_{rad} kms^{-1}	E_{Vrad} kms^{-1}	T_{eff} K	E_{Teff} K	$\log g$ dex	$E_{\log g}$ dex	[M/H] dex	$E_{[M/H]}$ dex	D_{pho} pc	E_{Dpho} pc	Gal_X pc	Gal_Y pc	Gal_Z pc	U_{vel} kms^{-1}	V_{vel} kms^{-1}	W_{vel} kms^{-1}
208279	12.6	1.3	4352	123	2.47	0.56	0.00	0.10	306.48	15.52	124.9527	226.2358	−201.9609	2.14	20.63	6.21
208919	−29.9	0.9	4460	91	2.00	0.61	0.00	0.10	344.29	22.99	123.2583	250.6297	−215.3820	54.81	−8.87	−7.25
210185	−12.5	1.0	4399	122	2.12	0.68	−0.12	0.21	849.89	31.31	80.1528	145.9663	−151.1601	−2.10	−47.84	−4.74
213999	28.1	1.3	4457	170	2.72	0.66	0.04	0.14	253.14	10.49	73.4774	153.5497	−195.9993	−22.80	11.84	−38.36
215861	−3.3	2.9	4917	235	3.34	0.62	0.00	0.10	262.23	9.06	48.6897	175.1028	−194.3644	0.34	50.33	−24.32
215851	25.1	4.1	4771	276	3.04	0.74	−0.21	0.25	402.09	24.07	88.6214	268.7529	−324.1546	−40.13	22.44	4.96
216230	−20.8	3.5	4793	224	3.17	0.47	−0.50	0.10	322.07	11.87	62.2122	219.6280	−256.1461	−68.27	−17.48	24.61
217876	−22.5	0.5	4748	203	2.88	0.61	0.17	0.24	266.85	11.67	37.3347	169.4103	−210.6672	−10.77	−15.08	24.76
224278	15.4	0.7	4648	122	2.98	0.50	−0.17	0.24	334.80	14.65	−17.4461	172.5562	−285.2059	93.23	7.73	16.25
225059	05.0	0.8	4396	123	2.45	0.56	0.00	0.10	260.04	9.58	−15.3025	124.5426	−229.2000	1.65	−13.14	−8.16
−11.10																

Chapter 10

The Catalog Stars As Solar Vicinity Tracers

The kinematics of stars near the Sun has long been known to provide crucial information regarding both the structure and evolution of the Milky Way (Dehnen & Binney, 1998). Thus, our survey of intermediate-galactic latitude (Fig. 10.1) Red Clump stars located d $\sim$ 200-470 pc and Z $\sim$ $-$430-430 pc can be used to study the kinematics and structure of Solar Neighborhood.

In this section, we investigated our observed Red Clump stars in terms of, first relations among their parameters and second their kinematic properties.

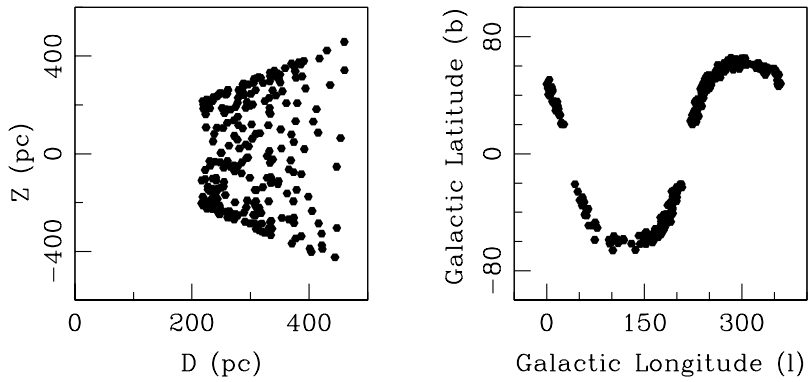

Figure 10.1: Positional properties of observed Red Clump stars

10.1 Atmospheric Parameters Of Red Clump Stars As A Function Of Spectral Type and Metallicity

Our large sample allows to investigate the statistical properties of stars. Here we explore the atmospheric parameters of our target stars as a function of their spectral type and metallicity to find out possible relations.

In Fig. 10.2, we plotted the derived T_{eff}, $\log g$ and [M/H] of 245 Red Clump stars as a function of spectral type (left panel) and the U,V and W space velocities as a function of spectral type (right panel). As it can be seen, there are no trends on parameters according to the spectral type apart from a very slight relation for [M/H] : late type (later than K2) Red Clump stars are seen to have higher metallicities, [M/H] $\geq$ 0.0 dex, while the early type ($\geq$ G9) have lower metallicities, [M/H] $\leq$0.0.

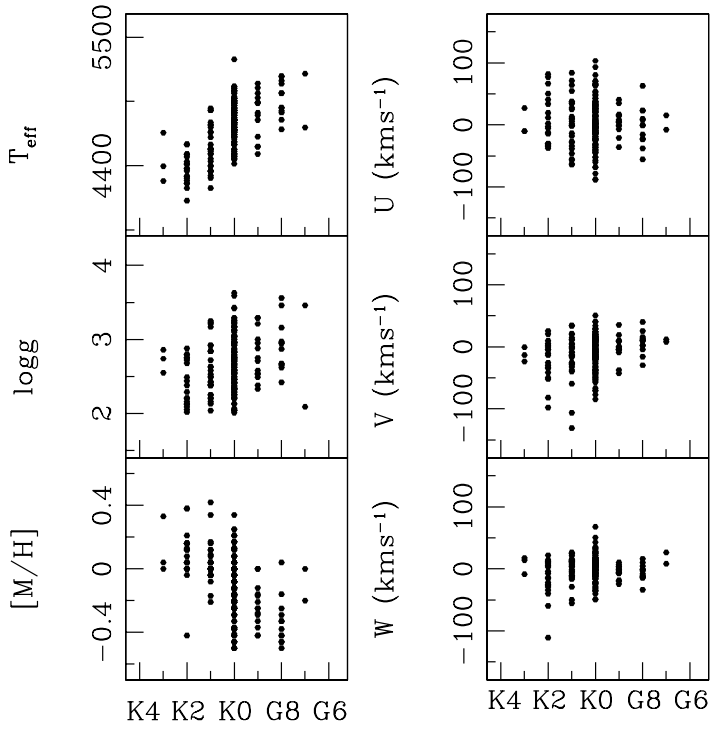

Figure 10.2: T_{eff}, log$g$, [M/H] and U,V,W space velocities as a function of spectral type.

In Fig. 10.3, we shown the T_{eff} - $\log g$ plane of our observed Red Clump stars as a function of their spectral types. It is seen that, as expected, the late-type stars with low-temperature and earlier types with higher temperatures are well separated, while for the K0 type stars the temperature interval is much more wider.

In Fig. 10.4, we plot the T_{eff} - $\log g$ plane of the observed targets as a function of the stellar metallicities. The stars have metallicities in the range $-0.5 \leq$ [M/H] $\leq +0.2$ dex. A few stars are in the metal rich tail of the distribution, with metallicities $+0.2 \leq$ [M/H] $\leq +0.5$ dex.

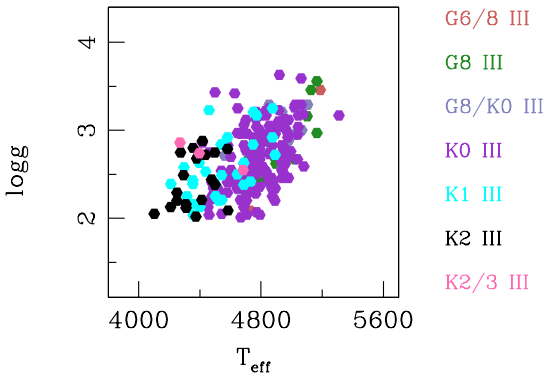

Figure 10.3: T_{eff} - $\log g$ plane plotted as a function of spectral type.

The stars show no trend of their properties with the metallicity.

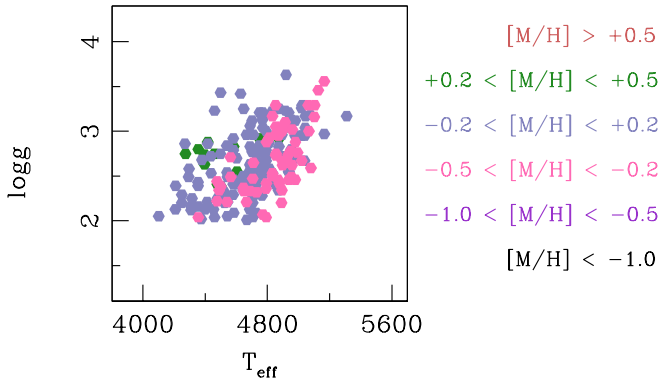

Figure 10.4: T_{eff} - $\log g$ plane plotted as a function of the metallicity.

10.2 The Milky Way

With increasingly detailed studies, nowadays it is clear that the Milky Way is composed by several different stellar populations. In the past these populations were viewed as a *continous* sequence, according to the idea that the Milky Way formed from the coherent collapse of a slowly-rotating gas cloud (Eggen et al. 1962). Thus the oldest population (Pop II.) stars were taken to define a nearly-spherical and slowly-rotating halo, while younger population (Pop I.) stars defined flatter and more rapidly rotating distributions, blending smoothly to disk.

The idea of *continuous* transition between these populations, although not that simple, has come under considerable revision in the light of new evidences. The realization that the central bulge is metal rich challenges the one-dimensional taxonomy of traditional stellar populations. At present the Galaxy is thought to contain three main luminous

populations: the *thin disk* (young, Pop.I stars), the *thick disk* (intermediate Pop II. stars) and the *stellar halo* (old, Pop II. stars).

Those stellar populations are characterized by a distinct spatial distribution, kinematics and metal content that proved to be a key concept in interpreting the observations of our own Galaxy.

- **Thin Disk :** The thin disk of the Milky Way has sustained ongoing star formation for $\sim 10^{10}$ years. Consequently it containes stars with a wide range of ages ($0 - 10\ Gyr$). The thin disk is divided into a series of sub-populations of increasing age:

  1.The Spiral-Arm Population is the youngest in the disk; it appears to trace the spiral pattern of the Milky Way. This population is concentrated very close to the disk plane, with a scale height of $\sim 100\ pc$. Representative objects include H I and molecular clouds, H II regions, protostars, O & B stars, supergiants, classical cepheids. The metallicity of this population is $[Fe/H] \geq 0.00$.

  2.The old Disk Population is more smoothly distributed. This population may be further sub-divided into young ($\sim 1\ Gyr$), intermediate ($\sim 5\ Gyr$) and older ($\sim 10\ Gyr$) categories. The scale height of this population is up to $\sim 300\ pc$, while the metallicity is $-0.7 \leq [Fe/H] \leq 0.5$.

- **Thick Disk :** The thick disk of the Milky Way is an intermediate population that is distributed in a tickened disk with a scale height $\sim 700\ pc$ up to $\sim 1500\ pc$. This population accounts for only $\sim 1\%$ of the stars in the vicinity of the sun but dominates at higher latitude ($z > 1\ kpc$). The true nature of this population is still not completely clear, although it is older than thin disk population. Kinematic studies imply that the thick disk rotates with a velocity of $\sim 180\ kms^{-1}$. This would indicate that the thick disk is more closely associated with the thin disk population, which rotates $\sim 220\ kms^{-1}$ than with the halo. The metallicity of the thick disk population is $-1.7 \leq [Fe/H] \leq -0.6$.

- **Stellar Halo :** The stellar halo of the Milky Way includes the systems of globular clusters, metal-poor-high-velocity stars in the solar neighborhood and the metal-rich dwarf stars seen toward the galactic center. The stars formation in the outer halo largely ceased more than 10^{10} years ago, while the situation in the inner kpc of the Galaxy is still not so clear.

10.2.1 Milky Way Kinematics Traced By Red Clump Giants

Disk kinematics can be examined in detailed with a typical analysis of the U,V,W space velocity distribution of the stars. Thus, some irregularities can come out as over concentrations of the stars in U-V space velocity plane as moving groups and/or stellar streams.

We calculated the U,V,W space velocities as described in detailed in Chapter 6. Fig. 10.5 shows the distribution of the space velocities for our target stars with respect to the sun. The typical mean velocities are $< U, V, W > = < 3.2, -8.3, 0.2 >$ kms^{-1} with a dispersion of $(\sigma_U, \sigma_V, \sigma_W) = (35, 27, 20)$ kms^{-1}. We obtained the classical ordering for the velocity dispersion components: $\sigma_U > \sigma_V > \sigma_W$. These values are also very well correlated with the values derived by Valentini & Munari (2010) and by Famey et al. (2004).

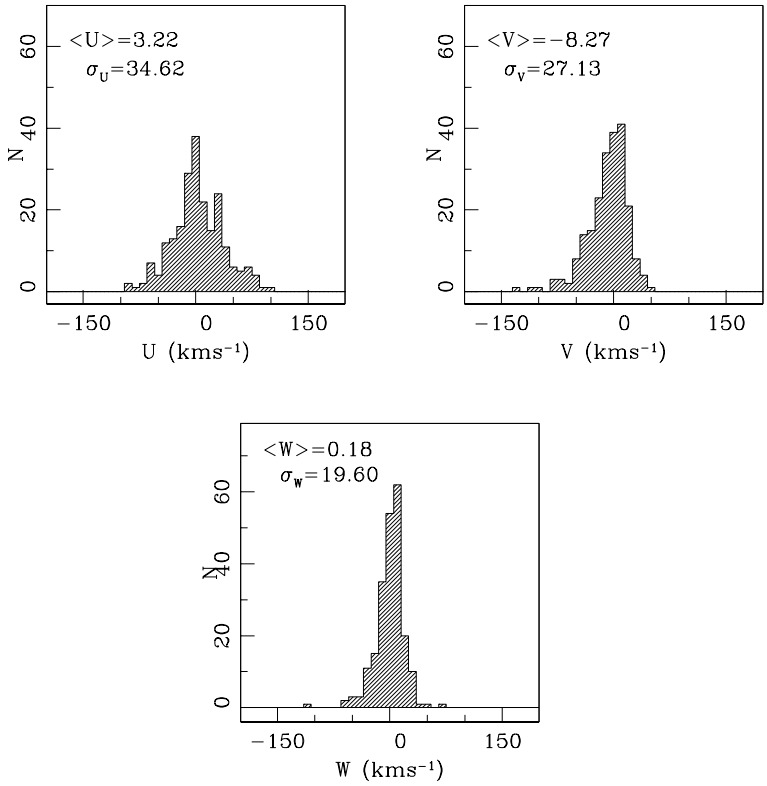

Figure 10.5: The (U, V, W) space velocity distribution of the 245 Red Clump stars.

In Fig. 10.6, we plot the UVW space velocities of the stars as a function of metallicity ([M/H]) and in Fig. 10.7, we plot the U-V, V-W and W-U space velocity planes as a function of the metallicity. We aimed to see possible metallicity trends among the space velocity of Red Clump stars. The lack of metallicity trends is well visible.

In Fig. 10.8 and Fig. 10.9, we plot again U-V, W-V and W-U space velocity planes this time with color separation based on surface gravities and spectral types, respectively. No trends of the properties with the metallicity are found.

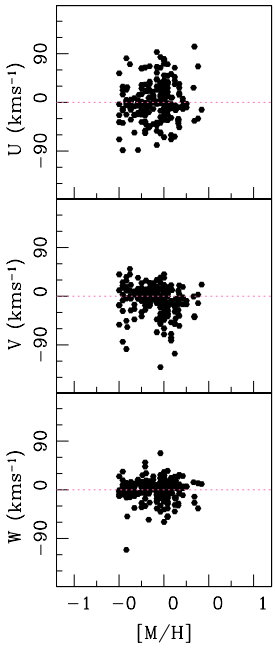

Figure 10.6: The (U, V, W) space velocities as a function of metallicity [M/H].

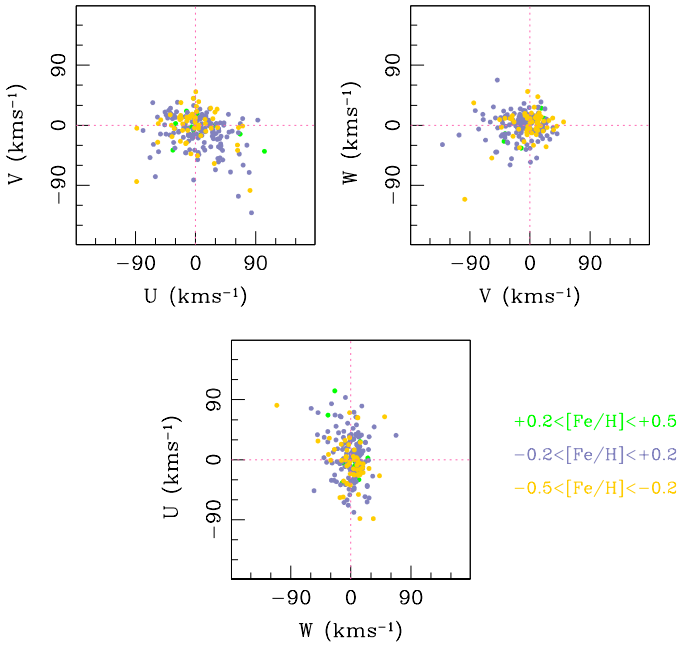

Figure 10.7: The (U, V, W) space velocities as a function of metallicity [M/H].

10.2.2 Moving Groups

It is known for a long time that spatially unbound groups of stars in the Solar Neighborhood share the same kinematics (Eggen 1996). Assuming that they are vestiges of more

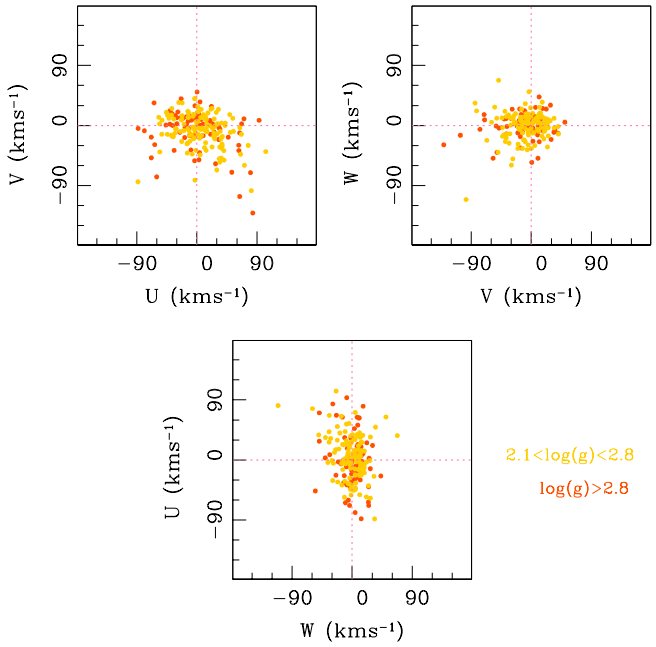

Figure 10.8: The (U, V, W) space velocities as a function of gravity ($\log g$).

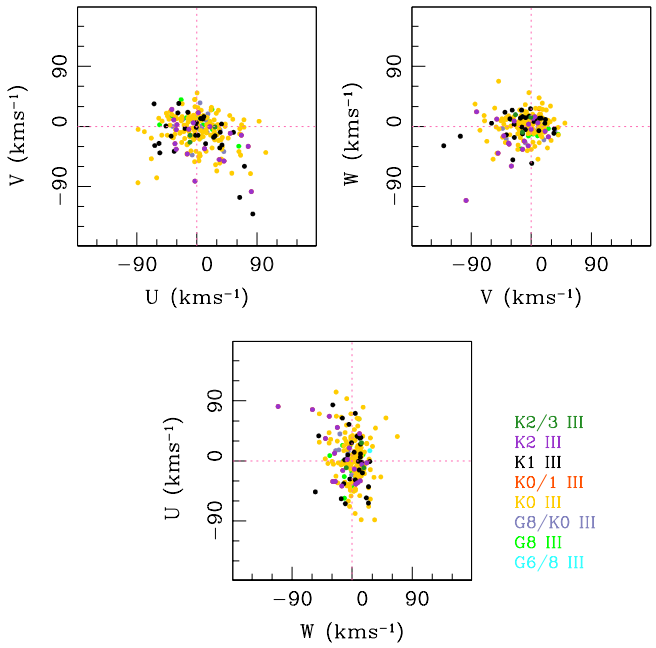

Figure 10.9: The (U, V, W) space velocities as a function of spectral type.

massive primordial clusters which partly evaporated with time, those kinematically cold groups are generally called *superclusters* (i.e. Hyades and Sirius), or also called *streams*

and moving groups. They are noticeable in the U-V velocity plane with: the peak at (U,V) = (9,3) kms^{-1} corresponds to the Sirius stream, that at (−12,−22) kms^{-1} to the Pleiades stream and that at (−35,−18) kms^{-1} corresponds to the Hyades stream.

To be able to define stars that are belonging streams from our sample, we used the same method by Skuljan et al. (1999). In their study, they analyzed the two dimensional velocity distribution in UV plane for 4597 stars selected from Hipparcos catalog. Among those stars, for 3561 late-type ones they derived the distribution of the stars in UV plane and defined the tilt of branches by rotating them counter-clockwise with an angle defined as β (Fig. 10.10).

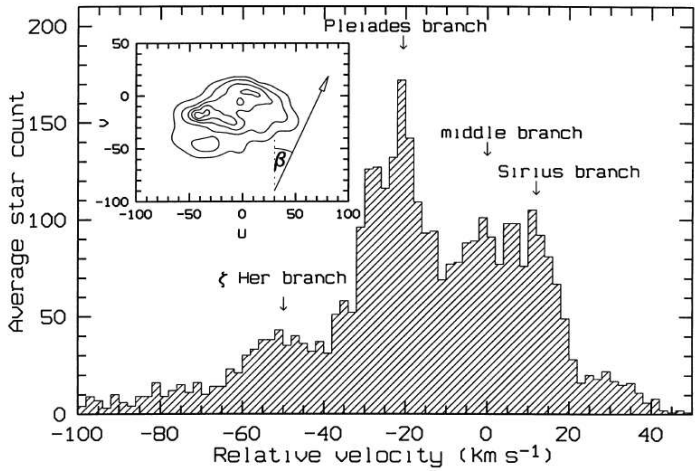

Figure 10.10: The relative U velocity and average star counts to define streams, taken from Skuljan et al. 1999.

In Fig. 10.11, we plotted our results obtained with a similar analysis of Skuljan et al. (1999). The inclination angle that they adopt for the late-type stars, is $\beta \sim 25°$ while in our case an angle of $\beta \sim 27°$ is more suitable. In a similar study, Antoja et al. (2008) find an inclination angle of $\beta \sim 16°$. The differences in β among those studies might be due to the different distance scale of the targets.

In Antoja et al. (2008) the mean metallicity of the branches is discussed, (see Tab. 10.1). We define three metallicity intervals for our stars, namely $+0.2 < [Fe/H] < +0.5$, $-0.2 < [Fe/H] < +0.2$ and $-0.5 < [Fe/H] < -0.2$. However, as evident in Fig. 10.12 the characteristic metallicity of the branches is still defined, since they span a wide range.

As mentioned by Skuljan et al. (1999), large errors in the parameters used for space velocity determination could lead to features in the kinematic U-V plane being artificially radially elongated (relative to the point (U,V) = (0,0)). The U-V space velocities for this three metallicity intervals are presented in Fig. 10.13 together with the mean U and V velocities for metallicity interval.

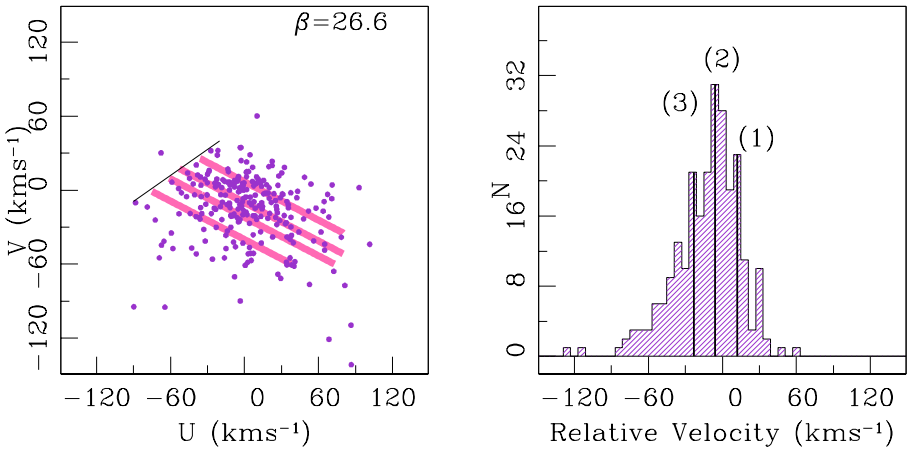

Figure 10.11: The relative U velocity and average star counts for defining streams traced by 245 Red Clump stars

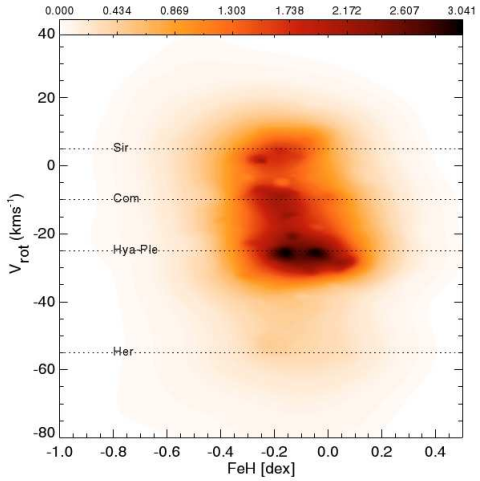

Figure 10.12: Density field in the V_{rot}-[Fe/H] plane from Antoja et al. 2008

To be able to confirm the stream membership of these stars, a detailed analysis of chemical elements is required (Freeman, 2010). However, this is possible only using higher resolution spectroscopy.

10.2.3 Star Kinematics

Soubiran et al. (2003) analyzed the space velocity components (U,V,W) and the related (σ_U,σ_V,σ_W) for stars having thin and thick disk metallicity (see Tab. 10.2). In Tab. 10.3, we give the results of mean (U,V,W) space velocity components and their (σ_U,σ_V,σ_W) values derived for three different [Fe/H] intervals.

Table 10.1: The mean metallicity of the branches

Branch	Antoja et al. (2008)		Helmi et al. (2006)	
	[Fe/H]	$\sigma_{[Fe/H]}$	[Fe/H]	$\sigma_{[Fe/H]}$
	dex	dex	dex	dex
Herculus	−0.15	0.27	−0.13	0.2
Hyades-Plaides	−0.11	0.20	−0.08	0.2
Coma Berenices	−0.16	0.22	...	...
Sirius	−0.21	0.21	−0.18	0.2

Table 10.2: Parameters of Thin and Thick Discs derived by Soubiran et al. (2003)

	[Fe/H]	$\sigma_{[Fe/H]}$	σ_U	σ_V	σ_W
	dex	dex	kms^{-1}	kms^{-1}	kms^{-1}
Thin Disc	−0.17	0.26	39	20	20
Thick Disc	−0.48	0.32	63	39	20

Table 10.3: The mean (U,V,W) velocities and σ_U,σ_V,σ_W) derived for different bins of [Fe/H]

Metallicity Interval	$< U >$ kms^{-1}	$< V >$ kms^{-1}	$< W >$ kms^{-1}	σ_U kms^{-1}	σ_V kms^{-1}	σ_W kms^{-1}
$+0.2 < [Fe/H] < +0.5$	8.25	−7.90	0.22	40.01	18.18	17.14
$-0.2 < [Fe/H] < +0.2$	6.30	−11.54	−0.32	34.17	27.44	18.76
$-0.5 < [Fe/H] < -0.2$	−3.13	−1.81	0.35	33.95	27.13	22.92

Thin disc and Thick disc stars have metallicities in the range [Fe/H] = +0.50 - −0.70 dex and [Fe/H] = −0.60 - −1.70 dex, respectively. Our samples stars have metallicities between [Fe/H] = +0.50 - −0.50, typical of the Thin Disc. As it is shown in Tab. 10.3, the values for (σ_U,σ_V,σ_W) are in agreement with those of Soubiran et al. (2003) for Thin Disc distribution and do not present significant differences at changing metallicity.

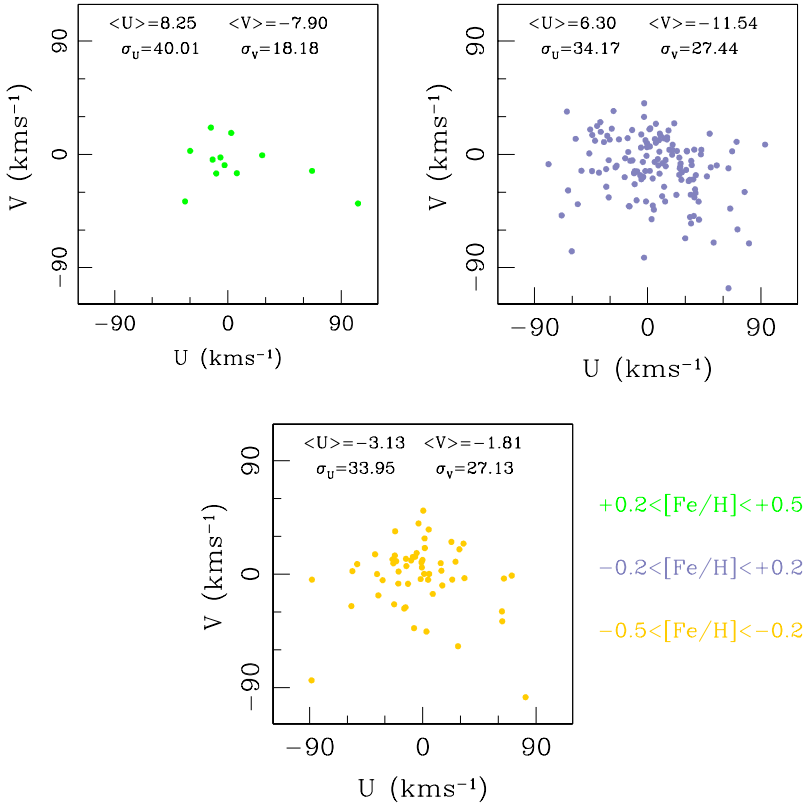

Figure 10.13: U-V space velocity plane of our observed stars plotted separately for three [M/H] bins. The mean (U,V,W) and σ(U,V,W) is derived for each metallicity bin.

10.2.4 Toomre Diagram

Toomre diagram is a representation of combined vertical and radial kinetic energies of stars' as a function of their rotational velocities. In Fig. 10.14, we plot our stars in a Toomre diagram and divided them into constant total space velocity bins, v_{tot} given as Eq. 10.1, with 50 kms^{-1} steps.

$$v_{tot} = \sqrt{U^2 + V^2 + W^2} \tag{10.1}$$

Bensby & Feltzing (2009) plot 899 nearby F and G dwarfs in a Toomre diagram. They considered low velocity stars, v_{tot} $\leq$ 50 kms^{-1} as thin disk stars and stars with 70 $\leq$ v_{tot} $\leq$ 200 kms^{-1}

as likely to be thick disc stars. Nissen (2004) studied a sample of 200 F and early G dwarfs in Toomre diagram. He considered stars with $v_{tot} \leq 85$ kms^{-1} to define thin disc sample and stars between $85 \leq v_{tot} \leq 180$ kms^{-1} to define thick disc sample.

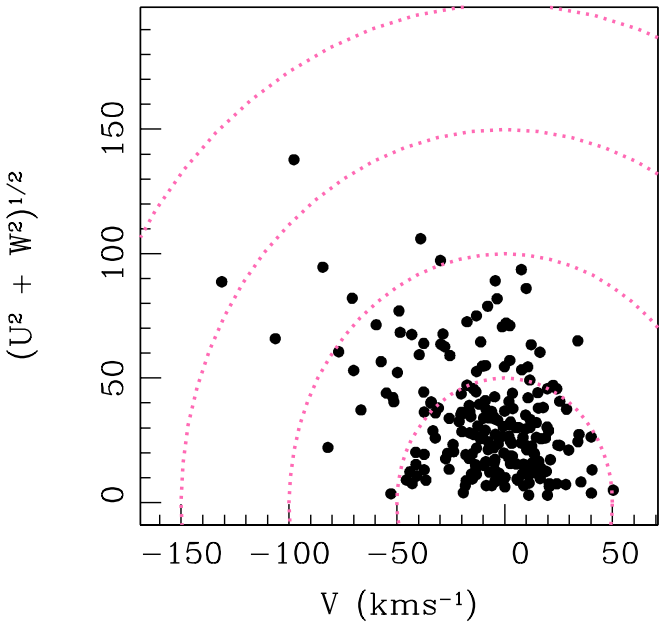

Figure 10.14: Toomre diagram of 245 observed Red Clump stars. The dotted lines show a constant space velocity with respect to LST in steps of 50 kms^{-1}

As seen in Fig. 10.14, most of our stars are lying in $v_{tot} \leq 80$ kms^{-1} with a few high velocity stars, $v_{tot} \geq 100$ kms^{-1}. Thus, if we assume Nissen (2004) kinematics, we are mostly looking at stars of the thin disk with a small contribution of stars of the thick disc.

10.2.5 Local Standard Of Rest

The Local Standard of Rest (LSR) is defined as the rest frame of a star at the location of the Sun that would be on a circular orbit in the gravitational potential of the Galaxy. Since the observations are relative to the Sun, which is surely not stationary, the kinematical parameters need to be corrected accordingly to the LSR motion.

The usual way to calculate the LSR is to calculate the mean velocity of the stellar population, and correct for asymmetric drift. The radial ($U_\odot$) and vertical ($W_\odot$) components of the Solar motion , as a function of stellar population, in principle can be obtained by direct analysis of the mean heliocentric velocities of Solar neighbourhood stars. However, the determination of the space velocity component in the direction of the Galactic rotation ($V_\odot$) is complicated by asymmetric drift with respect to the LSR, which depends on the velocity dispersion of the stellar sample. As it can be seen in Tab. 10.4, the derived values for $V_\odot$ differes a lot for the $U_\odot$ and $W_\odot$ from author to author. The values are in the

Table 10.4: Recent measurements of the LSR

Source	$U_\odot$ kms^{-1}	$V_\odot$ kms^{-1}	$W_\odot$ kms^{-1}
Binney (2010)	10.00±0.36	11.00	7.17±0.38
Coskunoglu et al. (2010)	8.50±0.29	13.38±0.43	6.49±0.26
Bobylev & Bajkova (2010)	5.5±2.2	11.0±1.7	8.5±1.2
Breddels et al. (2010)	12.0±0.6	20.4±0.5	7.8±0.3
Schonrich et al. (2010)	11.10±0.72	12.24±0.47	7.25±0.36
Francis & Anderson (2009)	7.5±1.0	13.5±0.3	6.8±0.1
Bobylev & Bajkova (2007)	8.7±0.5	6.2±2.2	7.2±0.8
Piskunov et al. (2006)	9.44±1.14	11.90±0.72	7.20±0.42
Fehrenbach et al. (2001)	8.24±0.6	11.58±0.6	5.97±1.1
Mignard (2000)	9.88	14.19	7.76
Dehnen & Binney (1998)	10.00±0.36	5.25±0.62	7.17±0.38
Binney et al. (1997)	11.00±0.6	5.3±1.7	7.0±0.6
Jaschek et al. (1991)	9.8	11.6	5.9
Mihalas & Binney (1981)	9.2±0.3	12.0	6.9±0.2

range 20 to 5 kms^{-1}.

With our 254 observed Red Clump stars in the Solar neighbourhood, we calculated the LSR in two ways: first we used all the sample without making a division of thin disk and thick disk population. The results are shown in Fig. 10.15. Using the second method, we defined the probability for a star of being member of a given population as introduced by Bensby et al. (2003, 2005). We considered just the stars which have high probability of being member of the thin disc population. The results are shown in Fig. 10.16.

Bensby et al. (2003) calculated the LSR by assuming that the Galactic space velocities of stellar populations with respect to the LSR have Gaussian distributions as follows:

$$f(U,V,W) \;=\; k \;\times\; EXP(\,-\,\frac{U_{LSR}^2}{2\sigma U_{LSR}^2} \;-\; \frac{(V_{LSR}-V_{asym})^2}{2\sigma V_{LSR}^2} \;-\; \frac{W_{LSR}^2}{2\sigma W_{LSR}^2}\,) \qquad (10.2)$$

where

$$k \;=\; \frac{1}{(2\pi)^{(3/2)}\sigma U_{LSR}^2 \sigma V_{LSR}^2 \sigma W_{LSR}^2} \qquad (10.3)$$

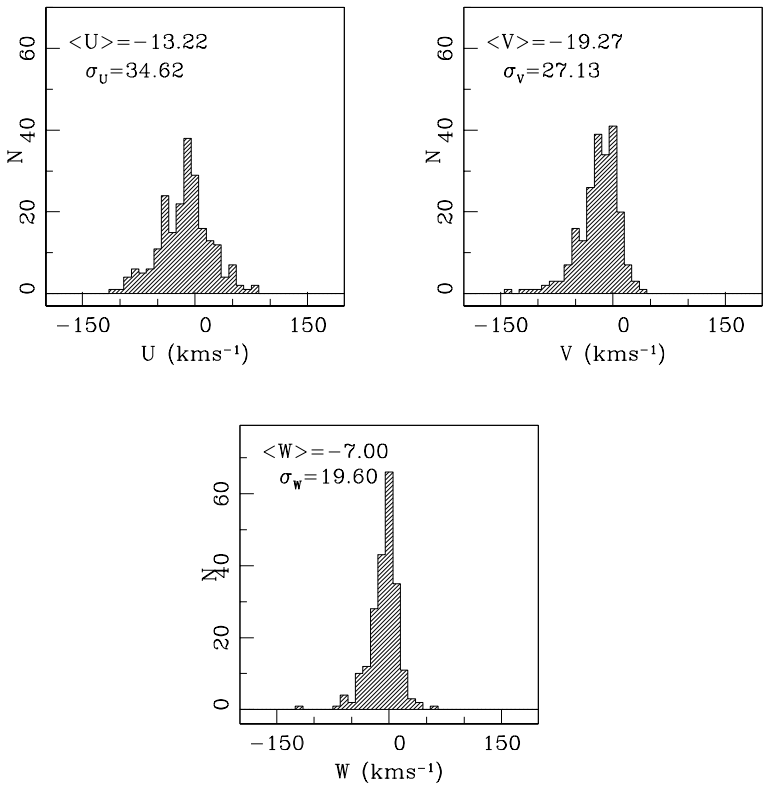

Figure 10.15: The distribution of the Galactic space velocities calculated for 245 observed Red Clump stars.

These values can be compared with the characteristic velocity dispersions (σU_{LSR},σV_{LSR},σW_{LSR}) and asymetric drifts in the thin disc, thick disc and halo derived by Bensby et al. (2003) and listed in Tab. 10.5.

Then the probability of a star to be member of a given population is defined at the ratio of the $f(U,V,W)$ distribution functions multiplied by the ratio of the local space densities for two populations. Thus:

$$\frac{TD}{D} = \frac{X_{TD}}{X_D}\frac{f(U.V.W)_{TD}}{f(U,V,W)_D} \qquad \frac{TD}{H} = \frac{X_{TD}}{X_H}\frac{f(U.V.W)_{TD}}{f(U,V,W)_H} \tag{10.4}$$

The values of X_D, X_{TD}, X_H are 0.94, 0.06 and 0.0015 respectively. Stars having TD/D $<$ 0.1 are defined as high probability thin disc stars, 0.1 $<$ TD/D $<$ 1 are defined as low probability thin disc stars, 1 $<$ TD/D $<$ 10 are low probability thick disc stars, and finally TD/D $>$ 10 are high probability thick disc stars.

We presented our determination of the LSR using both methods in Tab. 10.6. These results are in agreement with those by Breddels et al. (2010). When we apply a cut of limit to define thin disc as 0.1 $<$ TD/D $<$ 1, our results are in a good agreement (see

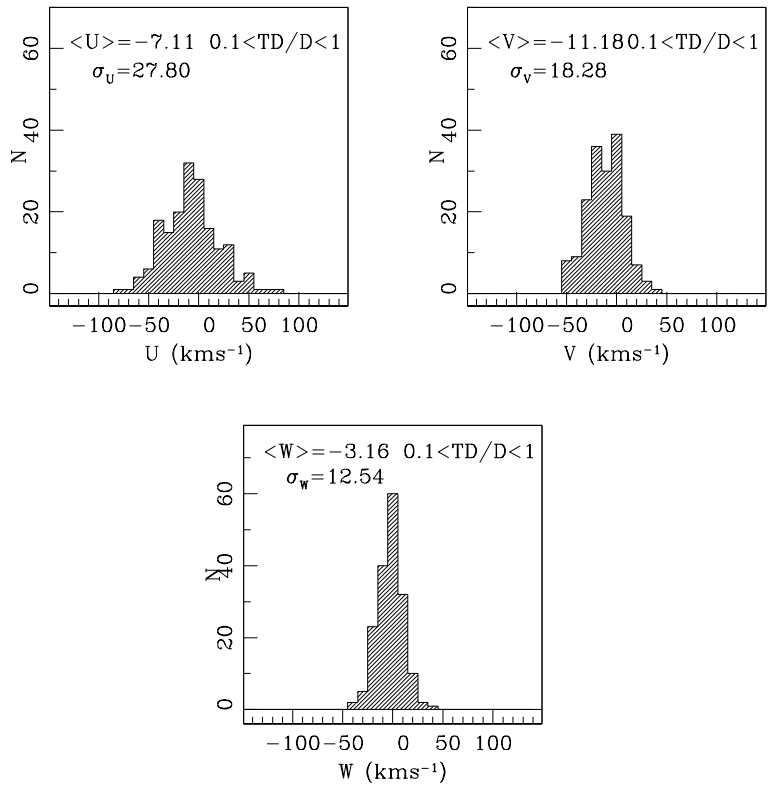

Figure 10.16: The distribution of the Galactic space velocities calculated for high probability thin disc stars.

Tab. 10.4) with both Fehrenbach et al. (2001) and Jascheck et al. (1991). These authors calculated the LSR motion using stars with D *leq* 195 pc. Our results are consistent with Coskunoglu et al. (2010) who apply the same method on RAVE data.

10.2.6 Milky Way Structure Traced By Red Clump Giants

Abundance gradients across the Galactic stellar disc provide fundamental constrains on the chemical evolution of the Galaxy components. In Fig. 10.17, we show the space velocity components and galactic height of our stars as a function of the metallicity. No metallicity gradient was found, neither in the radial direction, nor perpendicularly to the Galactic plane. This is not unexpected, due to the limited range of properties of the studied stars.

10.3 Age-Metallicity Relation

The age-metallicity relation (AMR) for nearby stars is a record of progressive chemical enrichment of the star-forming local interstellar medium during the evolution of the Galactic

Table 10.5: Velocity dispersions and asymetric drift values for thin disc, thick disc and stellar halo taken from Bensby et al. 2003.

	σU_{LSR} kms^{-1}	σV_{LSR} kms^{-1}	σW_{LSR} kms^{-1}	V_{asym} kms^{-1}
Thin Disc (D)	35	20	16	−15
Thick Disc (TD)	67	38	35	−46
Halo (H)	160	90	90	−220

Table 10.6: Recent measurements of the LSR

Source	$U_\odot$ kms^{-1}	$V_\odot$ kms^{-1}	$W_\odot$ kms^{-1}
All 245 observed stars	13.0	19.3	7.0
Stars with 0.1 < TD/D < 1	7.1	11.2	3.2

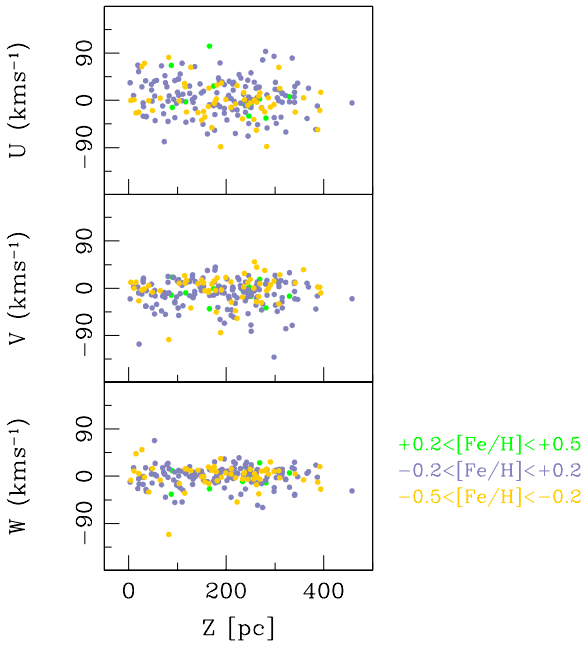

Figure 10.17: The distance versus Galactic scale height as a function of metallicity for observed Red Clump giants.

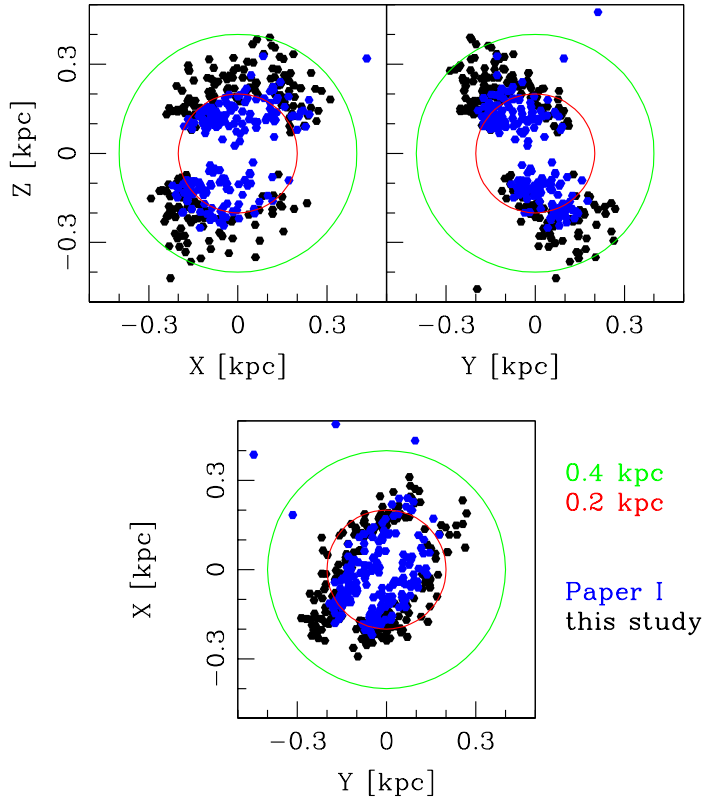

Figure 10.18: The comparison of Galactic (X, Y, Z) coordinates for Valentini & Munari, 2010 (blue dots) and this study (black dots). The red circle represents 0.2 *kpc* field and the green circle represents 0.4 *kpc* field.

disc. AMR provides useful clues about the star formation and chemical evolution history of the local environment.

Twarog (1980) first showed that nearby stars display an AMR, from *u,v,b,y-β* using Yale isochrones to obtain the metallicity and the age for two wide samples of stars. Since then, the AMR has been examined by many groups in the solar neighbourhood (i.e. Edvardsson et a., 1993; Ng & Bertelli, 1998; Ibukiyama & Arimato, 2002; Soubiran et al., 2008) and in open clusters (i.e. Friel & Janes, 1993; Carraro & Chiosi, 1994).

To trace the AMR in our sample, we use the PARAM code developed by L. Girardi (da Silvia et al., 2006). This code is based on a Bayesian estimation method and uses the theoretical isochrones by Girardi et al. (2000). PARAM uses the T_{eff}, V_{mag}, [Fe/H], π parallax information and their related errors as input data and estimates the probability that a star can belong to each small section of a theoretical isochrone of a given age and metallicity. Then those probabilities are summed over the isochrone by assuming a Gaussian probability distribution. With the assumption of a constant star formation rate and the possibility of selecting the IMF slope, the age probability distribution functions (PDF) is calculated.

Unfortunately, the errors in age estimation are mainly caused by the large uncertainties in individual distances of stars. Distances need to be known to a 5% accuracy to get reliable ages, as demonstrated in Carraro et al. (1998). When we ake use of the spectro-photometric distances for our stars, and we take into account the errors on the metallicity and temperature, the ages calculated by PARAM turn out to have large errors on age, $\sigma_{AGE}/AGE > 50\%$ (see Fig. 10.19). This prevent any firm conclusion on the AMR of the sample stars.

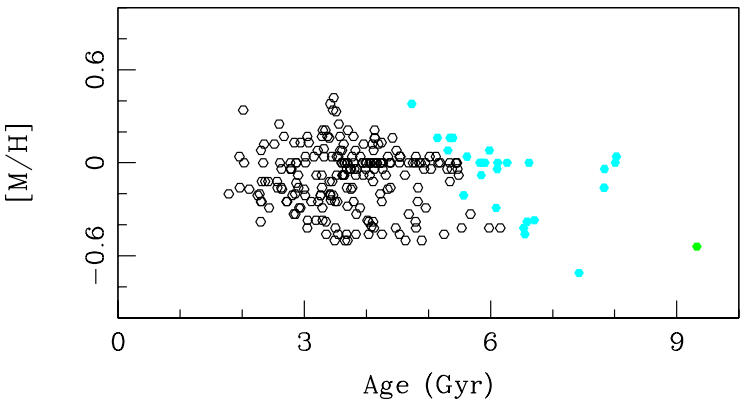

Figure 10.19: Age-Metallicity relation of target stars. The green dot represents $\sigma_{AGE}/AGE \geq 25\%$, the cyan dots represent $\sigma_{AGE}/AGE \geq 25\%$ and $\sigma_{AGE}/AGE < 50\%$, finally the black open circles represent stars with $\sigma_{AGE}/AGE > 50\%$

The Mass and the Radii Of Catalog Stars

As mentioned above, PARAM also can be used to derive the mass, radii, surface gravity and (B-V) colors of the stars. As in the case of the age determination, the errors on these parameters are very high. In Fig. 10.20 on the left panel, we compare the (B-V) colors derived from PARAM Tycho-2 data. On the right panel, we compare the surface gravities ($\log g$) derived from PARAM with those calculated from χ^2 fitting. The agreement between these determinations is reasonably good.

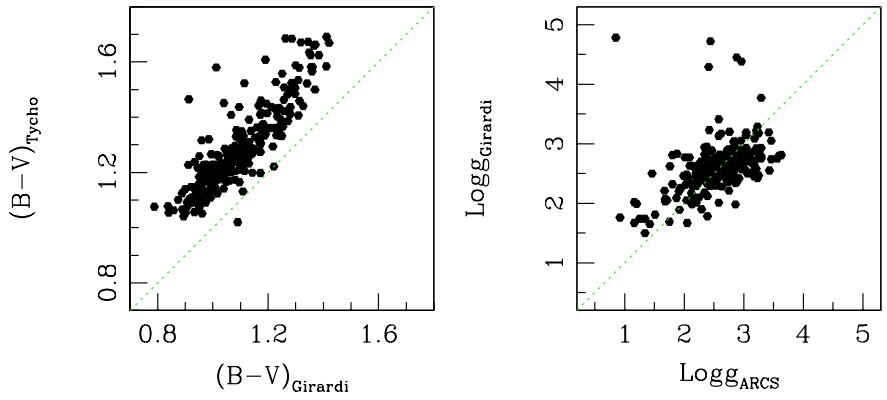

Figure 10.20: $(B-V)$ colours by Tycho-2 and by Girardi's Param are compared (left panel). *logg* values derived by χ^2 fitting and derived from Girardi's Param Evolutionary tracks are compared (right panel).

In Fig. 10.21 we present the mass-radii and $\log g$-radii relations for our target stars derived using PARAM.

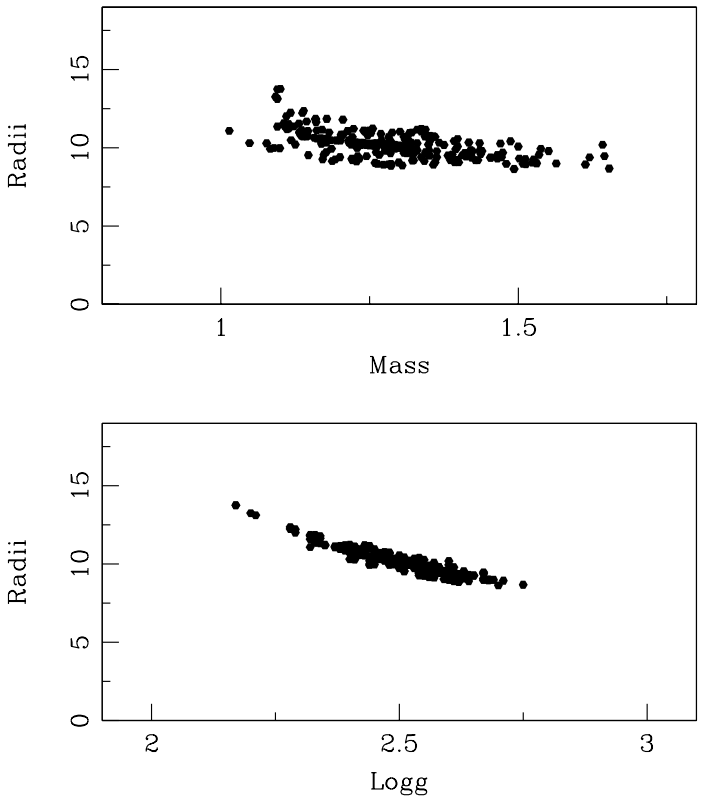

Figure 10.21: The Radii-Mass and Radii-logg plot for target stars.

Bibliography

Alonso, A., Arribas, S., and Martínez-Roger, C.: 1999, *A&As* **140**, 261

Antoja, T., Figueras, F., Fernández, D., and Torra, J.: 2008, *A&A* **490**, 135

Bailer-Jones, C. A. L.: 2005, in C. Turon, K. S. O'Flaherty, & M. A. C. Perryman (ed.), *The Three-Dimensional Universe with Gaia*, Vol. 576 of *ESA Special Publication*, pp 393–+

Bailer-Jones, C. A. L.: 2008, in R. W. Argyle, P. S. Bunclark, & J. R. Lewis (ed.), *Astronomical Data Analysis Software and Systems XVII*, Vol. 394 of *Astronomical Society of the Pacific Conference Series*, pp 169–+

Bailer-Jones, C. A. L.: 2009, in J. Andersen, J. Bland-Hawthorn, & B. Nordström (ed.), *IAU Symposium*, Vol. 254 of *IAU Symposium*, pp 475–482

Bailer-Jones, C. A. L. and Smith, K. W.: 2008, in C. A. L. Bailer-Jones (ed.), *American Institute of Physics Conference Series*, Vol. 1082 of *American Institute of Physics Conference Series*, pp 3–8

Bellas-Velidis, I., Pasian, F., Kontizas, E., Dapergolas, A., and Bratsolis, E.: 1997, in J. D. Hadjidemetrioy & J. H. Seiradakis (ed.), *Joint European and National Astronomical Meeting*

Bensby, T. and Feltzing, S.: 2010, *Highlights of Astronomy* **15**, 789

Bensby, T., Feltzing, S., and Lundström, I.: 2003, *A&A* **410**, 527

Bensby, T., Feltzing, S., Lundström, I., and Ilyin, I.: 2005, *A&A* **433**, 185

Binney, J. J., Dehnen, W., Houk, N., Murray, C. A., and Penston, M. J.: 1997, in R. M. Bonnet, E. Høg, P. L. Bernacca, L. Emiliani, A. Blaauw, C. Turon, J. Kovalevsky, L. Lindegren, H. Hassan, M. Bouffard, B. Strim, D. Heger, M. A. C. Perryman, & L. Woltjer (ed.), *Hipparcos - Venice '97*, Vol. 402 of *ESA Special Publication*, pp 473–478

Bobylev, V. V. and Bajkova, A. T.: 2007, *Astronomy Reports* **51**, 372

Bobylev, V. V. and Bajkova, A. T.: 2010, in C. Sterken, N. Samus, & L. Szabados (ed.), *Variable Stars, the Galactic halo and Galaxy Formation*, pp 173–+

Breddels, M. A., Smith, M. C., Helmi, A., Bienaymé, O., Binney, J., Bland-Hawthorn, J., Boeche, C., Burnett, B. C. M., Campbell, R., Freeman, K. C., Gibson, B., Gilmore, G., Grebel, E. K., Munari, U., Navarro, J. F., Parker, Q. A., Seabroke, G. M., Siebert, A., Siviero, A., Steinmetz, M., Watson, F. G., Williams, M., Wyse, R. F. G., and Zwitter, T.: 2010, *A&A* **511**, A90+

Carraro, G. and Chiosi, C.: 1994, *A&A* **287**, 761

Carraro, G., Ng, Y. K., and Portinari, L.: 1998, *MNRAS* **296**, 1045

Castelli, F. and Kurucz, R. L.: 2010, *A&A* **520**, A57+

Cioni, M. R., Habing, H. J., Loup, C., Groenewegen, M. A. T., Epchtein, N., and Consortium, T. D.: 1999, in P. Whitelock & R. Cannon (ed.), *The Stellar Content of Local Group Galaxies*, Vol. 192 of *IAU Symposium*, pp 65–+

Coskunoglu, B., Ak, S., Bilir, S., Karaali, S., Yaz, E., Gilmore, G., Seabroke, G. M., Bienayme, O., Bland-Hawthorn, J., Campbell, R., Freeman, K. C., Gibson, B., Grebel, E. K., Munari, U., Navarro, J. F., Parker, Q. A., Siebert, A., Siviero, A., Steinmetz, M., Watson, F. G., Wyse, R. F. G., and Zwitter, T.: 2010, *ArXiv e-prints*

Cutri, R. M., Skrutskie, M. F., van Dyk, S., Beichman, C. A., Carpenter, J. M., Chester, T., Cambresy, L., Evans, T., Fowler, J., Gizis, J., Howard, E., Huchra, J., Jarrett, T., Kopan, E. L., Kirkpatrick, J. D., Light, R. M., Marsh, K. A., McCallon, H., Schneider, S., Stiening, R., Sykes, M., Weinberg, M., Wheaton, W. A., Wheelock, S., and Zacarias, N.: 2003, *2MASS All Sky Catalog of point sources.*

da Silva, L., Girardi, L., Pasquini, L., Setiawan, J., von der Lühe, O., de Medeiros, J. R., Hatzes, A., Döllinger, M. P., and Weiss, A.: 2006, *A&A* **458**, 609

Dehnen, W. and Binney, J. J.: 1998, *MNRAS* **298**, 387

Edvardsson, B., Gustafsson, B., Andersen, J., Nissen, P. E., Lambert, D. L., and Tomkin, J.: 1993, in G. Klare (ed.), *Astronomische Gesellschaft Abstract Series*, Vol. 8 of *Astronomische Gesellschaft Abstract Series*, pp 105–+

Eggen, O. J.: 1996, *AJ* **112**, 1595

Eggen, O. J., Lynden-Bell, D., and Sandage, A. R.: 1962, *APJ* **136**, 748

Famaey, B., Jorissen, A., Luri, X., Mayor, M., Udry, S., Dejonghe, H., and Turon, C.: 2005, *A&A* **430**, 165

Fehrenbach, C., Duflot, M., and Burnage, R.: 2001, *A&A* **369**, 65

Francis, C. and Anderson, E.: 2009, *NA* **14**, 615

Freeman, K. C.: 2009, in J. Andersen, J. Bland-Hawthorn, & B. Nordström (ed.), *IAU Symposium*, Vol. 254 of *IAU Symposium*, pp 111–120

Friel, E. D. and Janes, K. A.: 1993, *A&A* **267**, 75

Girardi, L.: 1999, *MNRAS* **308**, 818

Girardi, L., Bressan, A., Bertelli, G., and Chiosi, C.: 2000, *A&As* **141**, 371

Hekker, S. and Melendez, J.: 2007, *VizieR Online Data Catalog* **347**, 51003

Høg, E.: 1998, *Highlights of Astronomy* **11**, 544

Houk, N. and Swift, C.: 2000, *VizieR Online Data Catalog* **3214**, 0

Ibukiyama, A. and Arimoto, N.: 2002, *VizieR Online Data Catalog* **339**, 40927

Jaschek, C. and Valbousquet, A.: 1991, *A&A* **242**, 77

Johnson, D. R. H. and Soderblom, D. R.: 1987, *AJ* **93**, 864

Katz, D.: 2009, in M. Heydari-Malayeri, C. Reyl'E, & R. Samadi (ed.), *SF2A-2009: Proceedings of the Annual meeting of the French Society of Astronomy and Astrophysics*, pp 57–+

Katz, D., Munari, U., Cropper, M., Zwitter, T., Thévenin, F., David, M., Viala, Y., Crifo, F., Gomboc, A., Royer, F., Arenou, F., Marrese, P., Sordo, R., Wilkinson, M., Vallenari, A., Turon, C., Helmi, A., Bono, G., Perryman, M., Gómez, A., Tomasella, L., Boschi, F., Morin, D., Haywood, M., Soubiran, C., Castelli, F., Bijaoui, A., Bertelli, G., Prsa, A., Mignot, S., Sellier, A., Baylac, M., Lebreton, Y., Jauregi, U., Siviero, A.,

Bingham, R., Chemla, F., Coker, J., Dibbens, T., Hancock, B., Holland, A., Horville, D., Huet, J., Laporte, P., Melse, T., Sayède, F., Stevenson, T., Vola, P., Walton, D., and Winter, B.: 2004, *MNRAS* **354**, 1223

Keenan, P. C. and Barnbaum, C.: 1999, *APJ* **518**, 859

Kovalevsky, J., Lindegren, L., Perryman, M. A. C., Hemenway, P. D., Johnston, K. J., Kislyuk, V. S., Lestrade, J. F., Morrison, L. V., Platais, I., Röser, S., Schilbach, E., Tucholke, H., de Vegt, C., Vondrak, J., Arias, F., Gontier, A. M., Arenou, F., Brosche, P., Florkowski, D. R., Garrington, S. T., Kozhurina-Platais, V., Preston, R. A., Ron, C., Rybka, S. P., Scholz, R., and Zacharias, N.: 1997, *A&A* **323**, 620

Kucinskas, A., Lindegren, L., and Vansevicius, V.: 2005, in C. Turon, K. S. O'Flaherty, & M. A. C. Perryman (ed.), *The Three-Dimensional Universe with Gaia*, Vol. 576 of *ESA Special Publication*, pp 695–+

Lattanzi, M. G. and Sozzetti, A.: 2010, in V. Coudé Du Foresto, D. M. Gelino, & I. Ribas (ed.), *Astronomical Society of the Pacific Conference Series*, Vol. 430 of *Astronomical Society of the Pacific Conference Series*, pp 253–+

Lindegren, L.: 2005, in C. Turon, K. S. O'Flaherty, & M. A. C. Perryman (ed.), *The Three-Dimensional Universe with Gaia*, Vol. 576 of *ESA Special Publication*, pp 29–+

Lindegren, L. and Perryman, M. A. C.: 1995, in M. A. C. Perryman & F. van Leeuwen (ed.), *Future Possibilities for bstrometry in Space*, Vol. 379 of *ESA Special Publication*, pp 23–+

Ma, C., Arias, E. F., Eubanks, T. M., Fey, A. L., Gontier, A., Jacobs, C. S., Sovers, O. J., Archinal, B. A., and Charlot, P.: 1998, *AJ* **116**, 516

Mignard, F.: 2000, *A&A* **354**, 522

Mihalas, D. and Binney, J.: 1981, *Galactic astronomy: Structure and kinematics /2nd edition/*

Mishenina, T. V., Bienaymé, O., Gorbaneva, T. I., Charbonnel, C., Soubiran, C., Korotin, S. A., and Kovtyukh, V. V.: 2006, *A&A* **456**, 1109

Moore, C. E.: 1959, *National Bureau of Standards Technical Note* **36**, 1

Munari, U.: 1999, *Baltic Astronomy* **8**, 73

Munari, U., Agnolin, P., and Tomasella, L.: 2001, *Baltic Astronomy* **10**, 613

Munari, U. and Castelli, F.: 2000, *A&As* **141**, 141

Munari, U. and Lattanzi, M. G.: 1992, *PASP* **104**, 121

Munari, U., Sordo, R., Castelli, F., and Zwitter, T.: 2005, *A&A* **442**, 1127

Munari, U. and Tomasella, L.: 1999, *A&As* **137**, 521

Munari, U., Zwitter, T., and Milone, E. F.: 2004, in R. W. Hilditch, H. Hensberge, & K. Pavlovski (ed.), *Spectroscopically and Spatially Resolving the Components of the Close Binary Stars*, Vol. 318 of *Astronomical Society of the Pacific Conference Series*, pp 422–429

Ng, Y. K. and Bertelli, G.: 1998, *A&A* **329**, 943

Nissen, P. E.: 2004, *Origin and Evolution of the Elements* pp 154–+

Nordstrom, B., Mayor, M., Andersen, J., Holmberg, J., Pont, F., Jorgensen, B. R., Olsen, E. H., Udry, S., and Mowlavi, N.: 2004, *VizieR Online Data Catalog* **5117**, 0

Perryman, M. A. C., de Boer, K. S., Gilmore, G., Høg, E., Lattanzi, M. G., Lindegren, L., Luri, X., Mignard, F., Pace, O., and de Zeeuw, P. T.: 2001, *A&A* **369**, 339

Perryman, M. A. C., Lindegren, L., Kovalevsky, J., Hoeg, E., Bastian, U., Bernacca, P. L., Crézé, M., Donati, F., Grenon, M., van Leeuwen, F., van der Marel, H., Mignard, F., Murray, C. A., Le Poole, R. S., Schrijver, H., Turon, C., Arenou, F., Froeschlé, M., and Petersen, C. S.: 1997, *A&A* **323**, L49

Piskunov, A. E., Kharchenko, N. V., Röser, S., Schilbach, E., and Scholz, R.: 2006, *A&A* **445**, 545

Rambaux, N., Couedtic, J., Laskar, J., and Sozzetti, A.: 2009, in M. Heydari-Malayeri, C. Reyl'E, & R. Samadi (ed.), *SF2A-2009: Proceedings of the Annual meeting of the French Society of Astronomy and Astrophysics*, pp 73–+

Ramírez, I. and Meléndez, J.: 2005, *APJ* **626**, 465

Robin, A. C., Reylé, C., Picaud, S., and Schultheis, M.: 2005, *A&A* **430**, 129

Schönrich, R., Binney, J., and Dehnen, W.: 2010, *MNRAS* **403**, 1829

Skuljan, J., Hearnshaw, J. B., and Cottrell, P. L.: 1999, *MNRAS* **308**, 731

Smith, K., Tiede, C., Elting, C., and Bailer-Jones, C. A. L.: 2008a, in R. W. Argyle, P. S. Bunclark, & J. R. Lewis (ed.), *Astronomical Data Analysis Software and Systems XVII*, Vol. 394 of *Astronomical Society of the Pacific Conference Series*, pp 539–+

Smith, K. W., Bailer-Jones, C. A. L., Elting, C., and Tiede, C.: 2008b, in C. A. L. Bailer-Jones (ed.), *American Institute of Physics Conference Series*, Vol. 1082 of *American Institute of Physics Conference Series*, pp 29–36

Soubiran, C., Bienaymé, O., Mishenina, T. V., and Kovtyukh, V. V.: 2008, *A&A* **480**, 91

Soubiran, C. and Girard, P.: 2005, *VizieR Online Data Catalog* **343**, 80139

Steinmetz, M., Zwitter, T., Siebert, A., Watson, F. G., Freeman, K. C., Munari, U., Campbell, R., Williams, M., Seabroke, G. M., Wyse, R. F. G., Parker, Q. A., Bienaymé, O., Roeser, S., Gibson, B. K., Gilmore, G., Grebel, E. K., Helmi, A., Navarro, J. F., Burton, D., Cass, C. J. P., Dawe, J. A., Fiegert, K., Hartley, M., Russell, K. S., Saunders, W., Enke, H., Bailin, J., Binney, J., Bland-Hawthorn, J., Boeche, C., Dehnen, W., Eisenstein, D. J., Evans, N. W., Fiorucci, M., Fulbright, J. P., Gerhard, O., Jauregi, U., Kelz, A., Mijović, L., Minchev, I., Parmentier, G., Peñarrubia, J., Quillen, A. C., Read, M. A., Ruchti, G., Scholz, R., Siviero, A., Smith, M. C., Sordo, R., Veltz, L., Vidrih, S., von Berlepsch, R., Boyle, B. J., and Schilbach, E.: 2006, *AJ* **132**, 1645

Takeda, Y., Sato, B., and Murata, D.: 2008, *PASJ* **60**, 781

Twarog, B. A.: 1980, *APJ* **242**, 242

Valentini, M. and Munari, U.: 2010, *A&A* **522**, A79+

van Leeuwen, F.: 2007, *A&A* **474**, 653